A Search for Neutrino Oscillations via the Muonic Decay of the Tau Lepton at the CERN SPS

Joshua C. Long

A dissertation submitted to the Johns Hopkins University
in conformity with the requirements for the degree of
Doctor of Philosophy

Baltimore, Maryland
June 1997

Work Supported in part by the National Science Foundation
through grant NSF PHY-9526278 under the direction of
Barry Blumenfeld

Abstract

The results of a search for the oscillation $\nu_\mu \to \nu_\tau$ with the NOMAD experiment at CERN are presented. NOMAD is designed to detect τ–lepton production events in the SPS wide band ν_μ beam. A 3-ton active target of tracking chambers, a series of TRD modules, a preshower module, and a lead–glass calorimeter are installed in the magnet from the UA1 experiment, approximately 1 km from the ν_μ source. Scintillator calorimeters are installed in the forward and rear magnet elements, and part of the UA1 muon system is placed at the rear of the detector. After a total of approximately 1×10^{19} protons on target, no evidence of τ production is detected via the decay channel $\tau^- \to \mu^- \nu_\tau \bar{\nu}_\mu$.

Acknowledgments

I would like to thank my parents, without whom none of this would have been possible. I would also like to thank my extended family in Maryland and Pennsylvania, especially Kevin and Suzanne Haggerty, for all of their hospitality over the past seven years.

The weeks and months which my advisor, Barry Blumenfeld, managed to spend at CERN were always marked by greater enthusiasm, productivity, and diplomacy, not to mention respect for real physics processes. My only regret is that he was not able to spend more time at the experiment. Unfortunately, these times of tight budgets appeared to affect his situation more than mine. I am very grateful for his efforts to keep me solvent in Geneva for four years.

Fortunately, there were always collaborators at NOMAD willing to come to the assistance of an overwhelmed student. In my situation, that task fell to (on?) Achim Geiser. It is difficult to think how I could have finished this work without his guidance, which was practically day–to–day and all the more worthy of thanks given the number of other tasks to which he set himself.

Thanks especially to Leslie Camilleri and the CERN group on NOMAD, who managed to scare up an additional few months' worth of funding so that I could complete my analysis while still present at the lab. Thanks to the leadership of our spokesman, Luigi DiLella, and his predecessor Francois Vannucci, I could always count on that atmosphere being open and lively.

The completion of this study would have been further delayed without the work

of Dario Autiero, who assembled the 1995 data sets into an easily accessible format. Burkhard Schmidt provided many useful comments (which I regret not being able to implement in full) in addition to his invaluable work in helping to assemble the detector. Special thanks to Anna Lupi for providing the code which made it possible to analyze the data in a familiar environment, as well as for hosting me in Florence during a much needed vacation. On a similar note, I would like to thank Domizia Orestano for hosting me in Rome, on one of her rare breaks from all that electron work.

My quick adjustment to life at the lab was assured as soon as I arrived and began working for Lucie Linssen and the rest of the muon chamber group. This included Emmanuel Tsesmelis and, later, Didier Ferrere.

The hours in front of the terminals would have been far less efficient had it not been for the wizardry of my co–conspirator, David Steele. Jean-Pierre Meyer was always willing to lend a hand in the management of the muon chamber simulation code.

Thanks also to Steven Boyd, Alain Castera, Olivier Cloue, Claude Detraz, Nikki Hyett, Filippo Martelli, Chung Nguyen Mau, Caroline Poulsen, Chiara Roda, Andre Rubbia, Daniel Sillou, Malica Tareb, Michele Veltri, Bruce Yabsley, and any others I may have forgotten (it took too long...) With their help I was finally able to make the slow–control monitoring system reasonably functional and transparent, whatever other shortcomings that system may be determined to possess, or whatever other roles some of the aforementioned colleagues may have played in the decision as to the software platform used, or in the securing of my eventual degree of responsibility for it.

No one survives a lengthy stint overseas without the appropriate penalties in paperwork. I am very grateful for the efforts of people in both the New World and the Old for making the whole process less painful, including Nancy Anderson, Jane Barney, Jill Callahan, Estella Hankin, Janet Krupsaw, Rachel Phillips, and Barbara Staicer. Special thanks to Marie-Anne Huber, especially for the passes to the Grand

Theatre.

I would like to thank Harold Woods for his supervision of my first independent experiment, a home–brewed version of a gravitational torsion balance. My own gravitation toward this field was assured under the guidance of Robert H. Romer and Joel Gordon. I owe my introduction to experimental particle physics in particular to Peter Fisher, who gave me the opportunity to work with his group at Los Alamos after my first year at Hopkins, and who has provided important advice ever since. Thanks also to Bob Cousins, both for his advice and help in arranging a trip to a conference.

Thanks again to Barry for his support during my last few weeks at Hopkins, and to Leon Madansky, Thomas Fulton, Warner Love, and Nino Panagia for agreeing to be on my committee on short notice.

And thanks to everyone else for those times in between, for the midnight cruises up Santa Clara canyon (was this in the job description, gringo?), the beer gardens in the alleys of the Neustadt (and about fifty other places), for the views from San Giorgio, the Aventino, and Fiesole (*my* view was perfect, despite all of the fog), for the powders of Verbier, Tignes, Argentiere, and Eldora, and the celebrations in Sergy, Carouge, and Collevecchio. Who ever said Baltimore wouldn't be any fun?

Contents

List of Figures

List of Tables

Chapter 1

Introduction

A primary goal of particle physics is to describe and predict, as completely as possible, the properties of and interactions between the most fundamental constituents of matter. To this end, the most successful theory to have emerged is the so–called Standard Model of strong and electroweak interactions, which has stood up to basically every experimental test yet completed. In the standard model, the fundamental building blocks of matter are the quarks and leptons, and the interactions between them are governed by the mediating bosons (figure 1.1). To date, three generations of quarks and leptons have been observed. The lepton family consists of the charged electron and the successively more massive muon and tau particles, each grouped with an associated chargeless neutrino.

Neutrinos have been observed to interact only via the weak nuclear force. Observations of neutrino interactions are therefore very difficult, and, of all known elementary particles, the neutrinos are the least well understood. It is not known, for instance, whether neutrinos are stable, or whether they have mass. The latter question in particular is one of the most important in contemporary particle physics.

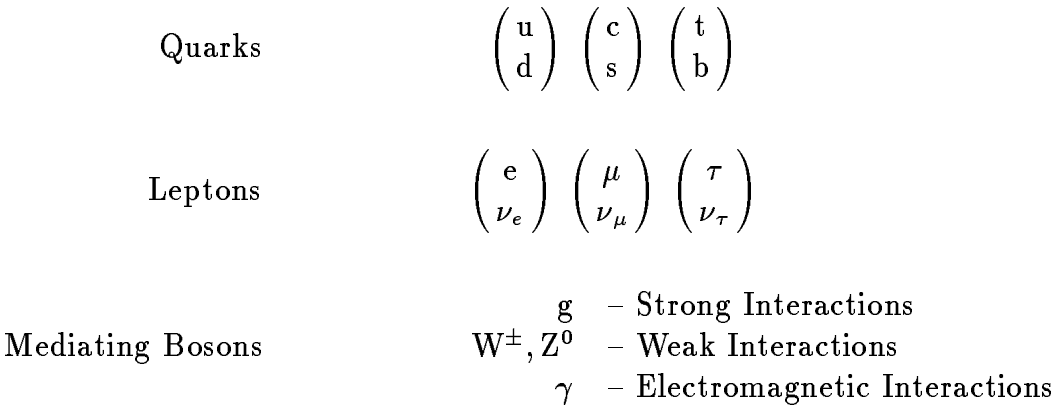

Figure 1.1: Elementary Particles in the Standard Model

1.1 Historical Background

The charged particles in the first generation of quarks and leptons comprise the basic ingredients of tangible matter, with the up and down quarks combining into the nuclear particles, the proton and the neutron. In 1930, even the basic picture of these composite particles had yet to be elucidated. An outstanding puzzle at that time was the demonstration that the energy spectrum of electrons emitted from radioactive nuclei (beta–decay) was continuous. Another was that the nitrogen–14 nucleus, assumed to be comprised of an odd number of spin 1/2 particles (14 protons and 7 electrons), was shown to have integer spin [1]. In response to these problems, Wolfgang Pauli proposed a neutral spin 1/2 particle, with mass comparable to that of the electron, as a nuclear constituent and which carried away the undetected energy in beta decay. With Chadwick's discovery of the neutron in 1932 as the second nuclear constituent, Enrico Fermi named Pauli's particle the "neutrino." Fermi subsequently inferred the neutrino to be massless from the shape of beta decay spectra, and used it as an essential ingredient in his theory of the weak interaction [2].

The success of Fermi's theory and its extensions was convincing evidence for

the existence of the neutrino. Yet, no direct evidence of interactions induced by neutrinos was observed for over twenty years after Pauli's suggestion. This was of no surprise, since the predicted strength of the weak interaction implied that a neutrino would pass through 50 billion miles of water without interacting. The situation finally changed in the 1950s with the experiments of C. Cowan and F. Reines, who used large tanks of liquid scintillator to detect signals from inverse beta–decay reactions:

$$\bar{\nu} \ + \mathrm{p} \ \rightarrow \ \mathrm{n} \ + \mathrm{e}^{+} \tag{1.1}$$

induced by neutrinos from a nuclear reactor [3].

At about the same time, a crucial step in the understanding of the weak interaction came with the re-discovery by C.N. Yang and T.D. Lee that there was no evidence for parity conservation in weak interactions. This led to a number of experiments which observed parity violation in the directional dependence of decay rates in the chain $\pi \ \rightarrow \ \mu \ \rightarrow \ \mathrm{e}$, and in the beta decay of ^{60}Co. Parity violation also allowed for the longitudinal polarization of the final state electrons in beta decay. The degree of polarization subsequently observed in an experiment by Frauenfelder, et. al. [4] lent support to the hypothesis that the neutrino carried a single handedness, i.e., that the neutrinos participating in these reactions spun only clockwise with respect to the direction of their momenta (left–handed), or only counterclockwise (right–handed). In an elegant experimental study of the reaction:

$$\mathrm{e}^{-} \ + {}^{152}\mathrm{Eu} \ \rightarrow \ {}^{152}\mathrm{Sm} \ + \nu_e \tag{1.2}$$

Goldhaber, Grodzins, and Sunyar demonstrated the neutrino to be left–handed [5].

Soon after these developments, it became possible to study interactions with high–energy neutrinos produced at accelerators. In 1962, Gaillard, Lederman, Schwartz, Steinberger, et. al. reported the observation of the interactions of neutrinos produced by the decay $\pi \rightarrow \ \mu + \nu$ at the Brookhaven Alternating Gradient Synchrotron. The appearance of muons in the observed events was taken as evidence of a second neutrino flavor distinct from that appearing in beta decay, and that the

observed reactions were therefore:

$$\nu_\mu \ + \mathrm{n} \quad \rightarrow \quad \mathrm{p} \ + \mu^-, \tag{1.3}$$

$$\bar{\nu}_\mu \ + \mathrm{p} \quad \rightarrow \quad \mathrm{n} \ + \mu^+ \tag{1.4}$$

This lent support to the proposal of two distinct quantum numbers, muon number (+1 for μ^- and ν_μ) and electron number (+1 for e^- and ν_e), which, separately conserved, also prevented the unobserved decay $\mu \rightarrow \mathrm{e} + \gamma$ [6].

1.2 Solar Neutrinos

Theoretical models of energy production in the sun also predicted that the sun should be a copious source of neutrinos. In 1968, R. Davis and his collaborators began a search for the reaction:

$$\nu_e \ + {}^{37}\mathrm{Cl} \rightarrow \ {}^{37}\mathrm{Ar} + \mathrm{e}^- \tag{1.5}$$

in a large tank of C_2Cl_4 located at the Homestake mine in South Dakota. Based on predictions from what has become known as the Standard Solar Model (SSM), the above reaction was expected to be sensitive primarily to electron neutrinos produced in the decay:

$${}^{8}\mathrm{B} \rightarrow \ {}^{8}\mathrm{Be} + \mathrm{e}^+ \ + \nu_e, \tag{1.6}$$

a relatively rarely–occurring reaction in the proton–proton cycle responsible for most of the sun's luminosity. The flux rate expected was $(2.0 \pm 1.2) \times 10^{-35}\mathrm{s}^{-1}$ per ^{37}Cl atom. After the first run, the rate was measured to be less than 0.3×10^{-35} s^{-1} per ^{37}Cl atom, or $0.6 \times 10^{-35}\mathrm{s}^{-1}$ per ^{37}Cl atom without allowance for background. This was nearly a factor of three lower than the prediction [7].

Over the thirty year period since its construction, the Homestake experiment has continued to collect data. Several other experiments, sensitive to neutrinos produced in other solar reactions, have also come on line, most notably Kamiokande in Japan and GALLEX at Gran Sasso in Italy. The latest results from these experiments,

together with the SSM flux predictions, are summarized in table 1.1 [8]. These results have come to be known as the solar neutrino puzzle.

Experiment	*Measured Flux*	*SSM Prediction*	*units*
Homestake	2.55 ± 0.35	8.0 ± 3.0	SNU[9]
GALLEX	79 ± 16	132 ± 7	SNU
Kamiokande	$2.9 \pm 0.2 \pm 0.35$	5.7 ± 0.7	$\mathrm{cm}^{-2}\mathrm{s}^{-1}$

Table 1.1: Results of Solar Neutrino Experiments

Possible explanations of this problem generally fall into three categories. First is that the experimental results are preliminary, or wrong[1]. Second, there may be flaws in the SSM. Third, the electron–neutrinos produced in the sun are somehow depleted before reaching the detectors on Earth. An intriguing possibility is that the neutrinos change flavor or "oscillate" into muon– or tau–neutrinos, thereby becoming immune to detection via reactions such as (1.5).

1.3 Neutrino Oscillations

Within the framework of Quantum Mechanics, the oscillation phenomenon can arise when the states which govern the creation and detection of particles differ from the states which govern the propagation of the particles in space–time. The classic example is the K^0-$\overline{\mathrm{K}}^0$ system.

K^0s and $\overline{\mathrm{K}}^0$s are produced in strong interactions, and have definite strangeness, or strange–quark content. They decay (and are detected), however, via weak interactions, which do not conserve strangeness. The physical states, i.e., particles with definite masses and lifetimes which are eigenstates of the total Hamiltonian (which includes both strong and weak interactions), are linear combinations of K^0 and $\overline{\mathrm{K}}^0$.

If a state consisting purely of K^0 is created at time $t = 0$, the K^0-intensity at a

[1] A more precise statement would be that at least two of the experiments discussed in the text are wrong. For a more detailed interpretation of the results, see reference 8.

later time t contains a term proportional to $\cos \Delta m t$, where Δm is the mass difference between the two physical states. Thus, the K^0 and $\overline{K}^0$ intensities are predicted to oscillate in time for any non-zero mass difference, and the oscillation frequency is simply Δm^2. Such oscillations have been observed, and the corresponding mass difference is measured to be about 3.5×10^{-6} eV [10].

In analogy to the K^0-$\overline{K}^0$ system, the theory of neutrino oscillations is based on the premise that the weak–interaction states in which the neutrinos are produced and detected (denoted ν_e, ν_μ, ν_τ) are linear combinations of the states of the free Hamiltonian, which have definite mass (denoted ν_1, ν_2, ν_3). In a system of free neutrinos, any mass differences between ν_1, ν_2 and ν_3, lead to different propagation frequencies for these states, and thus different admixtures of ν_e, ν_μ, and ν_τ at later points in the time evolution of the system. This picture was first developed by Pontecorvo in 1957 and 1967 [11], and Maki et. al. in 1962 [12].

For a complete discussion of the three–component oscillation picture, see reference 2. The theory is simplified considerably by examining the case of two types of neutrino (ν_μ, ν_τ), and many experimental results are still reported in terms of the two–component theory. In this picture, ν_μ and ν_τ are linear combinations of two mass eigenstates (ν_1, ν_2). Expressed in terms of a unitary matrix with arbitrary mixing angle θ,

$$\begin{pmatrix} \nu_\mu \\ \nu_\tau \end{pmatrix} = \begin{pmatrix} \cos\theta & \sin\theta \\ -\sin\theta & \cos\theta \end{pmatrix} \begin{pmatrix} \nu_1 \\ \nu_2 \end{pmatrix}. \tag{1.7}$$

The states (ν_1, ν_2), eigenstates of the free Hamiltonian, determine the evolution of the system in space–time. Inverting equation 1.7, these states are:

$$\begin{aligned} \nu_1 &= \nu_\mu \cos\theta - \nu_\tau \sin\theta \\ \nu_2 &= \nu_\mu \sin\theta + \nu_\tau \cos\theta. \end{aligned} \tag{1.8}$$

In the units $\hbar = c = 1$, the time–dependent states are:

$$\begin{aligned} \nu_1(t) &= \nu_1(0) e^{-iE_1 t} \\ \nu_2(t) &= \nu_2(0) e^{-iE_2 t}. \end{aligned} \tag{1.9}$$

Suppose a beam of pure ν_μ is prepared at time $t = 0$, so that $\nu_\mu(0) = 1$ and $\nu_\tau(0) = 0$. Then, from equation 1.8.

$$\begin{aligned} \nu_1(0) &= \cos\theta \\ \nu_2(0) &= \sin\theta. \end{aligned} \tag{1.10}$$

From equation 1.7, the time–dependent ν_μ state is

$$\nu_\mu(t) = \nu_1(t)\cos\theta + \nu_2(t)\sin\theta. \tag{1.11}$$

Using the results from equations 1.9 and 1.10, the amplitude for detecting ν_μ at time t is then:

$$\nu_\mu(t) = \cos^2\theta e^{-iE_1 t} + \sin^2\theta e^{-iE_2 t}, \tag{1.12}$$

and the ν_μ intensity in the beam at time t is given by:

$$I_{\nu_\mu} = |\nu_\mu(t)|^2 = 1 - \sin^2 2\theta \sin^2\left(\frac{(E_2 - E_1)t}{2}\right). \tag{1.13}$$

The last expression indicates that the relative intensities of ν_μ and ν_τ will oscillate in time with frequency $(E_2 - E_1)/2$. Assuming conservation of momentum (i.e., that the states $\nu_1(t)$ and $\nu_2(t)$ propagate with the same momentum p), and that $m_{1,2} \ll E_{1,2}$, the energies can be expressed:

$$E_{1,2} = p + \frac{m_{1,2}^2}{2p}. \tag{1.14}$$

Substituting this result into equation 1.13, and expressing the time t in terms of the distance L from the ν_μ production source, the probabilities of finding ν_μ and ν_τ at distance L are then:

$$\begin{aligned} P(\nu_\mu \to \nu_\mu) &= 1 - \sin^2 2\theta \sin^2\left(\frac{1.27\Delta m^2 L}{E}\right) \\ P(\nu_\mu \to \nu_\tau) &= 1 - P(\nu_\mu \to \nu_\mu). \end{aligned} \tag{1.15}$$

Here, $\Delta m^2 = m_2^2 - m_1^2$, and the numerical factor 1.27 applies if Δm^2 is expressed in $(\mathrm{eV})^2$, L in meters, and the beam energy E in MeV.

According to this model, in which neutrino flavor oscillations arise in a way analogous to the observed strangeness oscillations in the K^0 system, a positive result ($P(\nu_\mu \rightarrow \nu_\tau) \neq 0$) would imply that at least one neutrino species must have non–zero mass. Neutrino oscillation experiments search simultaneously for evidence of lepton–number violation and neutrino mass, and therefore constitute one of the most important probes for new phenomena in contemporary particle physics.

1.4 Models of Neutrino Masses

In the absence of any convincing evidence for neutrino mass, neutrinos are taken to be massless in the Standard Model. There is no compelling reason for doing so. The local gauge invariance of the Standard Model Lagrangian, for instance, requires the photon mass to be zero, but this is not true for any of the fermions. Many models of neutrino mass generation have been proposed, the details of which are beyond the scope of this chapter, but of which a few should be mentioned in brief.

In the Standard Model, the charged fermions are assumed to acquire mass via the same mechanism responsible for the generation of the masses of the weak vector bosons. This occurs via coupling to the Higgs field, an isospin doublet with weak hypercharge $Y = 1$ and non-zero vacuum expectation value[2]. In direct analogy to the charged fermions, a coupling of the same form can be introduced into the Standard Model Lagrangian for the neutrinos. The spontaneous breaking of the $SU(2) \times U(1)$ symmetry of the Lagrangian yields a term for the neutrino mass, which can be expressed in the form:

$$L = -(\bar{\nu}_L \mathbf{M} \nu_R + \bar{\nu}_R \mathbf{M}^\dagger \nu_L), \tag{1.16}$$

where ν_L and ν_R are left- and right–handed flavor states, and $\mathbf{M}$ is a complex 3×3 mass matrix [2]. This model assumes that neutrinos are, like their charged partners,

[2]The details of mass generation in the Standard Model, technically beyond the scope of this chapter, are reviewed exhaustively in the literature. A good introductory discussion may be found in chapters 14 and 15 of reference 13.

Dirac particles (four-component objects; left- and right–handed particles and their antiparticles), and the above expression is referred to as the Dirac mass term.

One shortcoming of this picture is the necessity of introducing the ν_R states, which have not been observed (they are assumed not to exist in the Standard Model). Another is the lack of explanation as to why the strength of the coupling needed to generate the corresponding neutrino masses is so small compared to that for the charged leptons.

Another picture of neutrino mass can be constructed if the neutrinos involved are self–conjugate or Majorana particles. A Majorana mass term uses the left–handed states alone, and has the form

$$L = -\frac{1}{2}\bar{\nu}_L^C \mathbf{M} \nu_L + \text{ h.c.}, \tag{1.17}$$

where ${\nu_L}^C$ is the charge–conjugate of the state ν_L. In these models, neutrino masses are generated via more complicated scalar couplings than those used in the Standard Model. Some of these models are not ruled out. Much in the same way as the Dirac model, however, they suffer in general from the lack of explanation for the values of (and disparities between) the couplings which must be introduced to produce the observed neutrino masses [14].

Another class of models considers cases in which both Dirac and Majorana mass terms are present. Assuming one neutrino flavor generation, a general mass term may be written:

$$L = -M\bar{\nu}_L \nu_R - \frac{1}{2}(m_L \bar{\nu}_L^C \nu_L + m_R \bar{\nu}_R^C \nu_R) + \text{ h.c.} \tag{1.18}$$

Here, M is a Dirac mass mixing ν_L and ν_R, m_L is a Majorana mass for ν_L, and m_R is a Majorana mass for ${\nu_R}$[3]. Equation 1.18 can be expressed in matrix form and diagonalized to reveal two mass states ν_1 and ν_2 for this generation, which are mixtures of ν_L and ν_R.

[3]The discussion in the remainder of this section follows reference 2, pp. 45–47 and 96–97.

The mass eigenvalues m_1 and m_2 of these states are simple functions of the masses M, m_R, and m_L. An interesting case arises in the limit $m_R \gg M, m_L$, namely,

$$m_1 \simeq \frac{M}{m_R},\ m_2 \simeq m_R. \tag{1.19}$$

As m_R (and hence m_2) increases, m_1 decreases for a fixed value of M. Furthermore it can be shown that the mixing between the ν_L and ν_R approaches zero, with $\nu_1 \rightarrow \nu_L$, and $\nu_2 \rightarrow \nu_R$. The single flavor generation is left containing two essentially independent states, with an enormous mass difference.

The masses M, m_R, and m_L depend on the strengths of the various couplings assumed to generate them. M is usually taken to be on the order of the Standard Model mass scale, and many models beyond the Standard Model posit a ν_R satisfying the requirements in equation 1.19. This picture is called the seesaw mechanism, and is perhaps the best way to explain the observed smallness of neutrino masses. Furthermore, when the seesaw mechanism is generalized to three flavor generations, the masses of the light, left–handed neutrino partners in each generation are predicted to be in the relation:

$$m(\nu_1) : m(\nu_2) : m(\nu_3) = \frac{m_u^2}{M_R} : \frac{m_c^2}{M_R} : \frac{m_t^2}{M_R} \tag{1.20}$$

in other words, in the same hierarchical arrangement as that observed among the charged quarks[4].

1.5 Cosmological Implications of Massive Neutrinos

Neutrinos from any one of the flavor generations, if sufficiently massive, could have far–reaching cosmological effects, assuming that neutrino lifetimes are on the order of the current age of the universe and the validity of "Big Bang" models of cosmological evolution [15].

[4]This assumes the masses of the right–handed (heavy) neutrinos in each flavor generation to be essentially the same. Also, whether the quark or lepton mass hierarchy is assumed depends on the model under consideration. See reference 2, p. 96.

One class of models, based on the assumption that the universe is homogeneous and isotropic, leads to a solution of the field equations of General Relativity which describes the uniform expansion of the universe in time. This is consistent with observed recessional velocities of distant galaxies. An important parameter in these models is the critical mass density. If the true mass density of the universe is equal to the critical density, gravitational forces are just strong enough so that they will eventually bring the expansion of the universe to rest. In this case the universe is said to be "flat." If the true density is less than the critical density, expansion will continue indefinitely ("open" universe); if the true density is too large, the universe is "closed" and will eventually collapse.

A particularly attractive model, "inflation," developed to resolve various problems with the initial conditions of cosmological expansion, predicts a flat universe. The observed amount of luminous matter in the universe, however, can only account for about 1% of the total mass needed to attain the critical density. The amount of non–luminous matter inferred from galactic rotation curves would appear to account for another 30% at most.

One possible solution is that neutrinos make up, at least in part, the remainder of the missing mass or "dark matter" needed to close the universe. The required neutrino mass can be estimated from the cosmological neutrino number density. This latter quality can be inferred, in turn, from measured values of the cosmic background radiation. In the inflationary model, the early universe is dominated by relativistic particles in thermal equilibrium with each other. While in equilibrium, the neutrino and photon number densities are in the ratio simply determined as that of the number density of a relativistic Fermi gas to a relativistic Bose gas (namely 3/4, assuming Majorana neutrinos). As the universe expands and cools, and the particles precipitate out of equilibrium, this ratio stays the same, although the photon number density increases later from other processes such that the final ratio is approximately 1/4. The present–day photon density (that of the 2.7 K cosmic background radiation) is measured to be approximately $400/\mathrm{cm}^3$, so that

the neutrino density is approximately $100/\mathrm{cm}^3$.

Assumimg the cosmological neutrinos to be massive enough such that they are non–relativistic in the present day, the required neutrino mass is simply the energy density divided by the number density. In the approximation that the neutrinos constitute most of the mass in the universe (simply equating the energy density to the critical density), the required neutrino mass is then:

$$m_\nu = 1 \times 10^4 H_{100}^2/110 \text{ eV}, \tag{1.21}$$

where H_{100} is the Hubble constant, expressed in the units 100 km s^{-1} Mpc^{-1}. In these units, $H_{100}^2 \simeq 0.5 - 1.0$, so that this cosmological model favors neutrino masses on the order of 10-100 eV.

A conservative assumption would be that the heaviest neutrino (most likely the ν_τ, according to the seesaw mechanism) has at least the minimum mass ($\simeq 10$ eV) required. Assuming that neutrinos oscillate, these results suggest that neutrino oscillation experiments sensitive to ν_τ masses of 10 eV, at reasonably small mixing angles[5], are in order.

1.6 Neutrino Oscillation Experimental Strategy

Neutrino oscillation experiments generally fall into two basic categories. In a *disappearance* experiment, a detector sensitive to a particular kind of neutrino interaction is exposed to a low–energy neutrino source. A measured deficit in the neutrino flux from the expected value is interpreted as the result of the transformation of the source neutrinos into heavier flavor neutrinos which, due to their low energies (usually on the order of 1 MeV), are not capable of producing the corresponding charged

[5]In the Standard Model, quark mass eigenstates are not equivalent to the weak states, and the degree of quark mixing is described by the CKM matrix, not discussed this chapter. One possible handle on the size of the neutrino mixing angles is the expectation that these parameters be of the same order as the quark mixing angles, the latter of which are measured to be in the range .002–.9993

leptons in the detector, by which products the presence of the oscillation final–state neutrinos is inferred.

The solar ν_e experiments (section 1.2) can be interpreted as disappearance experiments. Similar large, underground detectors search for deficits in expected ν_μ fluxes resulting from cosmic ray interactions in the atmosphere. Still other experiments are constructed to look for deficits in the expected rates of interactions induced by neutrinos produced in nuclear reactors.

In higher-energy experiments (typically 1-50 GeV), a detector is placed in a very well–characterized ν_μ beam produced in an accelerator. The experiment looks for the *appearance* of anomalously large numbers of final–state charged leptons other than muons.

In all oscillation experiments, measured deviations from the expected neutrino fluxes can be translated into oscillation probabilities (section 1.3). As of this date, no signals from well–characterized sources (accelerators and reactors) have been observed, with the possible exception of the LSND experiment at Los Alamos. The experiments therefore quote probability limits. Given the two unknown parameters in the probability (the mass difference and mixing angle), the results are usually expressed as contours (and the limits as excluded regions) in the $(\Delta m^2, \sin^2 2\theta)$ parameter space.

For a particular experiment, sensitivity to the mass difference depends on the ratio of the source–detector distance to the neutrino energies involved. From equation 1.15, neutrino oscillations occur over a periodic length

$$L_{osc} = E/1.27\Delta m^2 \tag{1.22}$$

where L_{osc} is in meters, E in MeV, and m in eV. Solar neutrino experiments, for example, with $L \simeq 1 \times 10^{11}$ m and $E \simeq 1$ MeV are sensitive to $\Delta m^2 \simeq 1 \times 10^{-11}$ eV^2. "Short–baseline" accelerator experiments, with $L \simeq 1$ km and $E \simeq 10$ GeV are sensitive to $\Delta m^2 \simeq 10$ eV^2. On the other hand, the sensitivity of a particular experiment to the mixing angle depends on the accumulated statistics, very low

for most experiments relative to the accelerator experiments. As a result, the different classes of experiments tend to probe very different regions of the oscillation parameter space.

One set of limit curves, for accelerator–based experiments probing for the oscillation $\nu_\mu \to \nu_\tau$, is shown in figure 1.2 [16]. The region above and to the right of a given curve is excluded at the 90% confidence level. The projected limit curve (assuming no oscillation signal is observed) for the NOMAD experiment, the subject of this study, is shown along with that of the complementary experiment CHORUS. Based on these curves, NOMAD should be sensitive to a massive ν_τ of cosmological interest, assuming a mixing angle larger than $\simeq 5 \times 10^{-4}$.

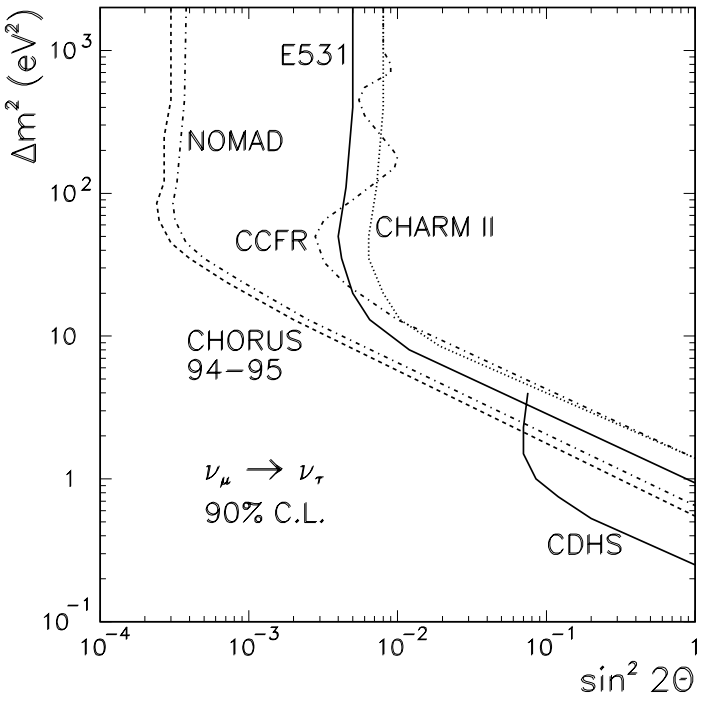

Figure 1.2: Limit curves for $P(\nu_\mu \to \nu_\tau)$ from accelerator–based experiments. The areas above and to the right of each curve are excluded at the 90% confidence level.

1.6.1 Overview of the NOMAD Experiment

As appearance experiments, NOMAD (Neutrino Oscillation MAgnetic Detector) and CHORUS (CERN Hybrid Oscillation Research apparatUS) are designed to identify final–state τ–lepton events produced in a neutrino beam composed almost exclusively of ν_μ and ν_e. More specifically, the experiments are designed to detect charged–current (CC) events of the form:

$$\nu_\tau + N \rightarrow \tau^- + X \tag{1.23}$$

where N is a target nucleon and X consists either of the nucleon or its fragments, plus other by–products of the reaction. At the energies typical of the neutrino beam (in this case produced by the Super Proton Synchrotron accelerator at the CERN laboratory near Geneva, Switzerland), any τ produced from a ν_τ is expected to travel on the order of 1mm before decaying. At first glance, an obvious choice of detector technology would be one providing for charged–particle track resolution much finer than 1mm. This determined the design of the CHORUS detector, which hopes to identify the actual final–state τ tracks in layers of photographic emulsion. The analysis of emulsion is, however, a slow and expensive process.

The NOMAD experiment uses a different approach, and consists exclusively of components which can be read out electronically (chapter 3). The principal tracking detector, a series of drift chambers, has resolution on the order of 1mm, so that final–state τ events cannot be identified via the τ track. Instead, NOMAD attempts to identify the subsequent decays of the τ^- in equation 1.23, using kinematic criteria.

NOMAD is designed to be able to identify τ events via most of the decays which occur with branching ratios on the order of 10% or more. These include the principal leptonic modes, $\tau^- \rightarrow e^- \nu_\tau \bar{\nu}_e$ and $\tau^- \rightarrow \mu^- \nu_\tau \bar{\nu}_\mu$, and the hadronic modes $\tau^- \rightarrow \pi^- \nu_\tau$, $\tau^- \rightarrow \pi^- \pi^+ \pi^- \nu_\tau$, and $\tau^- \rightarrow \rho^- \nu_\tau$. The limit curve in figure 1.2 is derived assuming that no τ events are detected in the combined search for *all* of these decays, in a sample of roughly 1.1×10^6 recorded neutrino events. The upper limit obtainable from each separate decay mode can be roughly estimated by

dividing the total limit by the branching ratio for that decay (usually between 0.1 and 0.2).

In general, the details of the analyses developed to identify the separate decays are different. However, several channels make use of similar kinematic criteria. The most sensitive criteria used to distinguish leptonic τ^- decays is based on the direction of the momenta of final–state leptons in the plane transverse to the beam direction. In typical CC ν_μ and ν_e interactions, this transverse momentum (p_T) of the final–state μ^- or e^- is expected to balance that of the hadronic jet (that is, of the analog of "X" in equation 1.23 above). Any transverse momentum imbalance, or "missing-p_T," due to unreconstructed neutral particles or measurement errors, is expected to be distributed randomly. In ν_τ CC events in which the τ^- subsequently decays into a lepton, however, two more neutrinos are produced in the decay, which cannot be reconstructed. The missing p_T in these events, due to the decay neutrinos, is expected to balance the hadronic jet p_T much more often than in ν_μ and ν_e events, while the final–state lepton p_T is expected to be distributed more randomly. The transverse momenta relationships in simulated (Monte-Carlo) standard and $\tau^- \rightarrow$ lepton events are illustrated in figure 1.3.

In the absence of any ν_τ source to evaluate the efficiency of the kinematic criteria in selecting ν_τ events from background ν_μ and ν_e events, the experiment relies heavily on a complete computer simulation, or experimental model, of ν_τ and standard events in the detector (chapter 5). The model is crucial for understanding the ways in which the kinematics of ν_μ and ν_e events can mimic those of signal events, for example via the mis–reconstruction of decay tracks, or scattering and attenuation effects in the target.

The focus of this study is a search for $\nu_\mu \rightarrow \nu_\tau$ oscillations via the decay $\tau^- \rightarrow \mu^- \nu_\tau \bar{\nu}_\mu$. The decay channel through which NOMAD will most likely attain the highest sensitivity to ν_τ events is $\tau^- \rightarrow e^- \nu_\tau \bar{\nu}_e$. This is due to the composition of the neutrino beam; the 1% admixture of ν_e in the predominantly ν_μ beam leads to a corresponding 100-fold decrease in the CC background for the $\tau^- \rightarrow e^- \nu_\tau \bar{\nu}_e$ channel.

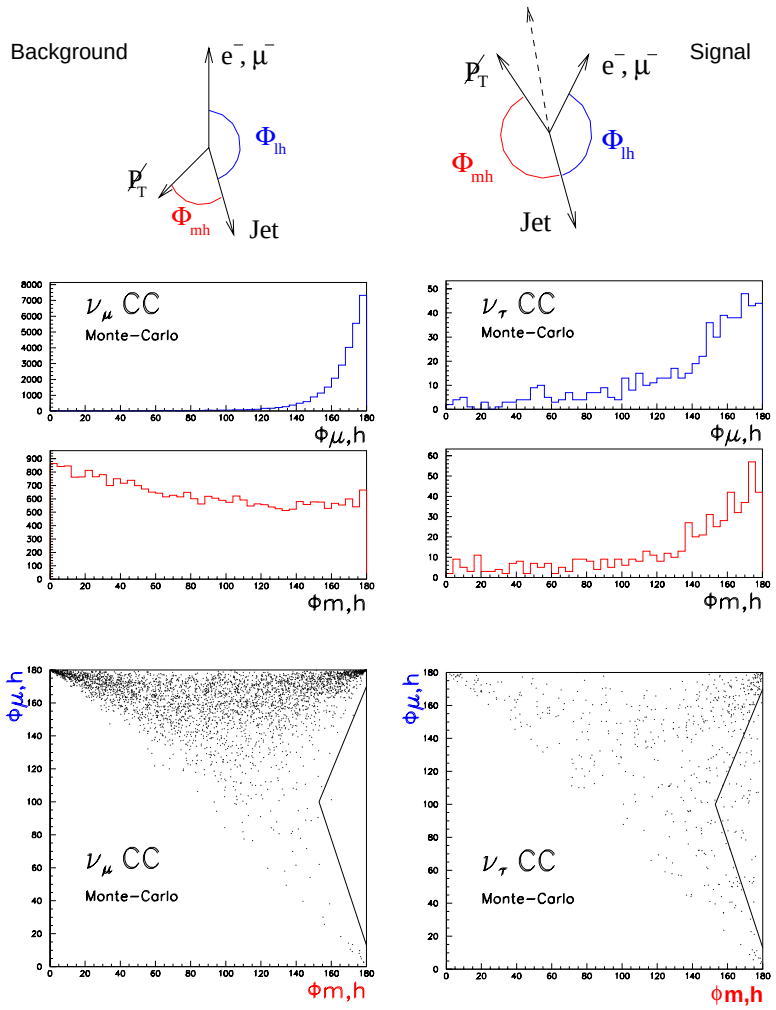

Figure 1.3: Top: momenta relationships in the transverse plane for CC ν_μ and ν_e events (left) and $\tau^- \rightarrow$ lepton events (right). Middle: Distributions of azimuthal angles between the final state lepton p_T and the jet p_T ($\phi_{l,h}$), and that between the missing-p_T and the jet p_T ($\phi_{m,h}$). Bottom: $\phi_{l,h}$ vs. $\phi_{m,h}$; these so–called "$\phi - \phi$ plots" (and their variants) are the most sensitive criteria used to isolate ν_τ events in NOMAD.

The search strategies for both leptonic channels are very similar, however, so that the higher statistics in the $\tau^- \to \mu^- \nu_\tau \bar{\nu}_\mu$ channel offers an excellent opportunity to establish how well the experimental model and backgrounds are understood.

Chapter 2

Neutrino Source and Beam Characteristics

Neutrino oscillation experiments of the appearance type are made possible by beams produced at accelerators. The high energy enables the production of final–state muons and tau leptons, which cannot be produced in sufficient quantities by reactor or natural sources.

An accelerator neutrino source consists of three basic components. The first is a high–energy proton beam, which is directed at a fixed target. The second component consists of the pions and kaons produced in the target, which decay to produce the third component, the actual neutrinos. The NOMAD experiment is located the CERN West Area Neutrino Facility (WANF), which receives protons from the SPS (Super Proton Synchrotron). A detailed description of the CERN neutrino facility may be found in reference 18; the summary below follows reference 17.

2.1 Primary Beam

A fast–extracted proton beam from the CERN SPS constitutes the NOMAD primary beam. Protons are injected into the SPS and accelerated to 450 GeV. Shortly before

the maximum energy is reached, part of the beam is extracted at 445 GeV, over a duration of about 6 ms, onto a beryllium target. This provides the first neutrino spill. The beam is then directed to other experiments over a 2.4 second duration, or "flat-top" (referring to the steady, maximum current maintained in the SPS magnets during this interval), during which NOMAD receives a substantial flux of muons. At the end of the flat-top, the remainder of the SPS beam is directed to the beryllium target, providing a second 6 ms neutrino spill. This cycle repeats every 14.4 s, and is illustrated in figure 2.1.

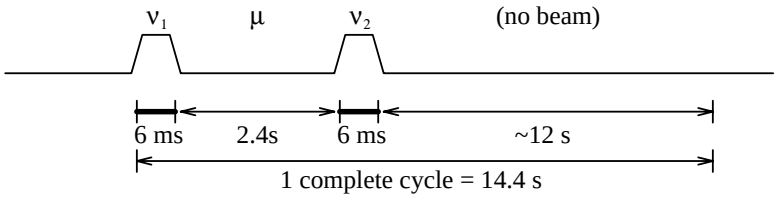

Figure 2.1: Time structure of the CERN SPS extraction. Proton intensity on the neutrino target (arbitrary units) is plotted vs. time. ν_1 and ν_2 refer to the neutrino spills. During the "μ" window, NOMAD receives a substantial muon flux

The intensity of the proton beam is monitored with a series of beam current transformers (BCT), in which a current is induced by the passing protons. A typical neutrino spill consists of about 1×10^{13} protons-on-target ("p.o.t."), and has a gaussian cross-section with $\sigma \simeq 5$mm.

2.2 Secondary Beam

The protons from the SPS interact in the target to produce mesons and other particles. The mesons, particularly charged pions and kaons, are then focused, and their decays produce the neutrino beam. The WANF beam line is illustrated schematically in figure 2.2.

The target consists of 11 beryllium rods, each 10 cm long and 3 mm in diam-

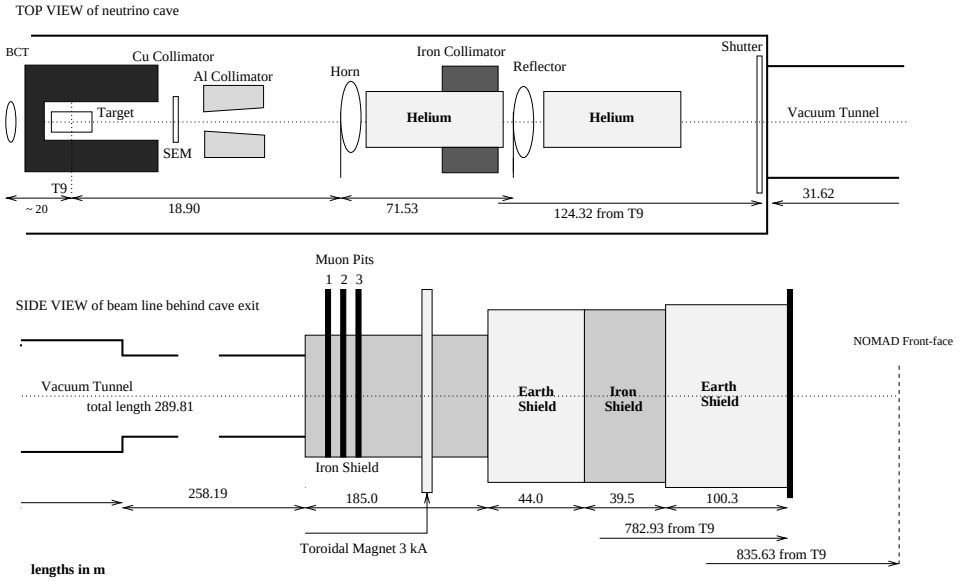

Figure 2.2: Schematic view of CERN West Area neutrino beam line

eter, oriented longitudinally along the proton beam and separated by 9 cm gaps. Approximately 93% of incident protons interact in the target. Mesons leaving the target at high angles are absorbed in an aluminum collimator.

Positively charged pions and kaons are then focused by a pair of magnetic lenses, the horn and reflector. Each consists of two coaxial conductors, carrying equal and opposite currents. Each is synchronized with the SPS operation such that the maximum current (about 140 kA) is maintained during the neutrino spills.

The sections between the horn and reflector, and between the reflector and decay tunnel, are enclosed in helium tubes 80 cm in diameter in order to reduce the absorbtion of the secondary particles. An iron collimator is installed after the horn to reduce the antineutrino contamination in the beam, by intercepting de-focused negative secondaries before they decay.

Most of the focused pions and kaons decay in a 290 m vacuum tunnel, plugged at the far end with iron and earth shielding to absorb remaining muons and hadrons. A

toroid magnet located at the iron shield sweeps large–angle muons back into the iron and earth. The remaining particles reach the CHORUS and NOMAD experiments, located in the old Big European Bubble Chamber Hall near the end of the CERN West-Area beam line. NOMAD is located approximately 835 m from the target, and the average distance between the meson decay point and NOMAD is 620 m.

Monitoring elements in the beam line include a secondary emission monitor (SEM) behind the target, which measures the flux and profile of the secondary beam, and a series of solid–state detectors at three positions ("pits") in the iron shield. These detectors provide an absolute flux measurement of the beam, calculated from the sampled muon flux. To insure beam quality during the operation of NOMAD, information from the monitoring elements is constantly checked by NOMAD shift crews, and saved on NOMAD data tapes.

2.3 Neutrino Beam Simulation and Flux Calculation

Since the amplitude of the neutrino oscillation signal is a function of the source–detector distance, an ideal experiment would measure the neutrino flux at several different longitudinal positions along the beam. The flux measurement at the first position is then the prediction for the second; a variation in the (acceptance–corrected) measured amplitude of the oscillation final state would be a signal for neutrino oscillations.

This is true, however, only for oscillation experiments in which the oscillation final state is expected to constitute a significant portion of the neutrino beam due to standard processes. The ν_τ content of the CERN wide band beam due to known physics processes is expected to be unobservable (section 2.3.2), so that any ν_τ signal of reasonable significance can be taken as evidence for oscillations.

In the case of the anticipated $\nu_\mu \rightarrow \nu_e$ measurements in NOMAD, electron neutrinos are expected to constitute about 1% of the beam. Since the re-location of the NOMAD detector is not possible for technical reasons, an accurate calculation

of the ν_e component of the beam based on a priori knowledge is necessary. This is accomplished with a detailed Monte Carlo simulation, the main features of which are summarized here. The $\nu_\mu \to \nu_e$ measurement aside, the beam simulation is also the first step in the complete NOMAD experimental model (chapter 5), central to the understanding of event selection efficiencies and backgrounds. An excellent description of the neutrino beam simulation can be found in reference 19.

2.3.1 Standard Beam Composition

The Monte Carlo begins with a detailed simulation of proton interactions in the beryllium target, and continues with the passage of mesons through the beam line. The original program, based on the CERN-developed package GEANT ([20] and see section 5.2), derives from a Monte Carlo adjusted to spectra measured at the CHARM II experiment at CERN, known as GBEAM+.

Since the generation of event samples with GBEAM+, several corrections have been implemented in the program to optimize it for NOMAD, resulting in the NUBEAM program. NUBEAM relies on the FLUKA package [21] for simulating hadronic interactions, which has substantial input from experimental data. The Monte Carlo samples used in this study are generated with GBEAM+ and corrected to the NUBEAM results with a re-weighting procedure (section 5.4).

The energy spectra from a NUBEAM study using 10^9 simulated p.o.t. and a NOMAD fiducial area of 2.6×2.6 m^2 are shown in figure 2.3. The radial distribution is shown in figure 2.4. Expected mean energies and relative abundances of each neutrino species at NOMAD are listed in table 2.1, assuming the 2.4×10^{19} p.o.t. (anticipated over two years of data taking) originally requested in the NOMAD proposal. The expected number of ν_μ CC events, 1.15×10^6, is used to compute the predicted rate measured in chapter 6.

The principal uncertainty in the calculated fluxes arises from the limited knowledge of the yields of pions and kaons from 450 GeV proton interactions in the target. Since electron neutrinos arise only from kaon decay (and some muon contamination),

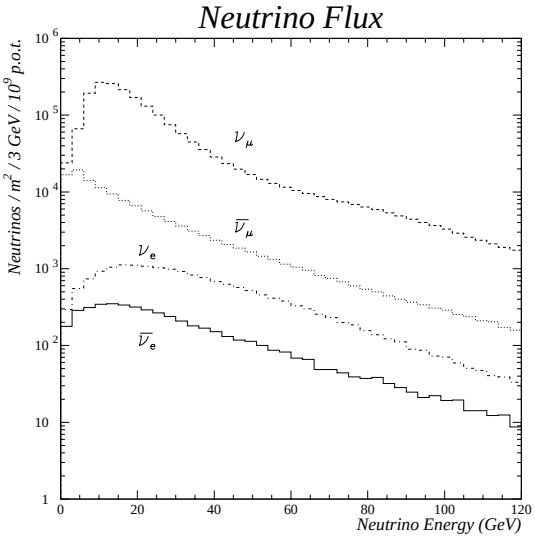

Figure 2.3: Predicted energy spectra of neutrinos at NOMAD

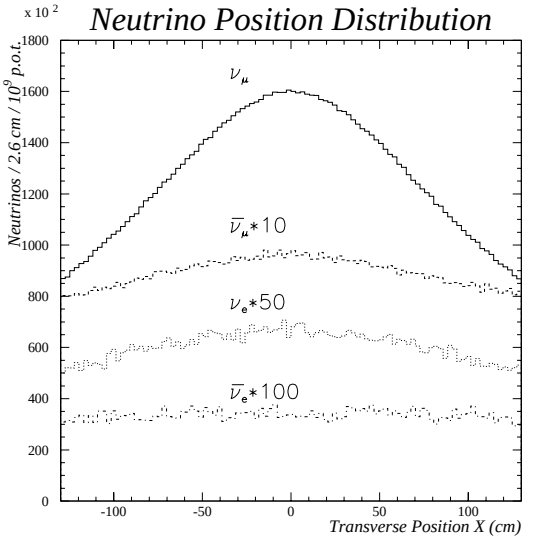

Figure 2.4: Predicted profile of neutrino beam at NOMAD. The distribution is symmetric in the other transverse coordinate.

Source	*Average E (GeV)*	*Relative Flux*	$N_{\nu CC}$
ν_μ	23.6	1.000	1.15×10^6
$\bar{\nu}_\mu$	22.7	0.070	0.39×10^5
ν_e	37.0	0.010	0.17×10^5
$\bar{\nu}_e$	33.2	0.003	0.22×10^4

Table 2.1: Predicted energy, relative abundance, and absolute number of charged-current events for 2.4×10^{19} p.o.t. and a NOMAD fiducial area of 2.6×2.6 m^2.

the correct ratio of these yields is a critical parameter for predicting the ν_e content of the beam, crucial to the NOMAD $\nu_\mu \to \nu_e$ oscillation analysis. The reduction of this uncertainty is a principal motivation for the SPY (Secondary Particle Yields) experiment at CERN, which directly measures the yields at NOMAD energies.

2.3.2 Tau Neutrino Content

The search for the oscillation $\nu_\mu \to \nu_\tau$ is less dependent on accurate flux predictions since the ν_τ component of the beam due to standard physics sources, which would constitute irreducible background, is expected to be negligible. In the West Area beam line, tau neutrinos are produced primarily via the reactions:

$$\begin{aligned} p + N \to \quad & D_s^+ + X \\ & D_s^+ \to \quad \tau^+ + \nu_\tau \\ & \qquad\quad \tau^+ \to \bar{\nu}_\tau + X' \end{aligned} \tag{2.1}$$

and the corresponding charge–conjugated processes. Due to threshold effects, the production of charmed D-mesons is relatively rare compared to lighter mesons, and the short lifetime ($c\tau = 140\mu$m) prevents the Ds produced in the target from reaching the horn.

A calculation of the rates of the above processes, considering production both at the target as well as in the iron at the end of the decay tunnel, has been carried out [22]. The expected ν_τ flux interacting in NOMAD, relative to the ν_μ flux, is 5×10^{-6}.

Assuming selection efficiencies on the order of a few percent, this corresponds to less than one observed ν_τ event over the expected course of the NOMAD experiment.

Chapter 3

The NOMAD Detector

3.1 Overview

The main purpose of the NOMAD detector is the identification of τ–lepton production events via the τ decay products. This must be accomplished with high efficiency and good discrimination against background. The τ decay products of interest are muons, electrons and pions, therefore the identification of these particles is a priority, as is the rejection of tracks which fake them. Since τ candidate events are identified with kinematic criteria based especially on transverse momentum balance (section 1.6.1), both charged particle momenta and energy due to photons must be measured with good precision.

These and other requirements led to the design shown in figure 3.1. The NOMAD detector consists of a series of drift chambers followed by a transition radiation detector (TRD) flanked by two planes of scintillation counters, behind which is placed a preshower detector and a lead-glass electromagnetic calorimeter. These subdetectors are placed inside a large dipole magnet recycled from the UA1 experiment, which has a field of 0.4 T along the x-direction (into the plane of the figure). The front and rear magnet sections are instrumented with scintillator for additional calorimetry. Additional scintillator planes are placed in front for a charged–particle

veto, and large–area drift chambers, also recycled from UA1, are placed at the rear for muon identification. The essential features and function of each subdetector are described below. For a more complete description, see reference 17.

3.2 Drift Chambers

The drift chambers serve two purposes of central importance to the NOMAD experiment. First, they provide for the tracking of charged particles from neutrino interactions, measuring the momentum and charge of these particles from the curvature of the tracks in the magnetic field. Second, they serve as the principal neutrino target.

These two requirements are in conflict. For tracking, the chambers must be constructed from low density, low atomic number (Z) materials in order to minimize effects such as secondary interactions, multiple scattering, and radiative energy loss. The number of neutrino interactions in the target, however, is proportional to the number of target nucleons, so a material of sufficiently high Z and density is needed to achieve the required statistics.

The final design chosen is illustrated schematically in figure 3.2 (top). Each chamber consists of four 3×3 m^2 aramid-fiber panels sandwiched by Kevlar skins. The three 8 mm gaps are each equipped with a series of sense wires, interleaved with field–shaping wires which define drift cells of ± 3.2 cm around each sense wire (figure 3.2, bottom). The wires in the central gap are at 0 degrees with respect to the magnetic field direction, and those in the outer gaps are at ± 5 degrees. Aluminum cathode strips, each 2.8 mm wide separated by 1.2 mm, are printed on mylar glued to the panels. The gaps are filled with an argon–ethane gas mixture (40%–60%).

A total of 44 chambers are grouped into 11 modules of 4 chambers each, and installed in the front of the magnet. This arrangement has a mass of 2.7 tons assuming a fiducial area of 2.6×2.6 m^2, and is longitudinally slightly shorter than one electron radiation length. In addition, 5 chambers are placed individually in between

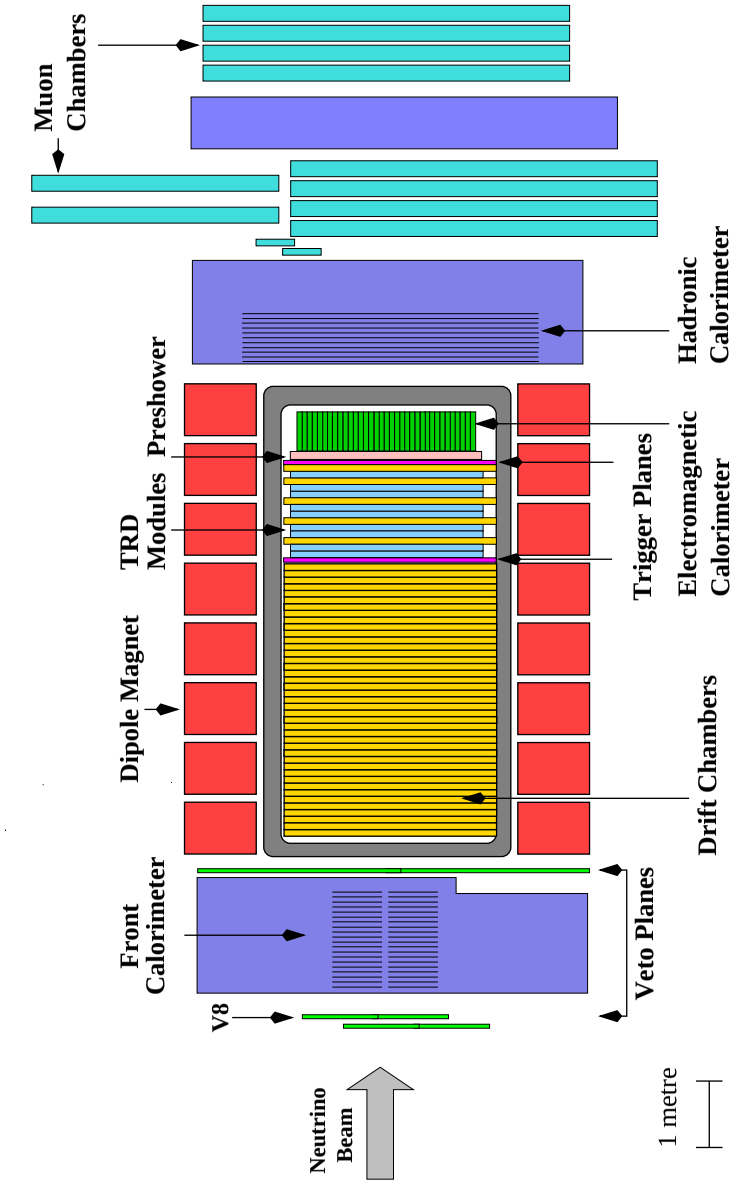

Figure 3.1: Side view of the NOMAD detector ($y - z$ plane, where z is along the beam direction

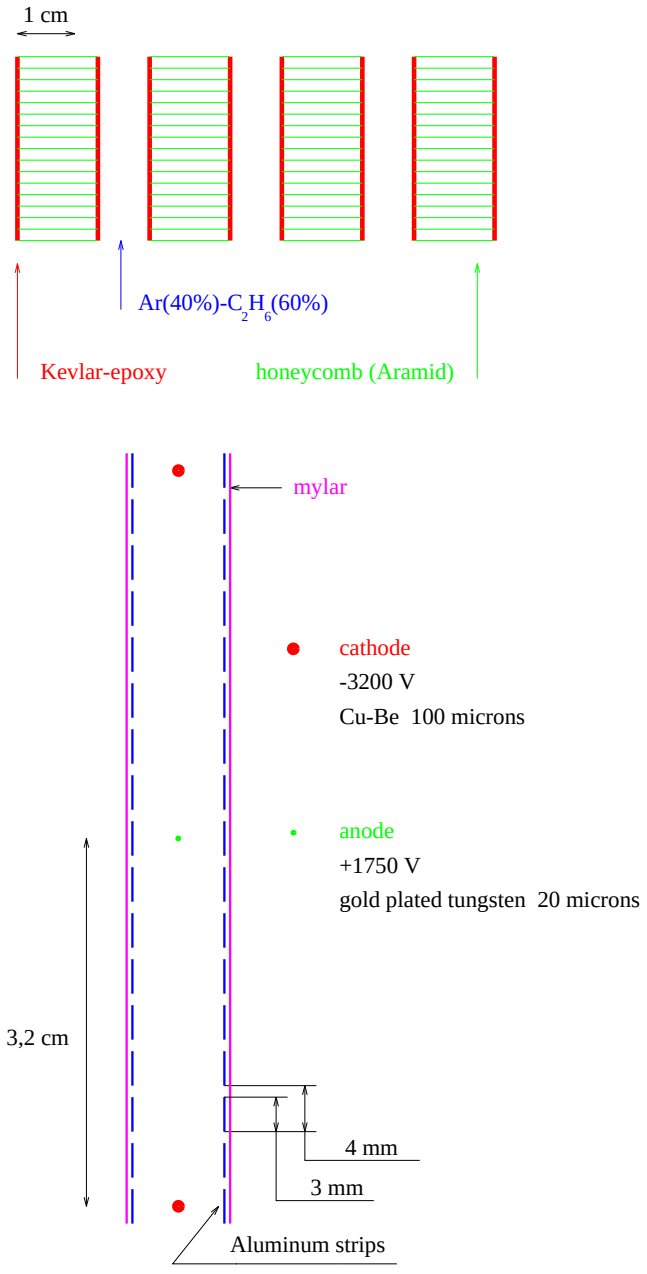

Figure 3.2: Construction of the NOMAD drift chambers

modules of the TRD to improve track extrapolation to the other subdetectors.

The chambers are operated 100 V above the edge of the plateau, where the hit efficiency is measured to be 97%. Signals are fed into a preamplifier and a fast discriminator, and digitized in a TDC (LeCroy 1876). The spatial resolution is measured to be from about 150 μm for straight-through tracks, to about 700 μm for tracks at polar angles of 40 degrees. The momentum resolution ranges from about 2.7% for 1 GeV tracks 3.5 m in length, to about 15% for 50 GeV tracks 1.5 m in length.

3.3 Trigger and Veto Counters

To ensure the efficient pre-selection of events of interest during the real–time operation of the detector, two trigger planes are installed in the NOMAD detector, and a charged–particle veto installed in front. Each trigger plane plane is made up of 32 scintillation counters. 24 counters, each 124 cm $\times$ 19.9 cm $\times$ 0.5 cm, are installed horizontally. 4 additional counters, each 130 cm long, are installed vertically at the edges of the horizontal stack to increase the total fiducial area. The counters are connected via lightguides to photomultipliers oriented parallel to the magnetic field. A complete plane is illustrated in figure 3.3. Signals are discriminated and fed into a coincidence unit (LeCroy 4564), which forms a logical OR of all counters. Signals are also sent to a TDC, for the determination of individual counter timing.

One plane of scintillation counters ("T1") is placed immediately behind the target drift chamber modules, and a second ("T2") behind the TRD. The efficiency of the counters for single tracks is measured to be 97.5%.

The NOMAD veto consists of 59 scintillation counters at the front of the detector. The counters are 2 cm thick and 21 cm wide, and come in two lengths (300 and 210 cm). Most are read out with photomultipliers on both ends. Signals are fed into mean–timers which produce a logical OR of all counters, and into TDCs for the timing of individual counters.

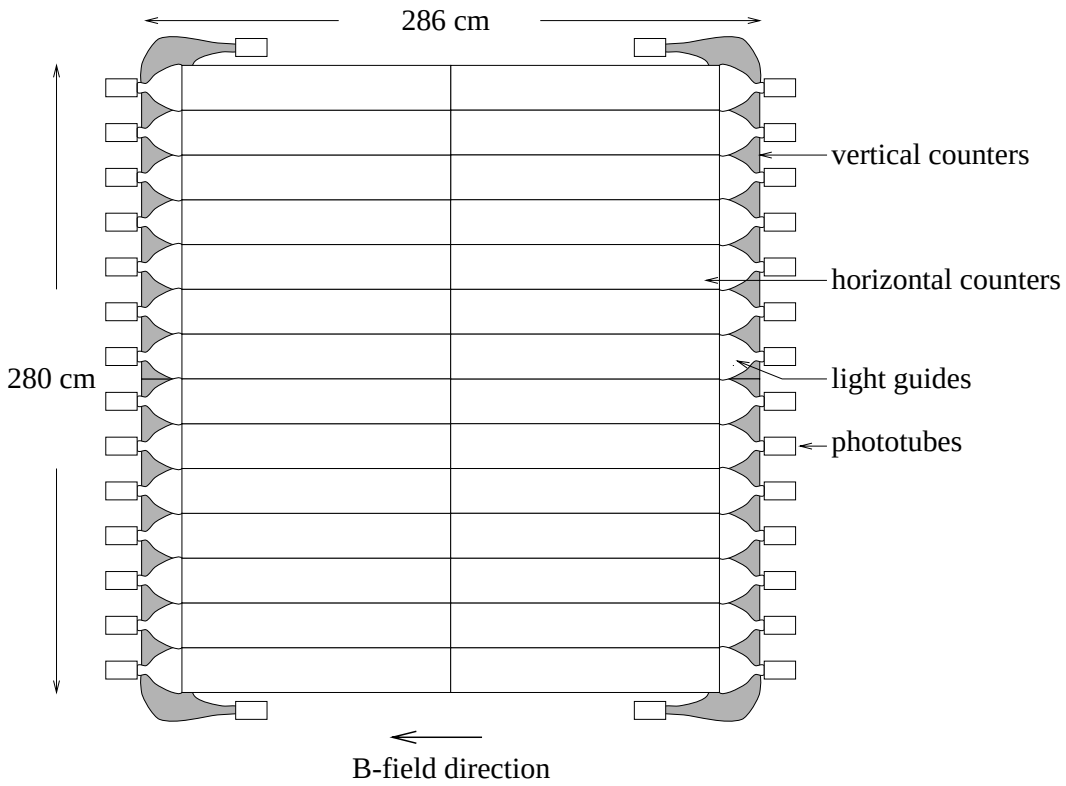

Figure 3.3: Front view of a trigger plane

The arrangement of the veto counters is optimized to provide rejection against charged particles produced upstream and in the front magnet support, and against large–angle cosmic rays (see figure 3.1). In this configuration, the charged particle rejection efficiency is measured to be about 96%.

The basic trigger signal for neutrino interactions in NOMAD consists of at least one hit in T1 in coincidence with a hit in T2, in anti-coincidence with the veto. More complicated signals for other physics processes, defined with parts of the trigger and veto in conjunction with other subdetectors, are also used.

3.4 Transition Radiation Detector

In neutrino neutral current (NC) interactions, a final–state neutrino is produced on the leptonic side of the decay and results in substantial missing-p_T opposite to that of the jet. A principle background to the electronic decay mode of the τ lepton, therefore, consists of NC interactions in which a final state pion from the hadronic jet is misidentified as an electron. The NOMAD transition radiation detector is used to reject such events, by providing both a high pion rejection factor and electron identification efficiency.

Each TRD module consists of a radiator and detection plane. The radiator is made of 315 polypropylene foils, each 15 μm thick and 3×3 m^2 in area, separated by air gaps of 0.25 mm. The detection plane consists of 176 aluminized mylar straw tubes, arranged vertically, each 3 m long and 16 mm in diameter, separated by 0.2 mm. Each tube is fitted with an anode wire and filled with a gas mixture of 80% xenon and 20% methane.

Eight modules are arranged into four doublets and installed behind the first NOMAD trigger plane. An additional drift chamber (section 3.2) is placed behind each doublet for improved track extrapolation. One more module and chamber completes the arrangement, part of which is illustrated in figure 3.4.

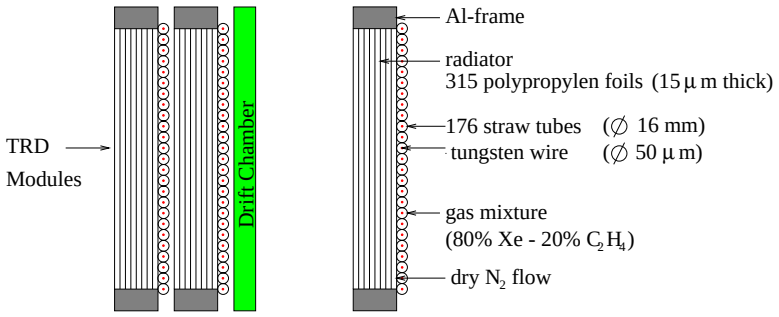

Figure 3.4: Top view of TRD modules with additional tracking chamber

The straw tubes are operated in proportional mode and read out with charge–

integrating ADCs. Electron–pion discrimination in the TRD is based on the difference in energy deposition in the straw tubes from particles of different Lorentz factors ($\gamma = E/m$). For pions and muons at typical NOMAD energies ($\simeq$ 10GeV), $\gamma \simeq 100$ and most of the energy deposit is due to ionization in the gas mixture. For electrons, $\gamma \simeq 10^4$, well above the range ($\gamma \simeq 1000$) in which charged particles begin to produce transition photons (X–rays) at the interfaces of the foils. In the NOMAD TRD, a typical electron at a detector straw is accompanied, on average, with 3 radiation photons of energy 14 keV. This results in a significantly harder and broader energy spectrum for electrons than for pions. This is illustrated in figure 3.5, for muons and electrons. With all 9 TRD modules, a pion rejection factor of 1000 is achieved, with an electron identification efficiency of 90%.

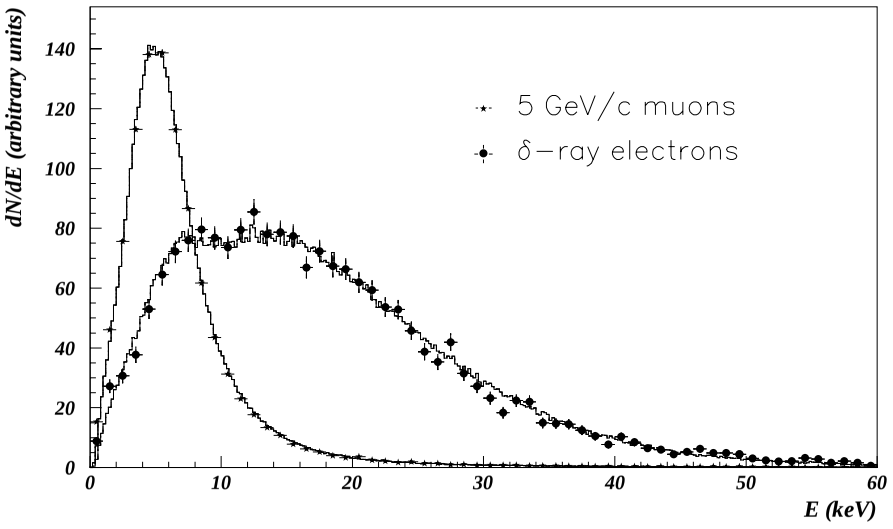

Figure 3.5: Energy deposit from 5 GeV muons (stars) and 2 GeV electrons (solid points) in the TRD. Solid lines are results from simulation.

3.5 Electromagnetic Calorimeter

The identification and measurement of final–state electrons in neutrino interactions is greatly enhanced by a high–acceptance electromagnetic calorimeter (ECAL) [23]. This detector is also important for measuring the neutral component (due to photons) of the transverse momentum of final state particles from these interactions, which is central to the identification of τ–decay candidates.

To obtain good energy resolution over a wide range ($\simeq 10^2 - 10^5$ MeV), the calorimeter is constructed from lead-glass blocks. Each block measures 79 mm $\times$ 112 mm $\times$ 494 mm, equivalent to about 20 radiation lengths. Each is read out with a 3-inch phototetrode, mounted on a sheared edge of the block at 45 degrees to the direction of the axis, in order to reduce the operational losses in the magnetic field. A cell of 9 blocks with phototetrodes is illustrated in figure 3.6. 875 blocks are arranged into 35 rows of 25 towers, so that the total calorimeter assembly measures 280 cm $\times$ 277 cm, and has a total mass of about 20 tons.

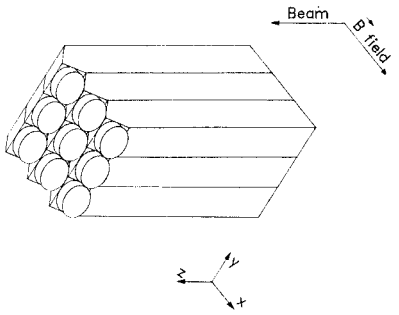

Figure 3.6: Rear view of 9 lead glass calorimeter blocks, showing position of the readout tetrodes.

Tetrode signals are amplified, shaped, and fed into peak–sensing ADCs. Each block is monitored by two blue LEDs on both sheared edges, and is calibrated in a test beam of 10 GeV electrons. The spatial resolution of electromagnetic showers is measured to be about 4 mm, and the energy resolution is measured to be $\sigma_E/E =$

$.0104 + .0322/\sqrt{E(\mathrm{GeV})}$.

3.6 Preshower Detector

In order to enhance the conversion of photons to electron–positron pairs, and to improve electron/pion discrimination, a fine–grained preshower detector is installed immediately in front of the ECAL.

The preshower consists of a lead-antimony converter followed by two planes of proportional tubes. The converter is made from two lead sheets, each 45 mm thick and measuring 288 cm $\times$ 288 cm, which sandwich a 2 mm sheet of aluminum, for a total of about 1.6 radiation lengths. Each aluminum proportional tube is 9 mm wide and fitted with a 30 μm–diameter tungsten anode, and filled with an 80% argon–20% ethane gas mixture. A schematic of the assembly is illustrated in figure 3.7. There are 286 horizontal tubes measuring 291 cm in length, and 288 vertical tubes each 289 cm long.

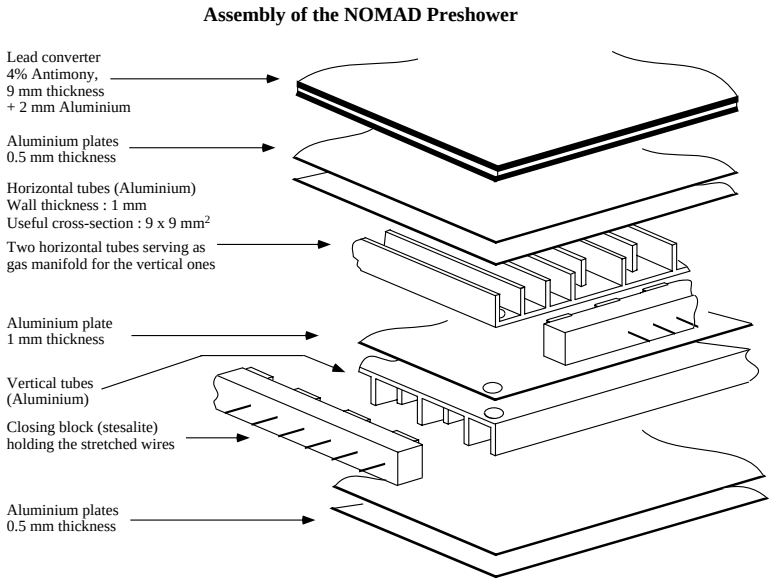

Figure 3.7: Construction of the preshower detector

Signals from the tubes are amplified and fed into charge–integrating ADCs. Approximately 70% of all photons measured in NOMAD convert in the preshower, the spatial resolution for which is approximately 1 cm, substantially finer than the dimensions of the ECAL blocks. For particle energies greater than 4 GeV, the pulse–height spectrum from the preshower can be used to identify electrons with 90% efficiency, with a pion contamination smaller than 10%.

3.7 Hadronic and Forward Calorimeters

In order to measure neutral hadrons, especially K_Ls and neutrons, which could carry transverse momenta of up to several GeV and contribute to τ event background, a hadron calorimeter is installed in the rear magnet support, behind the ECAL. The HCAL is also important for identifying photons whose ECAL energy deposit might otherwise be mis-associated to charged particles traversing the same ECAL blocks.

The HCAL is a sampling calorimeter consisting of alternating layers of iron absorber and active scintillator. The rear section of the NOMAD magnet, or 'magnet-I,' consists of 23 iron plates 4.9 cm thick and separated by 1.8 cm gaps, which provide the absorber layers. 11 scintillator slabs, each 1 cm thick, 360 cm long, and (on average) 18.3 cm high, are inserted into the first 11 gaps. The slabs are fanned together on both ends via light pipes onto 5-inch phototubes, so that the assembly forms a module approximately 3.1 interaction lengths deep. 18 modules are stacked vertically to cover an active area 3.6 m high and 3.5 m wide. A front view of the HCAL is shown in figure 3.8.

The photomultiplier signals are split. One is fed into charge–integrating ADCs for position and energy measurement, the other into TDCs for event timing. The (horizontal) spatial resolution for muons in the HCAL is measured to be about 20 cm.

In order to provide additional massive active target for neutrino interactions, and to address other physics topics, a similar sampling calorimeter is constructed

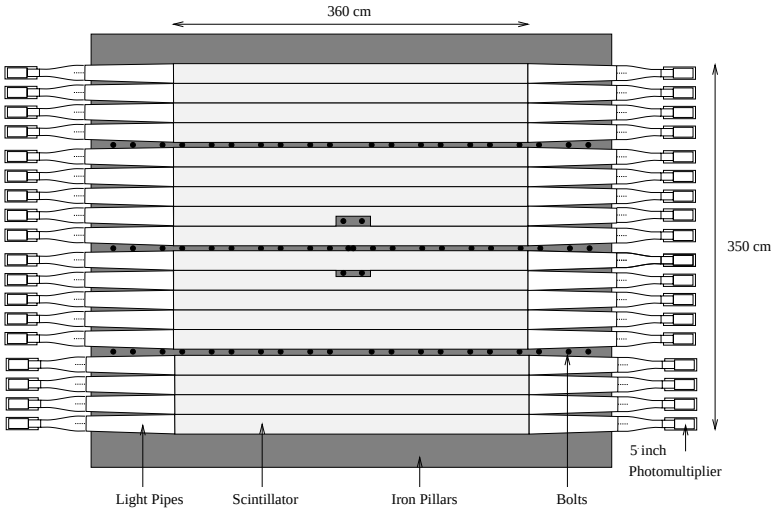

Figure 3.8: Front view of hadronic calorimeter

using the forward section of the magnet-I. Five scintillator slabs, each 0.6 cm thick, 175 cm long, and 18.5 cm high, are inserted into successive gaps. The slabs are fanned together on both ends via light pipes onto 3-inch phototubes, so that the assembly forms a module approximately 0.7 interaction lengths deep. 10 modules are arranged vertically to form a stack, covering an active area 1.9 m high and 1.75 m wide. 4 stacks are aligned in the magnet-I along the beam axis, as shown in figure 3.9, for a total mass of about 17.7 tons.

3.8 Muon Chambers

In order to provide for the identification of final–state muons essential to this analysis, 10 large–area drift chambers, previously used in the UA1 experiment, are installed at the rear of the detector. These chambers also provide a veto for the oscillation searches based on the other τ decay modes.

Each chamber contains four planes of aluminum drift tubes, with two planes of 48 tubes oriented along the length of the chamber and two planes of 73 tubes

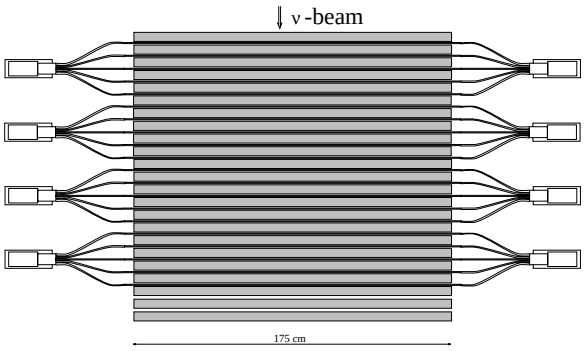

Figure 3.9: Top view of forward calorimeter

along the width. The long tubes measure 555 cm and the short tubes 375 cm; all have transverse dimensions of 14.9 cm $\times$ 4.4 cm. The planes are staggered by half a tube width in order to resolve left–right ambiguities, as illustrated schematically in figure 3.10. The maximum drift length is 7 cm, and the total active area per chamber is 3.75 $\times$ 5.55 m^2.

The chambers are arranged in pairs (modules), separated by gaps of 1 m, for track segment reconstruction. Two modules, oriented vertically are placed immediately behind the HCAL. A third module, oriented horizontally, is installed above the first two, completing the first station. The vertical modules are followed by an iron wall absorber 80 cm thick, behind which two more vertical modules are installed, forming the second station.

The chambers are filled with a gas mixture of 40% argon and 60% ethane, and operated at about 100V above the onset of the plateau. Signals are amplified and discriminated in preamplifiers on the end of each anode, and fed into TDCs. Track segments are reconstructed independently in each station, from 3 or 4 hits per projection (figure 3.10). For muons with energy greater than 5 GeV, the efficiency for track segment reconstruction is measured to be 97%, with a resolution of about 400μm.

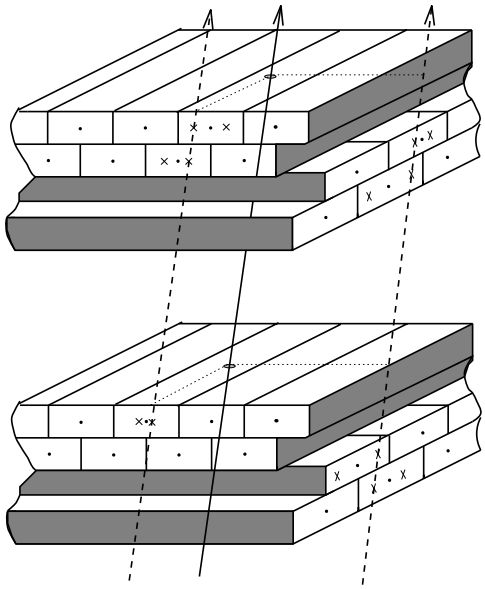

Figure 3.10: Schematic view of a section of muon chamber module. The solid line represents a muon. "×"-marks show the positions of recorded hits, from which the track segments in each projection (dashed lines) are reconstructed.

Chapter 4

Data Acquisition and Reduction

The CERN neutrino beam, described in chapter 2, delivers neutrinos in short bursts to NOMAD, a detector of nine active subsystems (chapter 3). The "on-line" data acquisition system (DAQ), described below, must be therefore be able to handle high event rates over short intervals and to synthesize information from many sources. For a more complete description of the DAQ, see reference 17.

Once on tape, the raw data must be decoded and assembled into the physics events for subsequent analysis. The "off-line" reconstruction programs, briefly outlined in this chapter, must accomplish this as completely as possible, and with good efficiency, to take advantage of the completely electronic readout. For detailed descriptions of the reconstruction algorithms, see references 25, 26, and 27.

4.1 Electronic Interface and Software

The DAQ is made sensitive to trigger signals for neutrino events (section 3.3) within small time windows centered around the neutrino spills. Two gates, synchronized with the SPS neutrino spills, are generated by a specially designed VME–based module, which performs all other trigger logic in NOMAD as well. An additional gate is generated for the flat–top. The module provides for the logical combination of up to 8 subdetector signals, and a maximum of 6 different trigger types, in each

of the gates.

The trigger used for the pre–selection of neutrino events is formed by a coincidence of the signals in each of the trigger planes, in anti-coincidence with the veto. The rate for this trigger is roughly 5.5 per 10^{13} protons-on-target. This translates into about 15 neutrino candidates per spill. Of the 5.5 events, about 0.5 are potentially interesting candidates for neutrino interactions in the active target; 2.5 are due to neutrino interactions in the magnet, 1.5 to non–vetoed muons, and 1 to cosmic rays. Triggers obtained in the 2.6 second flat–top between the neutrino spills are used to select muon events for alignment, calibration, and efficiency studies.

Signals from each of the subdetectors are digitized by some combination of three types of electronic modules, of the FASTBUS standard. These include 12-bit charge–integrating ADCs (of CERN design), 12-bit peak–sensing ADCs, and 16-bit TDCs (LeCroy type 1876 model 100; 1 ns resolution.) In order to minimize the dead time associated with burst–mode operation, the digitized information converted from the detector signals is buffered internally in the FASTBUS electronics and read out after the end of each spill.

Twelve FASTBUS crates in total are controlled by five VME–based cards (CES FIC 8234), which perform block transfers of available data to local buffers and assemble the data into sub-events. The sub-events are passed to a sixth FIC (the "event builder"), where they are assembled into complete events together with information about the state of the beam. Data are then written to a local disk from which, twice daily, they are transferred via network to a vault for storage on high–capacity tapes.

The data acquisition software is based on the CASCADE [24] package designed by CERN. Each of the VME controller cards, including the event builder, is run with a separate independent process known as a stage. An additional stage handles the disk recording.

The reliability and performance of each of the subdetectors, as well as the beam, is constantly verified with monitoring programs, which run on a network of Sun workstations. The programs connect to the stages and generate summary

histograms, which are systematically checked by shift personnel several times per day.

The operation of all stages and monitoring programs is managed with the run control program, implemented on a Sun in C++ with a simple graphical interface. Additional panels display information in real–time from the trigger module, error messages, and the status of the data transfer to the vault.

The control and monitoring of slowly–varying parameters, or "slow control," is handled with a network of several Apple Macintosh computers running Labview graphical software. The Macintoshes provide for control and monitoring of all high and low voltages, gas systems, temperature probes, etc., in the experiment, usually via CAMAC electronics. Slow control data are passed to a centralized Labview task running on a Sun workstation. Alarms are generated in the event of detector problems. Periodic samples of slow control data, along with all alarm records, are passed from the Sun to the event builder stage and saved for offline use.

A schematic of the DAQ is illustrated in figure 4.1. Altogether, the system records over 1.5 megabytes of data per minute, and about six times this quantity flows through in the form of calibration events which are not recorded. In the neutrino spills, the DAQ has a typical dead time of 10% arising from digitizations. Under normal conditions the system is fully automatic; down time and losses due to inter-run transitions is less than 3%.

4.2 Event Reconstruction and Selection

The reconstruction and selection of neutrino events from the raw data is performed primarily on a cluster of approximately 30 Digital Alpha workstations. The process involves several steps:

1. *Preliminary tracking and vertex location:* The raw data from the drift chambers is unpacked and passed though basic track and vertex finding algorithms, primarily for the purpose of the next step.

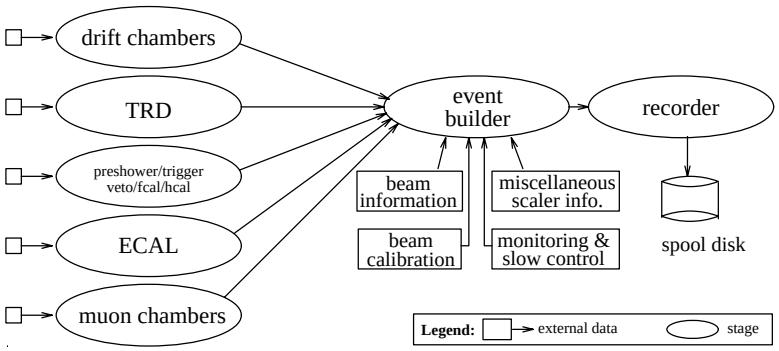

Figure 4.1: Schematic overview of the NOMAD data acquisition system

2. *Filtering:* Neutrino interactions in the target region are pre-selected with two filter algorithms, termed "loose" and "intermediate." These reject events with primary vertices outside the target region, and/or fewer than two tracks within. Especially dense events (with 12 or more hits on average per drift chamber plane) are observed to be problematic to further reconstruction, and are removed.

3. *Drift chamber reconstruction:* Using information obtained from the first pass, a much more thorough reconstruction of drift chamber tracks and vertices is performed.

4. *Phase–1 reconstruction:* After the drift chambers, the basic level reconstruction is performed for the other subdetectors. This includes, for example, the translation of raw data into space coordinates, and the construction of muon chamber track segments and calorimeter clusters.

5. *Phase–2 reconstruction:* This phase combines information from the separate subdetectors for particle identification and to form complete events. Drift chamber tracks are extrapolated to the other subdetectors and associated to calorimeter clusters and muon chamber track segments. Algorithms handling this process are referred to as the "matching engine."

Some of the more important elements of the reconstruction algorithms are detailed below.

4.2.1 Track and Vertex Finding and Fitting

The reconstruction of tracks in the drift chambers consists of four phases [25]:

1. *Triplet Building:* The fundamental units from which tracks are constructed in NOMAD are combinations of single hits in each plane of a given drift chamber. Combinations belonging to the same track are isolated with simple geometric criteria.

2. *Helix Search:* Three or more triplets may then be tested as to whether they belong to the same helix, the most general path of a charged particle in a magnetic field. A helix is uniquely described at each point by six parameters: three spatial coordinates, two angles, and the curvature with the proper sign.

3. *Triplet Collection:* With the helix parameters, additional hits in a road around the helix are collected and assigned to tracks.

4. *Track Fitting:* Track candidates may now be fit; position, curvature, and direction may be estimated by procedures which should be optimal in the statistical sense.

Perturbations of particle trajectories in the drift chambers, due primarily to multiple scattering, make traditional global least–squares fitting procedures highly impractical. A stepwise method known as a Kalman filter is used instead for the calculation of the track parameters. The curvature of the track provides the momentum of the particle.

Once the tracks have been reconstructed in the drift chambers, the vertex algorithm is applied [26]. This algorithm determines the event topology, deciding which tracks belong to which vertex (the *primary*, or initial interaction point, or various secondaries resulting from subsequent interactions and decays) and makes fits to

determine the track parameters at the vertex. These tasks are interdependent and event topology strongly depends on the results of fitting a sample of tracks at a vertex; a poor fit at a given vertex may prescribe the removal of tracks or a fit at another vertex. In events with several tens of tracks, this procedure can become extremely cumbersome, therefore a version of the Kalman filter is used. Due to the overly restrictive settings of various parameters for track–vertex association, additional vertex association is applied at the analysis level (section 6.2).

4.2.2 Calorimeter Energy Measurement and Clustering

Reconstruction algorithms for the electromagnetic calorimeter [27] determine the shape and magnitude of energy deposits in the lead glass blocks. These deposits, or "clusters" consist of contiguous groups of calorimeter cells and originate from both charged particles (track–associated clusters) and neutrals (unassociated or "isolated" clusters).

To convert the signal from a calorimeter block from ADC counts to energy, the ADC counts are multiplied by the ratio of the energy measured by the block in a test beam to the average test beam ADC counts. The average counts are in turn corrected for the differences in conditions between the test beam and the experiment, such as the presence of the magnetic field and degradation effects, as measured with the LED monitoring system.

The clustering algorithm records the position of the first calorimeter cell having an energy deposit greater than a certain threshold (30 MeV by default). Adjacent cells with energy deposits greater than this threshold are added to the seed cell, and the process continues until no other adjacent unused cell is found. The finished cluster centroid is determined with a center of gravity method, and the radius is computed using the spread of the energy distribution.

4.2.3 Data Statistics

Due to technical problems, construction of all NOMAD drift chambers could not be completed before the beginning of the 1995 run. The chambers were therefore installed in stages during the run, beginning with the modules furthest downstream. As a result, data taking in 1995 was divided into 3 distinct periods, during which 4, 8, and finally the full 11 modules of drift chambers were present. For the number of protons–on–target during each period, see section 5.3.3.

This study is based on the official 1995 NOMAD data sets. These include the 4, 8, and 11 module data. Drift chamber reconstruction version v5r9++ (referred to as "PROD4" [25]) has been applied to these samples, and the resulting output passed through phases 1 and 2 of the general reconstruction (version 63) [28]. For practical purposes, this data set has been projected into an "ntuple," a flexible data structure available as part of the CERN-developed HBOOK analysis software package [29]. Referred to as NTUPLE6, it contains all official NOMAD data and Monte Carlo samples available as of this writing. The data statistics are summarized in table 4.1.

Full Data Statistics		
sample	*source*	*NTUPLE6 ev.*
Data	4-module	85406
	8-module	194668
	11-module	217009

Table 4.1: Statistics of the data samples in NTUPLE6, and used in this analysis

Chapter 5

Event Simulation

As in most high energy physics experiments, physical events making up the NOMAD experimental data result from the synthesis of detailed information from many complex subsystems. In order to provide a convenient framework for the essential task of interpreting the data in terms of fundamental theories, a complete computer simulation of the physics processes in NOMAD is performed, using Monte Carlo methods. The output of the simulation program has essentially the same format as the real data, so that it may be passed though the same reconstruction and analysis algorithms, allowing for direct comparisons.

Using Standard Model physics processes as the basic input, the simulation is used to predict the types and rates of events expected to be observed, and the effects of detector acceptance on the real data. With the addition of simulated tau neutrino events, the simulation is used to estimate the efficiency of the detector for selecting signals and for rejecting backgrounds, and to optimize the analyses for these purposes.

In the NOMAD experiment, three steps can be distinguished in the complete simulation process: the simulation of the neutrino beam, the generation of neutrino interactions, and the simulation of the detector response to particles produced in these interactions. The first step is described in section 2.3; a brief description of

the subsequent steps is the focus of this chapter.

5.1 Event Generation

The simulation of the physics process $\nu + N \rightarrow l + X$ (where N is a target nucleon, l is a final-state lepton, and X consists either of the nucleon or its fragments, plus other by–products of the reaction) in the context of the NOMAD experiment is performed with the Nomad Event Generator LIBrary (NEGLIB) [30]. This program library consists of several packages for handling various phases of the simulation, as depicted in figure 5.1. The scope is general enough so that the term "NEGLIB" is often used to refer to the overall event simulation in NOMAD.

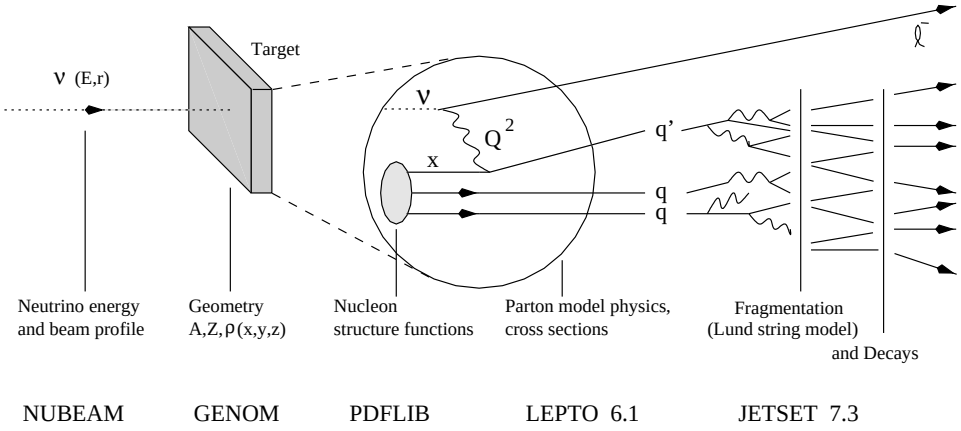

Figure 5.1: Interplay of programs used to simulate interactions in NEGLIB

The types of neutrinos incident on the detector, their energy ranges, and spatial distributions may be specified by the user, or according to the complete beam simulation by way of an interface to the NUBEAM program (section 2.3). The detector geometry information from the response simulation program (see next section) is used to generate the vertex position, as specified by the distribution of material densities along the beam axis.

Deep–inelastic (DIS) neutrino–nucleon scattering processes (in which the incident neutrino is considered to scatter off of a nucleon constituent particle, or parton–the dominant form of scattering at WANF beam energies) are simulated with a modified version of the LEPTO 6.1 program [31]. LEPTO 6.1 is based on the leading–order electroweak cross sections for the underlying parton–level scattering, and includes leading–order QCD corrections. The fragmentation of produced partons into final–state hadrons is performed in LEPTO with the Lund string model, via an interface to the JETSET 7.3 program [32]. Separate programs are provided in NEGLIB for the simulation of the Fermi motion of target nucleons, and for alternate descriptions, if desired, of their parton content. Quasi-elastic (QEL) scattering events (such as $\nu_\mu + \mathrm{n} \rightarrow \mathrm{p} + \mu^-$) and resonance–production (RES) events (such as $\nu_\mu + \mathrm{p} \rightarrow \mathrm{R}^{++} + \mu^-$, followed by $\mathrm{R}^{++} \rightarrow \mathrm{p} + \pi^+$) are simulated with separate packages.

The subsequent decays of τ leptons produced in simulated ν_τ charged current interactions are processed in NEGLIB with the KORALZ package, which includes the TAUOLA program [33].

5.2 Detector Simulation

The propagation of particles produced in neutrino interactions through the NOMAD detector is simulated with the GEant NOMad (GENOM) library [34]. This software is based on the CERN-developed program GEANT [20], a general tool for the complete description of detector geometry and composition, and the passage of particles through matter.

All NOMAD subdetectors are described in the GENOM program. Neutrino events simulated with NEGLIB can be used as input, as can a host of other simulated particles (including cosmic rays), with user–specified energy and spatial distributions. GENOM then records the trajectories of the product particles through the experiment, and simulates the response of the subdetector elements, taking into

account a very comprehensive list of interaction processes. Events output from GENOM can then be passed through the reconstruction and analysis programs as if they were real data.

5.3 NEGLIB Statistics and Event Weights

For the purpose of this analysis, the official 1995 NOMAD Monte Carlo samples are used. They were generated with the GBEAM+ beam simulation, NEGLIB version 5.03, and GENOM version 510. These events were then passed through the same reconstruction chain as the corresponding real data (section 4.2.3), and stored in the NTUPLE6 data structure. The total event statistics from NEGLIB and NTUPLE6 which are used in this analysis are summarized in table 5.1.

The Monte Carlo statistics used represent the largest possible sample of the events available; the events of different types are not in the proportion expected from the actual beam and target. Furthermore, several basic deficiencies in the beam and detector simulation were noticed after the official event samples had been produced. Therefore, a weight is assigned to each Monte Carlo event to compensate for these effects, in order to allow the immediate comparison of Monte Carlo and data distributions. A single routine (specific to this analysis and separate from the official Monte Carlo production), called once with each Monte Carlo event processed in the analysis, is used to compute the weight. To each Monte Carlo event, a global weight W_g is given, and corrections are applied to this weight in accordance with the factors described in this section.

5.3.1 Neutrino Flavors and Interactions

For a given Monte Carlo event, the initial weight is computed according to the type of interaction i (CC or NC), the type of scattering s (DIS, QE, RES) simulated, and

Full Monte Carlo Statistics					
sample	*interaction*	*scattering*	*source*	*NEGLIB ev.*	*NTUPLE6 ev.*
MC	CC	DIS	ν_μ	153889	147680
			$\bar{\nu}_\mu$	30000	29344
			ν_e	26998	24603
			$\bar{\nu}_e$	2604	2355
		QE	ν_μ	10000	9606
			ν_e	1653	1422
		RES	ν_μ	2000	1942
			ν_e	1482	1242
		(coil)	ν_μ	∼40600	17586
		(magnet–C)	ν_μ	∼60000	2286
		(magnet–I)	ν_μ	∼104000	70084
	NC	DIS	ν_μ	113657	99407
			$\bar{\nu}_\mu$	18000	14564
			ν_e	8354	6920
		(coil)	ν_μ	∼45400	16789
		(magnet–C)	ν_μ	∼30000	790
		(magnet–I)	ν_μ	∼57000	11355

Table 5.1: Statistics of Monte Carlo samples in NTUPLE6, and used in this analysis. The difference in the numbers for NEGLIB and NTUPLE6 are due to the application of the density cut and other losses in PROD4.

the neutrino species n (ν_μ, $\bar{\nu}_\mu$, ν_e, $\bar{\nu}_e$) incident on the detector, with the expression:

$$W_{isn} = \frac{W_g P_{isn} I_n}{N_{isn}}. \tag{5.1}$$

Here, W_{isn} is the event weight, the global weight W_g is proportional to the number of events in the entire *data* sample, I_n is the incidence fraction for this neutrino species, and N_{isn} is the number of Monte Carlo events of the given type. P_{isn} is the relative probability that a neutrino of flavor n undergoes scattering s (DIS, QEL, or RES) by way of interaction i (NC or CC).

The starting values for the incidence fraction I_n are extracted from NUBEAM. For a simulated event with a given neutrino species incident on the detector, I_n is simply the ratio of the total number of events in the NUBEAM spectrum for that species to the total number in all spectra. For ν_μ, $\bar{\nu}_\mu$, ν_e, and $\bar{\nu}_e$, the fractions expected are .9516, .0326, .0141, and .0017, respectively. The actual values used for W_g and I_n are obtained by normalizing the predicted muon and electron spectra to the observed data distributions (section 6.4.2). A comparison of the observed fractions with the expectation quoted above is given in section 6.4.3. P_{isn} is calculated from and fixed to the relative CC and NC cross sections, and the quasi-elastic and resonance cross sections, which can be found in the literature (table 5.2).

5.3.2 Kinematic Cutoffs

All deep-inelastic Monte Carlo events used in this analysis were generated with restrictions on certain kinematic variables. The requirements implemented in the Monte Carlo samples at the generation level are:

1. Hadronic energy transfer (ν) > 1.0 GeV
2. Final–state lepton energy > 1.0 GeV
3. Four–momentum transfer (Q^2) $> 0.3(\text{GeV})^2$
4. Hadronic system invariant mass (W^2) $> 1.3(\text{GeV})^2$

interaction	*scattering*	*source*	σ (cm^2)	$E_{mean}(GeV)$
CC	DIS	ν_μ	$0.67 \times 10^{-38}/GeV$	23.6
		$\bar{\nu}_\mu$	$0.34 \times 10^{-38}/GeV$	22.7
		ν_e	$0.67 \times 10^{-38}/GeV$	36.7
		$\bar{\nu}_e$	$0.34 \times 10^{-38}/GeV$	32.2
	QE	ν_μ	0.4×10^{-38}	-
		ν_e	0.4×10^{-38}	-
	RES	ν_μ	0.6×10^{-38}	-
		ν_e	0.6×10^{-38}	-
NC	DIS	ν_μ	$0.223 \times 10^{-38}/GeV$	23.6
		$\bar{\nu}_\mu$	$0.146 \times 10^{-38}/GeV$	22.7
		ν_e	$0.223 \times 10^{-38}/GeV$	36.7

Table 5.2: Cross sections assumed for the calculation of P_{isn}. The mean energies are taken from NUBEAM predictions. Processes not quoted in the table (e.g., NC resonances) have not been simulated, and are therefore not included in the analysis.

The NOMAD data extend to smaller values in these parameters. Instead of removing the data in question with cuts, the weighting function is used to make approximate compensations in the Monte Carlo samples. For example, the weight for all ν_μ and ν_e events with final state lepton energy of 1-2 GeV is scaled by a factor of 2, the weight for events with ν less than 1.5 GeV is scaled up by a factor between 1 and 3, and the weight for events with Q^2 less than 0.5 GeV^2 is scaled up by a factor between 1 and 2.5. The exact choice of the weight for any given event is a detailed procedure which has to account for the correlations between the various cutoff parameters (in order to avoid double–counting), and has to be further adjusted to preserve the scaling behavior (cross section rising linearly with total energy) in the DIS sample.

5.3.3 Drift Chamber Modules Present

All Monte Carlo events in this analysis are simulated with the full target. To compensate for the different number of drift chamber modules present in the detector

over the entire data taking period, the global weight factor for a given event is scaled according to the z-position of the vertex. Specifically, for a Monte Carlo event with a vertex in a given z-range, the weight factor is multiplied by the ratio of protons-on-target available to the modules present in that range to the total number of protons-on-target. These factors are summarized in table 5.3.

Vertex z (cm)	*modules in range*	*p.o.t. available*	*correction factor*
$0 < z < 110$	1-3	3.0×10^{18}	.3488
$110 < z < 256$	4-7	6.0×10^{18}	.6977
$256 < z$	8-11	8.6×10^{18}	1.0

Table 5.3: 4, 8, and 11 module data correction factors

5.3.4 Drift Chamber Inserts and Glue Strips

Vertex distributions in the data indicate that the vertex density in regions ($\simeq 8 \times 8$ cm^2.) of the drift chamber inserts is higher by about a factor of 6 over the rest of the target volume. Similarly, the density in the regions of drift chamber glue strips is higher by a factor of 2.2. Neither feature is simulated in the NEGLIB samples used in this analysis. Therefore, the global weight factors for Monte Carlo events with vertices in regions corresponding to the inserts is scaled by a factor of 6, or 2.2 for the case of the glue strips, as summarized in table 5.4.

5.3.5 Trigger Efficiency

All Monte Carlo events for which the veto simulation recorded any number of hits, or for which the trigger simulation recorded zero hits in either trigger plane, are assigned a weight of zero, yielding the simulation of the geometrical trigger efficiency.

Vertex x (cm)	*Vertex y (cm)*	*correction factor*
-74.0< x <-66.5	-71.0< y <-63.0	6.0
-74.0< x <-66.5	-0.5 < y < 7.5	6.0
-74.0< x <-66.5	70.0 < y < 78.0	6.0
-2.0 < x < 6.0	-71.0< y <-63.0	6.0
-2.0 < x < 6.0	-0.5 < y < 7.5	6.0
-2.0 < x < 6.0	70.0 < y < 78.0	6.0
71.3 < x < 79.3	-71.0< y <-63.0	6.0
71.3 < x < 79.3	-0.5 < y < 7.5	6.0
71.3 < x < 79.3	70.0 < y < 78.0	6.0
-140 < x < 140	-51.3< y <-51.0	2.2
-140 < x < 140	-49.3< y <-49.0	2.2
-140 < x < 140	56.0 < y < 56.3	2.2
-140 < x < 140	59.0 < y < 59.3	2.2

Table 5.4: Correction factors for inserts and glue strips. The positions given are approximate only as they are extracted phenomenologically from the data, and do not necessarily reflect the true geometry.

5.3.6 Coil, C, and I events

The coil ($\sim$ 32 tons), C ($\sim$ 880 tons), and I ($\sim$ 90 tons) samples are normalized to the weight of these detector components relative to the fiducial target (2.7 tons). The weight is further corrected for the relevant radial neutrino flux ratio, and additional factors (of at most a factor 2) which were obtained from the analysis of the 1994 data. The resulting weights fall in the range between 10 and 300 (!).

5.4 Re-weighting for NUBEAM

The GBEAM+ parametrization used at generation level for the simulation of the beam spectrum has several known deficiencies:

- The simulation was historically optimized for, and tuned to, the CHARM II beam configuration (different beam configuration, different detector position). A simple scaling scheme was applied to translate this spectrum to the NOMAD

position.

- The simulation of the beam line was not updated to the actual configuration (e.g., incorrect horn and reflector positions).
- Antineutrino beam settings (opposite polarization of horn and reflector currents) were used instead of neutrino beam settings for the simulation of the antineutrino part of the beam.

Since these simulations were done, NOMAD has invested a lot of work into providing a much more accurate and up to date beam prediction, based on the NUBEAM 4.00 program. To avoid having to regenerate all the Monte Carlo samples, the existing samples are reweighted on an event-to-event basis by comparing the NUBEAM and GBEAM+ flux predictions as a function of neutrino energy and vertex radial position. The MC event weight is corrected by the ratio of these two predictions. The resulting MC spectra are equivalent to having generated them directly with NUBEAM, except for some fluctuations due to the necessarily finite statistics used for the generation of the two-dimensional translation tables. Typical weight corrections are of the order of 0.5–2.0.

5.5 Corrections not Integrated into Weight Function

Finally, a certain number of global differences between data and Monte Carlo have not been integrated into the weight functions. All the numbers given below are rough estimates and have errors of the order of 50% on the relative inefficiency. These include:

1. *Filter efficiency:* All real data events have been passed through a set of filter programs ("loose" + "intermediate"). The main filter inefficiency arises from a density cut on the average number of drift chamber hits per hit plane, which is set to 12. The global efficiency for this filter was estimated from scanning to be 93%. For the Monte Carlo, a similar drift chamber density cut was

implemented in PROD4. The difference of the efficiency of this cut with respect to the data filter is found to be 3% for ν_μ CC events, so an additional factor of .97 should be applied to the Monte Carlo efficiency.

2. *Trigger efficiency:* The difference between the actual and simulated trigger counter hardware efficiency yields a correction factor of 0.98, resulting in a total trigger efficiency of 0.95 for ν_μ CC events.

3. *Tracking and vertexing:* From a comparison of muon tracks matched to TRD tracks, drift chamber tracks, or both, the muon tracking efficiency is about 1% higher in the Monte Carlo than in the data. The vertex finding efficiency using the algorithm described in section 6.2 is estimated to be about 2% more efficient in the Monte Carlo. This yields another factor of 0.97 reduction for the total effeciency for ν_μ CC events.

4. *Muon chamber reconstruction:* The quality of the muon chamber reconstruction yields another factor 0.99 for the relative data/MC efficiency for ν_μ CC events.

5. *Fragmentation:* The jet fragmentation parameters used in the NEGLIB generation relevant for this analysis are known not to reflect the most up-to-date measurements. Some distortions of the hadron multiplicity and momentum spectra with respect to the data are thus to be expected. No correction for this effect is attempted at the present stage of the analysis.

Chapter 6

Muon Neutrino Analysis

Due to their relative abundance and expected low contamination by potential non-standard physics effects, ν_μ CC events are well suited to study the general properties of neutrino interactions. The primary purpose of this chapter is to use these standard events to investigate how well the data are represented by the Monte Carlo simulation. The proper identification of ν_μ CC events is also important since the number of these events produced in the detector enters directly into the calculation of the neutrino mixing parameters in the $\nu_\mu \to \nu_\tau$ oscillation search.

In the first sections of this chapter, a fiducial volume and a less stringent vertex association algorithm are introduced to compensate for some known features of the NEGLIB generation and PROD4 reconstruction. Muon identification is then applied, and some simple data and Monte Carlo distributions are compared (single particle spectra, multiplicity distributions). The normalization and shape obtained for the various data components (beam composition, cross sections) is compared to the NUBEAM plus Standard Model predictions.

Starting from a long–standing observation that significant discrepancies exist between the observed and simulated distributions for the missing-p_T and many other kinematic variables as measured in NOMAD, a set of Monte Carlo adjustments is proposed which significantly reduces these observed differences. These adjustments

include the addition of nuclear effects not yet considered at generation level, and the compensation of smearing and reconstruction effects not yet fully accounted for by the detector simulation. Motivations are given for both the choice of the additions applied, and the relative weight attributed to each of them. Finally, a strategy is proposed for the use of these additions in the context of further analyses.

6.1 Fiducial Volume

The data sample used contains contributions from the main target, as well as backgrounds from interactions in the surrounding materials (coil, C, I, basket, trigger scintillators, etc.), straight through muons leaking through the veto counters, and cosmic ray muons. Main target events are simulated inside a volume of $|x, y| <$ 140 cm, $0 \leq |z| \leq$ 408 cm, with statistics comparable to the data statistics. Low statistics (1-10% of data statistics) samples are also provided for interactions in the coil, magnet–C, and magnet–Is (table 5.1). Simulation of events in the intermediate region (edge of target beyond 140 cm, basket, trigger scintillators, etc.) and simulation of the single muon background is not yet provided.

In order to suppress these backgrounds, at least two tracks are required from the primary vertex (see section 6.2), and a fiducial cut is imposed. Unless quoted otherwise, the reference fiducial volume used for this analysis is the official NOMAD fiducial volume defined by: $|x| <$ 130 cm, $-125 \leq |y| \leq 135$ cm, $0 \leq |z| \leq$ 405 cm, i.e., the reconstructed primary vertex must lie within this volume. In order to reduce the background from upstream interactions and to account for the partially installed target, additional vertex–position requirements of $z > 5$ cm for 11–module data, $z > 110$ cm for 8–module data, and $z > 256$ cm for 4–module data are imposed.

In addition, an event is rejected for being outside of the fiducial volume if any of the following hold:

1. More than 25% of the tracks in the event originate outside a slightly more restricted fiducial volume.

2. More than one track in the event originates at $z < 5$ cm.

3. There are no tracks in the event with momentum greater than 500 MeV.

6.2 Vertex Association

In response to problems with vertex reconstruction in PROD4, an additional vertex–association algorithm is applied to the drift chamber tracks in each event. In this algorithm, a track is considered to be associated to the primary vertex if the vertex associated to the track is within Δz = 40 cm of the primary vertex, and one of the following criteria is met:

1. The track is already associated to the primary vertex by PROD4.

2. The track is associated to a vertex other than the primary, and this second vertex lies within 10 cm in x, y, and z of the primary vertex.

3. The track is forward, has initial point within Δz = 40 cm of the primary vertex, impact parameters within 5 cm in x and 10 cm in y, and more than one track in the event is associated to the primary vertex by PROD4.

4. Only one track in the event is associated to the primary vertex by PROD4, and the angle between that track and the candidate track is greater than 0.45 radians (this removes broken single tracks, muons with delta rays, and other fake 2-track vertices).

For cases in which PROD4 has already identified a primary vertex with at least two tracks, additional forward (backward) tracks starting (ending) within Δz = 40 cm (Δz = 15 cm) of that vertex are considered to be associated if their impact parameters are within 5 cm in x and 10 cm in y.

This algorithm will sometimes be referred to as the "box" vertex algorithm. For the purposes of this analysis, all events are required to have at least two tracks

associated to the primary vertex according to the criteria described, as a necessary condition for the eventual requirement of a final–state muon and hadronic system.

6.3 Muon Identification and Event Classification

For further studies, the data sample (after fiducial cuts) is subdivided into two categories:

1. *1-muon sample:* This sample consists of events containing at least one reconstructed muon, using the loose muon identification criteria defined below. It is overwhelmingly dominated by ν_μ (and $\overline{\nu_\mu}$) CC events, with only a very small background (order 1%) from punch-through and decay hadrons from NC and ν_e interactions.

2. *0-muon sample:* This sample is complementary to the 1-muon sample. It contains all events which have no identified muon, *and* no track in the muon chambers pointing back into the target volume. The latter requirement is added to remove the small fraction of events in which the muon has not been properly reconstructed in the drift chambers, and events with low momentum muons which do emerge from the iron absorber but fail the matching cuts due to large multiple scattering. This sample is dominated by NC interactions from all neutrino flavors, with a rather sizeable contribution from ν_μ CC events in which the muon has ranged out in the iron absorber. Smaller contributions are due to events in which the muon failed the muon chamber geometrical acceptance or track reconstruction criteria, and ν_e CC events.

For the purpose of the inclusive particle distributions discussed later, "muons" are tracks satisfying the muon identification criteria described below (one entry per event), and "hadrons" are all tracks which are not muons (including electrons).

6.3.1 Loose Muon Identification

A primary muon is identified if it satisfies the following muon quality requirements:

1. The muon candidate drift chamber track must be reconstructed, associated (but not necessarily fitted) to the primary vertex (section 6.2), and have its first hit within $\Delta z = 15$ cm of the primary vertex.

2. The muon candidate drift chamber track must be extrapolated successfully at least up to the first station of the muon chambers.

3. The drift chamber track is matched to muon chamber tracks by the matching engine. In each of the two projections, at least one match is required in station 1 *or* station 2. The only matching requirement for loose muon identification is a distance cut of 40 cm in station 1, and 50 cm in station 2. In case of ambiguities, the closest matching drift chamber/muon track pair is chosen.

4. Finally, a momentum cut of 2.5 GeV is applied.

Fig. 6.1 shows the primary muon acceptance vs. momentum, averaged over the full fiducial volume, for ν_μ CC events. The range-out threshold just below 2.5 GeV is clearly visible.

6.4 Data and Monte Carlo Comparison

Applying muon identification as outlined above, samples of 138692 1–muon events and 62636 0–muon events are obtained. For all the plots shown in this section, all the NEGLIB and NUBEAM weights described previously have been applied, and any statistics displayed on the plots pertain to the data.

6.4.1 Vertex and Multiplicity Distributions

Fig. 6.2 shows the vertex distribution for the 1-muon sample, and fig. 6.3 shows the same distribution for the sum of the 1-muon and 0-muon samples. In both

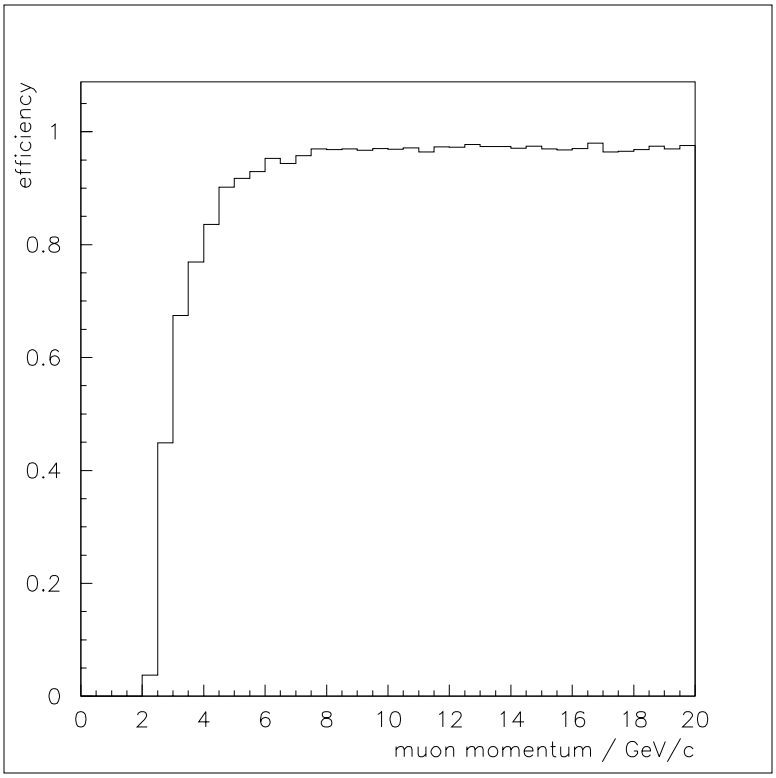

Figure 6.1: Loose muon reconstruction efficiency as a function of muon momentum for ν_μ CC events, including tracking, vertex association, probability to emerge from the iron absorbers, geometrical efficiency, and matching efficiency.

cases, good agreement between data and Monte Carlo is observed. In particular, NUBEAM is able to accurately reproduce the measured radial distribution, and the steps in the z-distribution correctly follow the expected relative fractions from 4, 8, and 11 module data.

Fig. 6.4 shows the multiplicity distribution for charged primary tracks, including the muon, if any, as obtained from the "box" vertex algorithm (section 6.2) for both the 1-muon and 0 muon samples.

The multiplicity distribution for isolated neutral clusters with $E > 100$ MeV in the ECAL is also shown. The 1-muon full MC distributions (dashed line) are

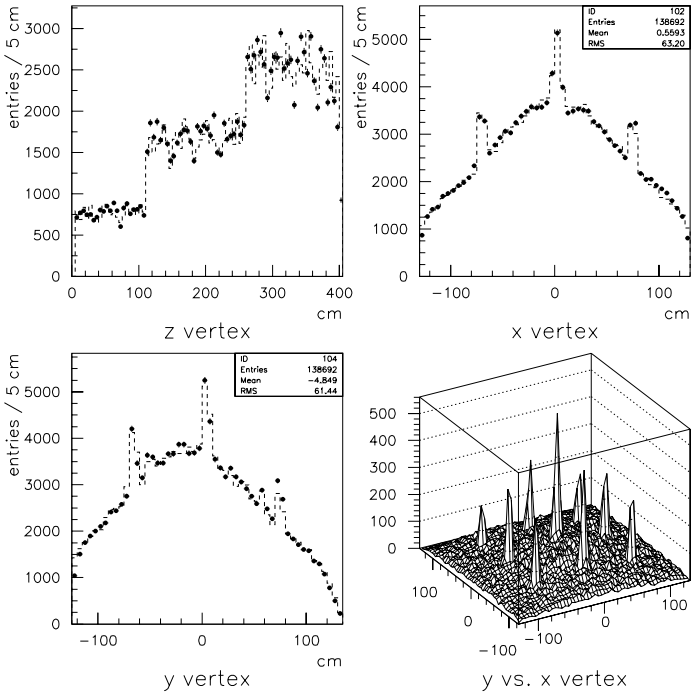

Figure 6.2: Drift chamber vertex distribution for 1-muon events. Shown are the data points, overlaid with the full MC prediction (dashed line).

normalized to the data. Reasonable agreement is observed, considering the fact that the fragmentation parameters in the simulation are known to be suboptimal (section 5.5), and that nuclear reinteractions and differences between the MC and data track reconstruction efficiencies (section 6.6) have not yet been accounted for. The background from NC events (in which a jet track has been misidentified as a muon) is very small (dotted line) and the contribution from C, coil, and I events is negligible (about 0.1%).

The relative normalization of the 0-muon and 1-muon samples is however *fixed* to the relevant theoretical cross section ratios in table 5.2. The reasonable agreement between the 0-muon data (points) and full Monte Carlo (dashed line) therefore

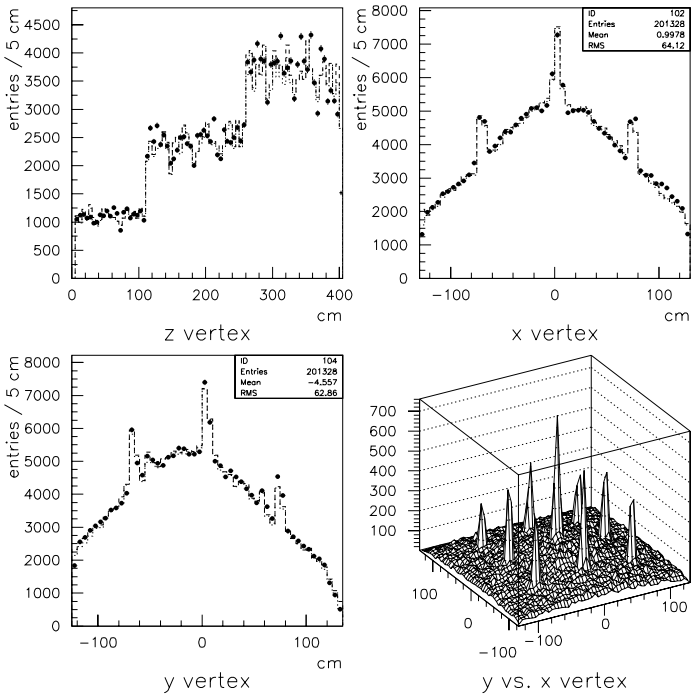

Figure 6.3: Drift chamber vertex distribution for 1-muon + 0-muon events. Shown are the data points, overlaid with the full MC prediction (dashed line) and the contribution from main target events (dotted line).

reflects the fact that the NC/CC ratio is qualitatively understood. Note the significant contamination of this sample by CC events in which the muon has not been identified (dotted line), and the small but non-negligible contribution from C, coil, and I events (dash-dotted line), mostly due to neutral secondary interactions. The disagreement at low multiplicities could be a combination of several effects, including a potential underestimate of the C, coil and I background (errors of factor 2), the non-simulation of background from the basket and target interactions beyond 140 cm, and the non-simulation of NC resonance events.

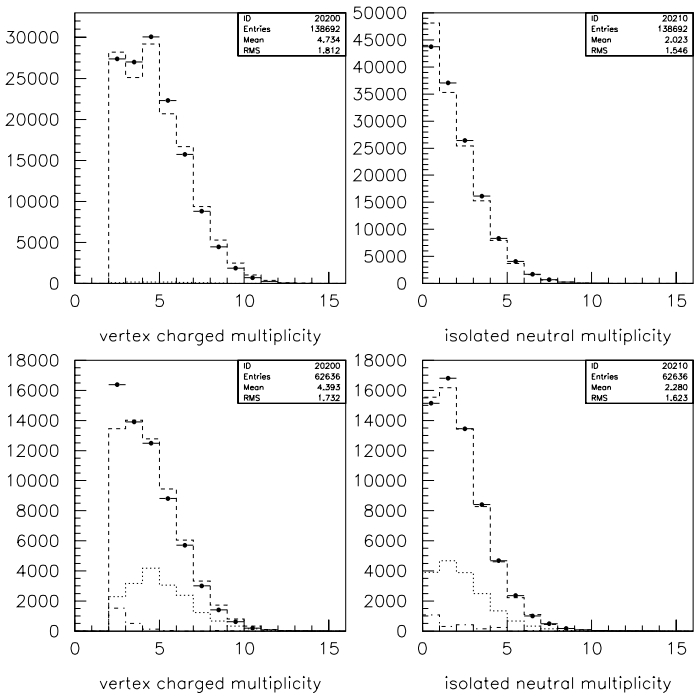

Figure 6.4: Charged and neutral multiplicity distributions for 1-muon (top) and 0-muon events (bottom). For more details, see text.

6.4.2 Inclusive Particle Distributions

Fig. 6.5 shows the inclusive single muon distribution as obtained from the full 1995 1–muon sample. The Monte Carlo curve (dashed line) contains a superposition of all relevant signal and background samples inside the fiducial volume, using the weighting scheme discussed in section 5.3. The negative and positive arms of the spectrum have been separately normalized to the data by varying the respective contributions from ν_μ and $\bar{\nu}_\mu$ with respect to the NUBEAM predictions (since some crossover between μ^- and μ^+ due to matching ambiguities, charm, etc. has to be accounted for, this is an iterative procedure). Note that the typical Monte Carlo

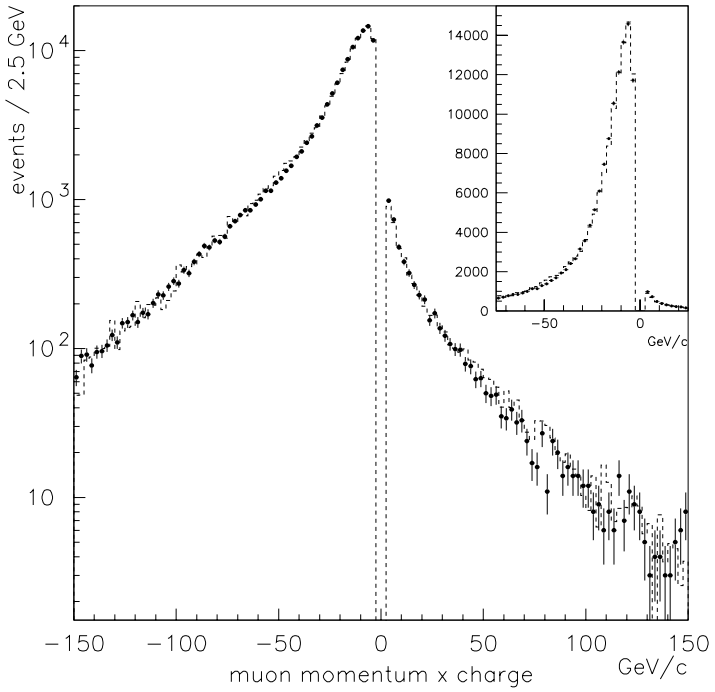

Figure 6.5: Inclusive muon momentum × charge distribution. The data points are overlaid by the Monte Carlo prediction (dashed). The insert shows the same data on a linear scale.

weights are of order 1, so the Monte Carlo curve has about the same statistical errors as the data points.

Fig. 6.6 shows the same distribution extended beyond 150 GeV, after partial bin regrouping to attenuate the statistical errors. It is clear that beyond 200 GeV the distribution is dominated by smearing effects; most of this smearing is reproduced by the standard GEANT simulation (dashed line). However, further improvement is achieved by the application of two additional smearing effects (continuous line):

- Enlargement of the single hit resolution, i.e., the resolution term proportional to momentum, by a factor 1.5. This is an "a priori" correction derived from

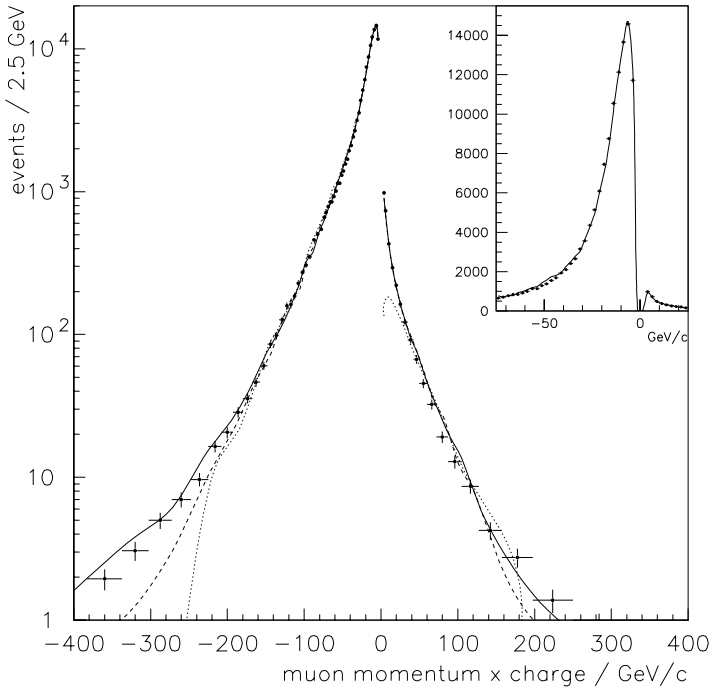

Figure 6.6: Inclusive muon momentum × charge distribution. The data points are overlaid by the full standard Monte Carlo prediction (dashed), the smeared MC prediction (continuous, see text), and the corresponding NEGLIB momentum distribution for ν_μ CC only (dotted). The insert shows the same data on a linear scale.

the respective average resolutions as stored in a drift chamber data base.

- Application of an additional "alignment smearing", i.e., a gaussian smearing of $1/p$ by $\frac{1}{600\ \mathrm{GeV}}$. The order of magnitude of this correction is derived from a study of the average muon momentum in the data as a function of run number and z-position. It has been known for some time that residual alignment errors distort the momentum spectra differently for different run ranges. Un-

fortunately, an attempt to apply these *average* corrections to the *data* did not yield a significant improvement, supporting the findings that the alignment distortions seem to be position dependent, and that these position–dependent variations seem to be of the same order as the average effect. Assuming that the convolution of all these variations can be described by a gaussian error in $1/p$ (which may not be true), the above correction is applied to the *Monte Carlo* sample instead. The value of $\frac{1}{600\ \mathrm{GeV}}$ is phenomenologically found to yield satisfactory Monte Carlo/data agreement.

With this correction, good agreement is observed over 4 orders of magnitude. In particular, the muon charge is reliably measured up to 200 GeV/c. The excess in the full Monte Carlo with respect to the NEGLIB μ^+ distribution at low momenta can be attributed to incorrectly solved matching ambiguities (positive pion matched to track in muon chambers in the full simulation, instead of negative muon), π and K decays, and punch-through background. These backgrounds can be reduced by using tighter matching criteria or isolation cuts (not used here).

Fig. 6.7 shows the inclusive hadron spectrum for the full data sample. Obviously, the data are not well described. Since the further Monte Carlo adjustments discussed in section 6.6 only yield a small improvement, it is suspected that the main source for this disagreement might be the non-optimal parametrization of the fragmentation function (section 5.5).

6.4.3 Comparison with Absolute NUBEAM Predictions

As discussed in the previous section, the actual fractions of ν_μ and $\bar{\nu}_\mu$ CC events observed in the data are obtained from the relative normalization of the inclusive μ^- and μ^+ spectra after background subtraction and efficiency corrections. A similar procedure is applied to e^- and e^+ spectra. The measured fractions are compared to those expected from NUBEAM in table 6.1.

In this context, the re-weighting scheme developed for the ν_μ CC events has

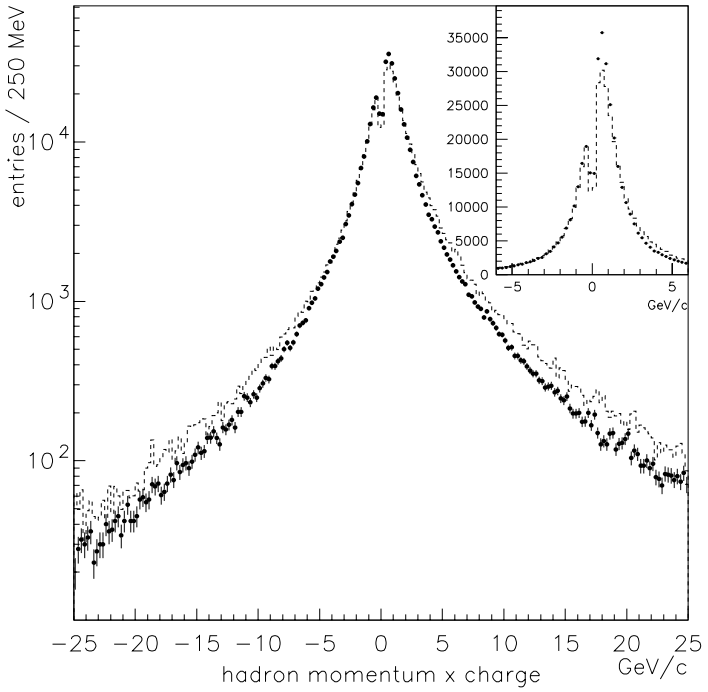

Figure 6.7: Inclusive hadron momentum × charge distribution for 1-muon + 0-muon events. The data points are overlaid by the full standard Monte Carlo prediction (dashed). The insert shows the same data on a linear scale.

been applied to all samples without any further dedicated studies, and the relative efficiencies for the different samples are assumed to be described by the Monte Carlo. With the caveat that no detailed systematic error study has been made which justifies these assumptions, both the $\bar{\nu}_\mu$ and ν_e fractions seem to be overestimated by NUBEAM by about 25%. The $\bar{\nu}_e$ fraction is in agreement within the large statistical error.

A comparison of the observed absolute ν_μ CC event rate with NUBEAM predictions has also been performed (table 6.2). For this study, the quoted MC efficiencies are corrected for the following estimates of MC/data differences (compare also sec-

flux $\times\sigma$ *ratio*	*NUBEAM expected*	*data measured*
ν_μ CC/total CC	0.9516	0.9619
$\bar{\nu}_\mu$ CC/total CC	0.0326	0.0252
ν_e CC/total CC	0.0141	0.0112
$\bar{\nu}_e$ CC/total CC	0.0017	0.0017

Table 6.1: Breakdown of total number of CC interactions within the official fiducial volume into contributions from ν_μ, $\bar{\nu}_\mu$, ν_e, and $\bar{\nu}_e$.

tion 5.5):

- A 2% correction for the muon reconstruction efficiency
- A 2% correction for the vertex efficiency, estimated from "box" vertex studies
- A 2% correction for the hardware trigger efficiency
- A 3% correction for the filter efficiency.

The systematic errors are taken to be equal to the correction in each case. The error on the NUBEAM prediction accounts for a comparison of this prediction with rates actually measured in the muon pits of the beam line.

Comparing the NUBEAM prediction with the actually observed number of data events, a NUBEAM/data ratio of 1.21 ± 0.26 is obtained.

6.5 Event Quality vs. Fiducial Volume

Fake missing-p_T due to reconstruction inefficiencies is one of the major sources of background in the search for $\tau^- \to \mu^- \nu_\tau \bar{\nu}_\mu$ events. These inefficiencies are expected to increase towards the edges of the fiducial volume. In order to assess this problem, several event quality variables are studied as a function of the vertex position:

1. *missing-p_T:* The average magnitude of the missing-p_T in CC events is a measure of the event momentum balance, and hence the reconstruction quality.

cut or correction	*MC eff.*	*data efficiency*	*events* $\times 10^5$	*event type*
loose fiducial + μ id	–	–	1.33014	μ^- events observed
vertex efficiency	0.91	0.89 ± 0.02		
muon id efficiency	0.85	0.83 ± 0.02	1.80 ± .06 (1.69 DIS)	ν_μCC events in fiducial sample $4+8+11$ module z cuts
filter efficiency	0.96	0.93 ± 0.03	1.94 ± .09	ν_μCC events on tape in fiducial
trigger efficiency	0.97	0.95 ± 0.02	2.04 ± .10	generated ν_μCC equivalent in loose fiducial (DIS+QE+RES)
fiducial efficiency	0.711	0.71 ± 0.01	2.87 ± .15	generated ν_μCC equivalent in 11 module target, official fiducial
live time	–	0.85 ± 0.05	3.38 ± .27	NUBEAM equivalent 2.7 tons (8.6×10^{18} pot, 11 mod.)
NUBEAM prediction	–	error: ±20%	4.08 ± .80	NUBEAM $2.6 \times 2.6 \times 4.05$ m^3 2.7 tons, 8.6×10^{18} pot

Table 6.2: Number of events observed/expected for various reference samples

For the purpose of this analysis, missing-p_T is built from primary charged tracks ("box" vertex) and isolated neutral clusters only. This is the same algorithm as the one that will be used in the subsequent $\nu_\mu \to \nu_\tau$ analysis in chapter 7 (see there for the motivation of this choice).

2. *multiplicity:* Non-reconstructed tracks will lower the apparent primary event multiplicity. The average multiplicity is thus a good relative measure of these inefficiencies.

3. *charge balance:* Non-reconstructed tracks will also often yield an unphysical charge balance (sum of charges of all associated tracks) at the primary vertex. Since a (predominantly negative) muon will be required, the lost tracks, if any, will be part of the predominantly positive hadronic system, thus inducing an average negative contribution to the charge balance.

Figure 6.8 shows missing-p_T, multiplicity, and charge balance as a function of each spatial coordinate of the primary vertex. Although there are discrepancies

in the absolute values, the shape of the Monte Carlo curves nicely follows the data, indicating that the simulation of edge effects is qualitatively under control. A set of tight fiducial cuts (dashed lines) is chosen so as to exclude the regions in which the increased levels of missing-p_T correspond to multiplicity degradation and charge imbalance, which can presumably be ascribed to reconstruction effects. The resulting tight fiducial volume used for the rest of this analysis is defined by: $|x| < 115$ cm, $|y| < 105$ cm, 5 cm $< z < 370$ cm. 71% of the ν_μ CC events lie inside this reduced fiducial region.

The observed differences of the absolute values for the missing-p_T and the charge balance in figure 6.8 are one of the motivations for a detailed study of these differences in the next section.

6.6 Study of Reconstruction and Nuclear Effects

Several hypotheses have been investigated in the attempt to understand the differences between the various distributions in the data and Monte Carlo, especially the differences in the missing-p_T distributions. Based on the observations that, for one, the value of the missing-p_T in both the data and Monte Carlo has improved with the progress of various analyses while, second, the differences between the data and Monte Carlo missing-p_T have remained essentially the same, several possible systematic effects have been studied.

These effects include momentum resolution and tracking efficiency in the reconstruction, and nuclear effects in NEGLIB. In the absence of full NEGLIB sets with the additional simulated effects, each effect is simulated in a rudimentary way, with routines at the analysis level which modify parameters in the track lists available from the Monte Carlo sets in NTUPLE6.

It is to be emphasized that this study is by no means offered as the solution to the data–Monte Carlo discrepancies. It is made with the intention to motivate further study of the discrepancies at the event–generation and reconstruction lev-

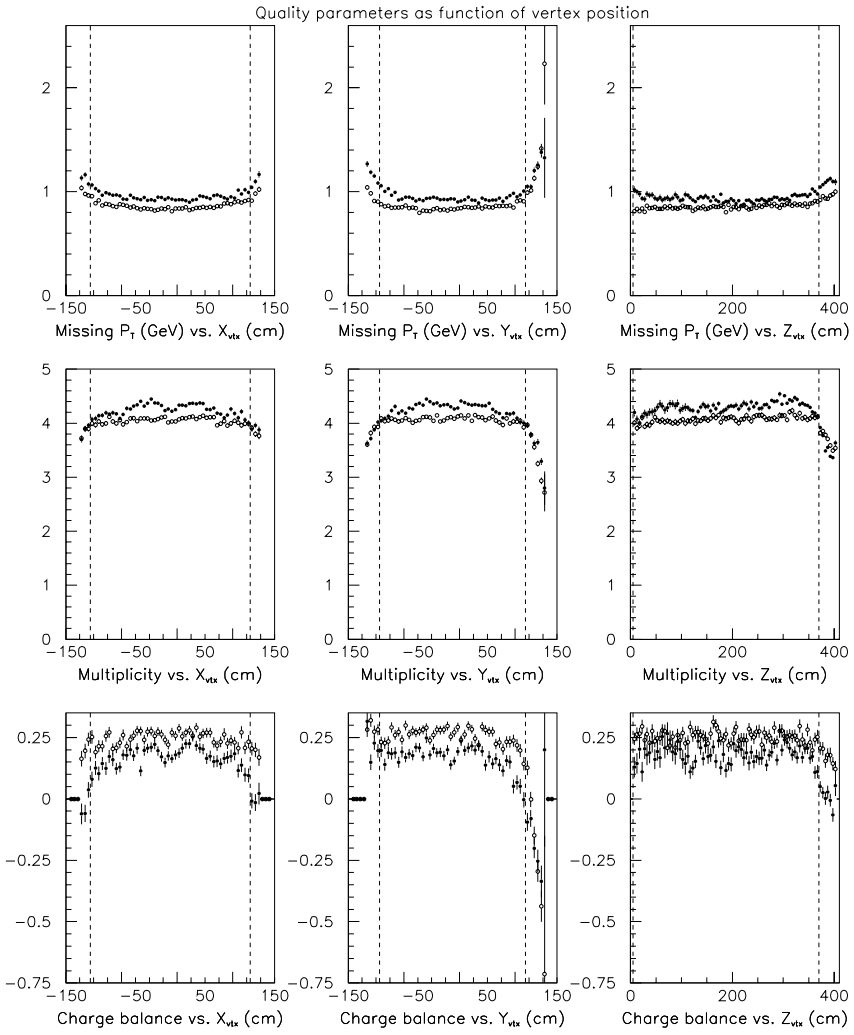

Figure 6.8: Missing-p_T, vertex charged multiplicity, and charge balance as a function of x, y, and z of the vertex. The data (full points) are compared to standard Monte Carlo predictions (open points).

els, and to provide some direction for those studies. It also provides the means to phenomenologically evaluate the systematic error due to these discrepancies on backgrounds and efficiencies for the subsequent $\nu_\mu \rightarrow \nu_\tau$ oscillation studies.

All but one of the adjustments discussed have been fixed using a priori external information, partially obtained from predefined models (e.g., nuclear reinteractions), and partially obtained from the data themselves from reasonably independent distributions (e.g., TRD/drift chamber track match). Although "better" input exists for some of them from subsequent studies, no modifications have been applied in order to minimize potential subjective biases.

6.6.1 Momentum Resolution

One possible contribution to the difference in data and Monte Carlo missing-p_T is a difference in the resolution of the charged track momenta as reconstructed in each set. This effect was already studied in the context of the muon momentum resolution (section 6.4.2). In this part of the analysis, an analogous correction is applied to all tracks.

The Monte Carlo resolution is smeared to that of the data by convoluting the charged particle track momenta and errors with a correction on a track-to-track basis which is equivalent to worsening the single hit resolution by a factor of 1.5. This factor is extracted from the actual track fit errors, available in the drift chamber data base. In addition, a gaussian misalignment smearing of $\frac{1}{600\ GeV}$ is applied, whose value was historically chosen to correspond to the best guess of the systematic alignment variations observed in the data. The motivation for applying a gaussian rather than linear correction is given in section 6.4.2.

The effect of the resolution correction and additional corrections on the missing-p_T is summarized in table 6.3. The smearing results in an average additional 20 MeV of missing-p_T in Monte Carlo events, and makes for the most significant contribution to the observed difference in the widths of the data and Monte Carlo distributions.

6.6.2 Tracking Efficiency

Another possible contribution to the p_T discrepancy is a difference in the in the efficiency to reconstruct tracks between data and NEGLIB events. It has been pointed out that the discrepancy could be explained by this effect alone if the efficiency for the data was lower than for NEGLIB by 20%. The observed effect, based on comparisons between the drift chambers and the TRD, is somewhat smaller. The number of TRD tracks with no match to drift chamber tracks is about 5% higher in the data than in the Monte Carlo. For muons alone, the effect is only about 1%.

The observed deficiency is simulated in this analysis by removing tracks from the Monte Carlo samples. For each charged Monte Carlo track i, a probability for removal is calculated with the formula:

$$P_i = \sum_j \frac{\cot \theta_{ij}}{100}, \tag{6.1}$$

where the summation is over all tracks beginning within $\Delta z = 1$m of the primary vertex and θ_{ij} is the angle between the track i in question and the jth track. A term in the sum is roughly 2% for a track within 50 milliradians and increases to 20% for tracks within 5 milliradians, so that the removal probability is essentially proportional to the track density. Tracks are "removed" by resetting the coordinates of the first and last points to positions well outside the detector volume.

As shown in table 6.3, the efficiency correction adds an average of 10 MeV of missing-p_T to each Monte Carlo event and smears the distribution by roughly the same amount.

6.6.3 Fermi Momentum Tail

Nuclear effects in the target not simulated with the version of NEGLIB used to generate the Monte Carlo sets for this analysis are another possible source of the missing-p_T discrepancy. One such effect is a tail in the Fermi momentum distribution extending beyond the upper limit of the distribution assumed in NEGLIB.

In the NEGLIB event samples used for this analysis, a 225 MeV upper limit to the Fermi momentum distribution is assumed, in accordance with basic nuclear gas models. Theoretical models taking into account effects such as nucleon–nucleon correlations, however, suggest tails in the Fermi distribution extending as high as 4 GeV [35]. The present analysis attempts to implement a distribution based on a more "realistic" correction to these models [36], with a 10% tail extending to 1 GeV. This strategy is in accordance with detailed studies of various parameterizations of the Fermi motion at the event generation level, which have shown that a 4 GeV tail leads to irreducible background not seen in the data.

For each Monte Carlo event in the present analysis, the magnitude of the additional Fermi momentum is calculated with the expression: $P_F = A\sqrt{R_a^2 + R_b^2}$, where, for purely historical reasons, R_a and R_b are two random numbers distributed normally with mean 1. The constant A is set at 0.3, so that the above expression generates the distribution in figure 6.9, for 20000 trials. This additional magnitude is cut at 1 GeV and applied to Monte Carlo events with a 13% frequency, which has the effect of scaling the tail of the simulated distribution above 225 MeV to 10% of the total (figure 6.9). For each Monte Carlo event to which the correction is applied, a random direction for the correction is chosen. The additional momentum is then added to the hadronic jet as a whole (only jet particles are corrected in this analysis; a more thorough treatment would also correct the final state lepton). A boost velocity is then calculated from the initial and corrected jets, which is subsequently used to boost all of the individual jet particles. Corrected tracks with polar angles of more than 60° or momentum less than 40 MeV are removed, in accordance with known reconstruction efficiencies.

The effect of the additional Fermi motion is the least severe of all the additions listed in table 6.3, adding an average of only 5 MeV of missing-p_T to Monte Carlo events.

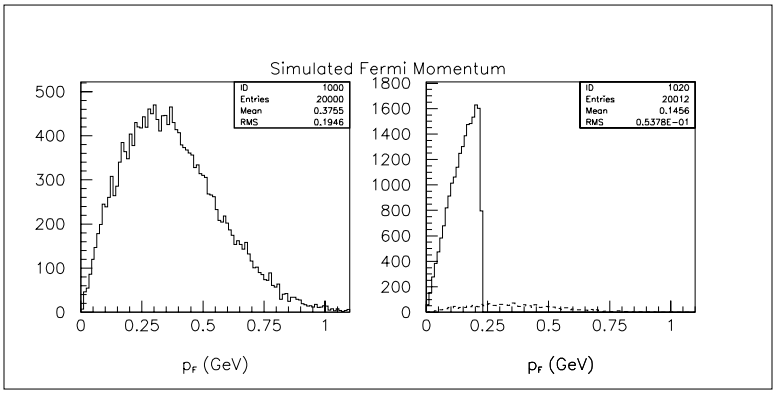

Figure 6.9: Left: Distribution of momenta added in addition to NEGLIB Fermi motion. Right: Same distribution up to .225 GeV (solid curve), with entire distribution scaled to 13% superimposed (dashed line): solid curve plus dashed curve beyond .225 GeV approximates net Fermi distribution used in this analysis.

6.6.4 Nuclear Reinteractions

Another nuclear effect not simulated in the version of NEGLIB used to generate the Monte Carlo sets for this analysis is the reinteraction of hadronic jet particles inside the target nucleus. Additional missing-p_T would be expected due to "hard" energy and momentum transfer to the struck nucleons in the predominantly (65%) carbon target.

Reinteraction effects are currently still a matter of discussion in NOMAD due to the problem of hadronic formation length. If the process of the hadronization of the struck quark occurs over distances long enough such that final state jet particles are formed outside the nucleus, reinteraction effects are not expected by some models. Using such a model with an average formation length of about 1.8 fm, which is currently being implemented in NEGLIB, fewer than 5% of jet particles undergo reinteraction. Reinteractions at this level, however, still produce a visible tail on the missing-p_T distribution.

Other models introduce a finite cross section for the interaction of the quark–gluon string before the hadrons are formed, therefore causing reinteraction effects up to the highest momenta. A recent reanalysis of BEBC data seems to favor such "constituent" models [37].

In the present analysis, nuclear reinteractions are simulated with routines based on the NUCRIN package [38], also used in previous studies. The reinteraction model used applies only to the lowest energy ($p < 5$ GeV) final–state hadrons. There is however no treatment of the formation length; the jet is assumed to be formed completely at the vertex, and the remaining distance to the nuclear boundary is used for the calculation of the reinteraction probabilities. Additional product particles, if any, are added to the NTUPLE6 track list, and corrected tracks with polar angles of more than 60° or momentum less than 40 MeV are removed.

As shown in table 6.3, nuclear reinteractions represent the largest addition to the missing-p_T. The absence of the formation length probably leads to an overestimation of the effect at intermediate momenta, while the momentum cutoff leads to an underestimation at high momenta if the constituent interaction models are correct. Interactions are observed to occur with a frequency on the order of 10%, or about a factor of two higher than the results from a preliminary study which implemented reinteractions at the event–generation level.

6.6.5 Additional Energy Transfer to the Nucleus

In addition to "hard" reinteractions, a "soft" contribution to such a transfer should be expected due to the nuclear binding forces. This is in naive analogy to the energy transfer to the remaining diquark of a nucleon in the spectator model from the subsequent fragmentation.

A detailed treatment of this additional energy transfer would consider such effects as nuclear excitations and breakup, and the proper direction of the restoring force on the jet in light of a composite model of the nucleus. As a zeroth order approximation, this analysis assumes a soft energy transfer of the order of a few

to a few tens of MeV with 100% probability. Applying momentum conservation to the jet–nucleus (carbon) collision, a boost velocity is calculated from the momenta of the initial and final jets, and all jet particles are subsequently boosted in the opposite direction of the original jet. The amount of energy transfer is somewhat arbitrarily calculated with the formula: $E_t = kR\nu + E_b$. Here, R is a random number distributed uniformly on (0,1), ν is the jet energy, and E_b is the minimum energy transfer needed to compensate the nuclear binding forces, estimated at 2 MeV. In order to choose a reasonable scale for this rather ad hoc effect, the constant k is adjusted so as to make the transverse momentum distribution of the hadronic jet agree with the data distribution (figure 6.10), yielding an average kinetic energy transfer of 35 MeV. As such, the energy transfer is the only parameter actually tuned in all of the analysis–level additions to the Monte Carlo.

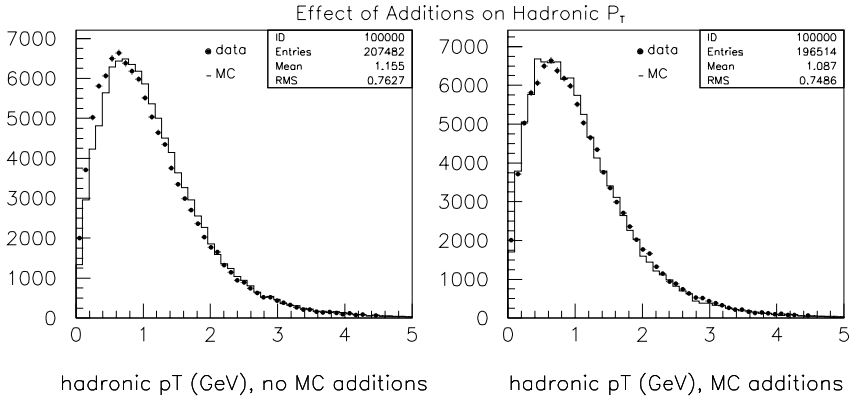

Figure 6.10: Hadronic p_T distributions (left) before Monte Carlo additions and (right) after.

As expected, the principal effect of this naive model of energy transfer, which boosts particles consistently in the direction opposite to the jet, is to shift the missing-p_T distribution (table 6.3). The relatively large effect is due to the large

mass of the nucleus, which translates a relatively small kinetic energy into a sizeable effect when translated into momentum.

As a final word of caution, it should be added that the effect attributed to the kinetic energy transfer could also effectively contain other components which would yield a systematic shift of the hadron p_T distribution, such as an underestimate of the loss of neutral particles. However, its usefulness as a phenomenological compensation of Monte/Carlo data differences is not affected by this ambiguity.

	missing-p_T	
Addition	*mean (MeV)*	*rms(MeV)*
(Uncorrected MC missing-p_T)	739	633
momentum resolution	+ 20	+ 29
reconstruction efficiency	+ 10	+ 9
Fermi momentum tail (1 GeV)	+ 5	+ 0
nuclear reinteractions	+ 61	+ 11
E_k transfer to nucleus	+ 54	+ 3
(Corrected MC missing-p_T)	889	685
(Missing-p_T in *data*)	890	691

Table 6.3: Effect of additions on missing-p_T

6.6.6 Summary and Effect on Kinematic Distributions

The net effect of all of the additions on the missing-p_T is summarized in table 6.3 and in figures 6.11–6.12. Their effect on other kinematic distributions is shown in figures 6.13–6.16 (definitions of these variables are provided throughout chapter 7). In these plots, Monte Carlo distributions are renormalized to the data, and any statistics displayed on the plots pertain to the Monte Carlo. Improvement is evident in all distributions with the exception of ϕ_{mh}, the angle between the missing-p_T and the jet p_T. As emphasized above, only one parameter was explicitly tuned in the set, so that very little bias is expected in the corrected Monte Carlo samples. These results are offered as additional motivation for the ongoing studies of the detailed

treatment of each effect in official NEGLIB productions subsequent to this analysis.

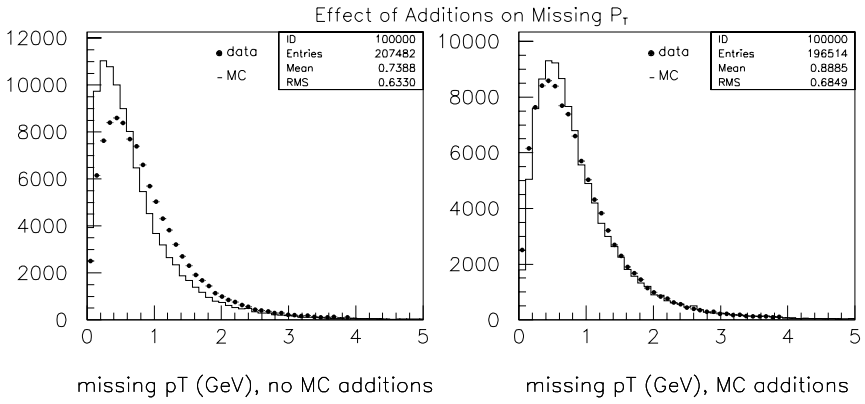

Figure 6.11: Missing-p_T distributions (left) before Monte Carlo additions and (right) after.

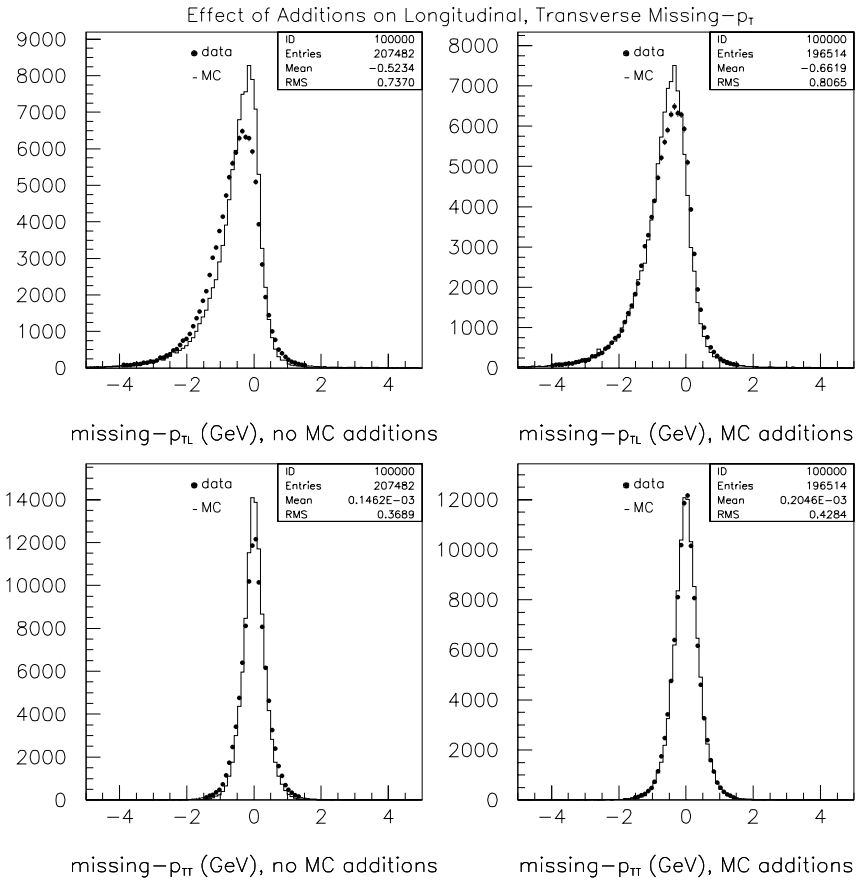

Figure 6.12: Longitudinal (to muon p_T) and transverse missing-p_T distributions (left) before Monte Carlo additions and (right) after.

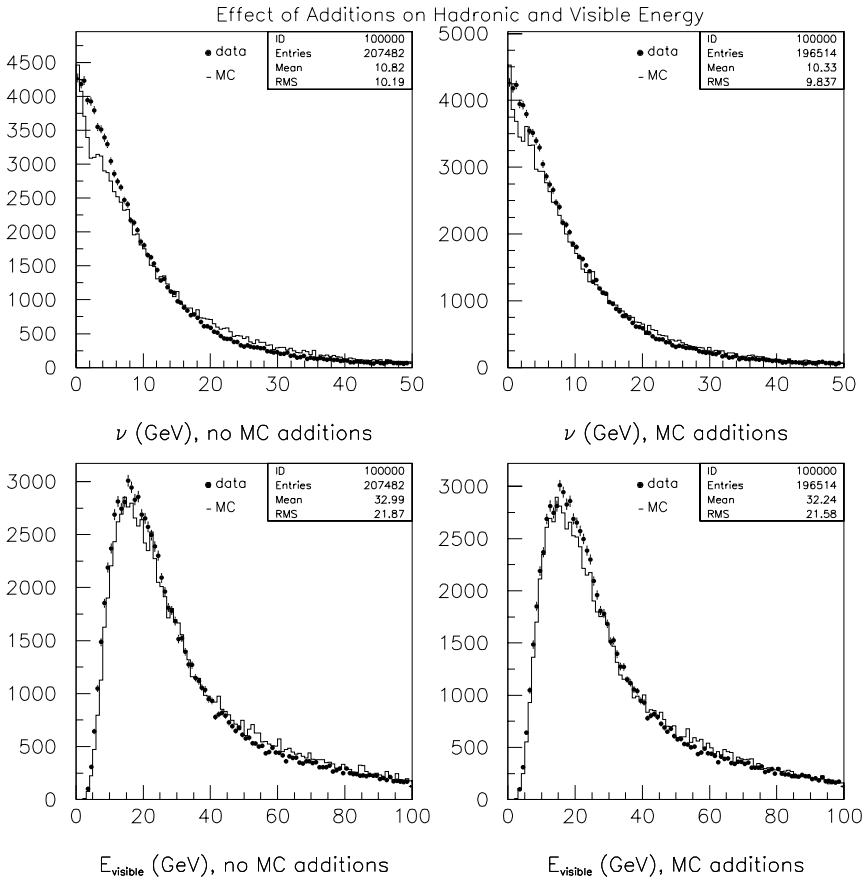

Figure 6.13: Hadronic and visible energy distributions (left) before Monte Carlo additions and (right) after.

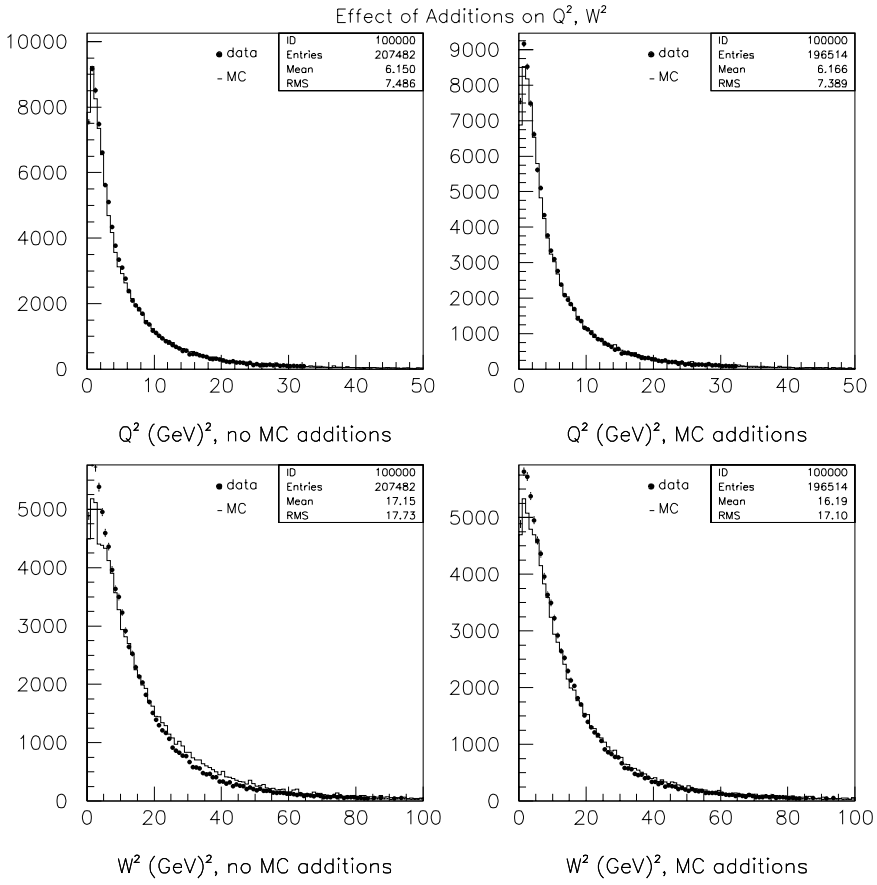

Figure 6.14: Q^2 and W^2 distributions (left) before Monte Carlo additions and (right) after.

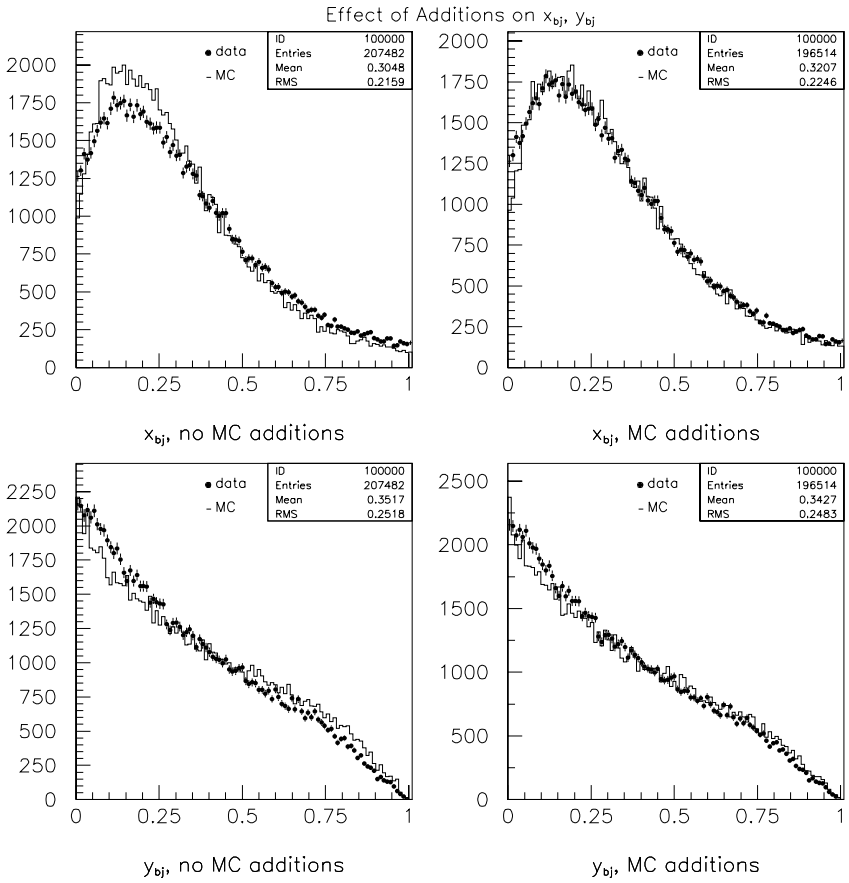

Figure 6.15: X_{BJ} and Y_{BJ} distributions (left) before Monte Carlo additions and (right) after.

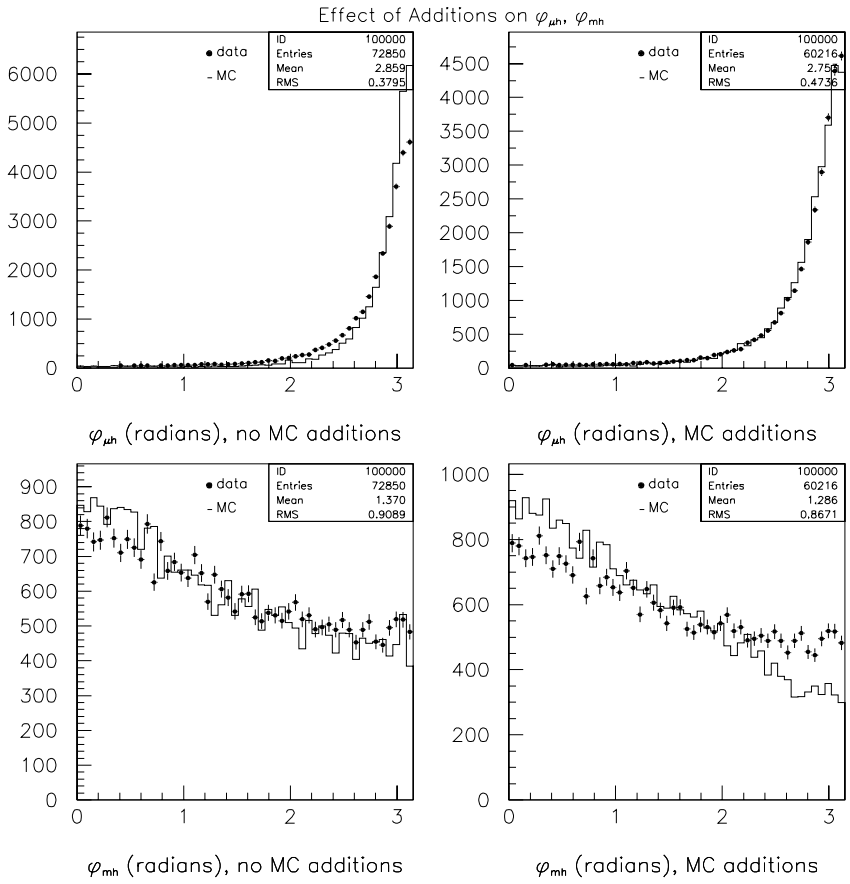

Figure 6.16: $\phi_{\mu h}$ and ϕ_{mh} distributions (left) before Monte Carlo additions and (right) after.

The much better phenomenological agreement with the data for many of the resulting Monte Carlo distributions, in particular those related to the missing-p_T, should yield a more reliable estimate of efficiencies and backgrounds in the $\nu_\mu \to \nu_\tau$ oscillation searches, and the differences before and after additions can yield some idea of the size of the systematic error.

6.6.7 Potential Bias For $\nu_\mu \to \nu_\tau$ Analyses?

The tuning of the "soft" nuclear interaction (section 6.6.5) to obtain agreement in the hadronic-p_T distribution potentially introduces an explicit bias in subsequent $\nu_\mu \to \nu_\tau$ searches. To check for such a bias, the complete event selection (with all weighting) is repeated. The kinematic region in which the $\nu_\mu \to \nu_\tau$ signal is expected is then removed, and effect of the Monte Carlo additions on the hadronic-p_T is re-investigated.

The $\nu_\mu \to \nu_\tau$ signal region is removed by requiring all events to have a ratio $p_{Trat} = p_T^\mu / min(p_{T,}^{miss} p_T^{had})$ of 1.0 or greater, which is equivalent to making a loose selection in the $\phi_{\mu h} - \phi_{mh}$ plane (the function of these variables is explained in chapter 7). All input parameters to the Monte Carlo additions are left unchanged. The effect of the additions on the mean of the resulting hadronic-p_T is summarized in table 6.4.

As shown in the table, the Monte Carlo additions correct the mean hadronic-p_T of the signal–depleted Monte Carlo distribution to that of the data. This result, equivalent to that observed in the full sample with the same additions, supports the conclusion that the tuning of this part of the Monte Carlo additions does not explicitly bias subsequent $\nu_\mu \to \nu_\tau$ searches.

Hadronic-p_T with $\nu_\mu \to \nu_\tau$ Signal Region Depleted		
	Hadronic-p_T	
sample	*mean (MeV)*	*rms (MeV)*
MC, no additions	1173	766
MC, with additions	1095	759
data	1095	747

Table 6.4: Effect of Monte Carlo additions on the hadronic p_T distribution for event sample with $\nu_\mu \to \nu_\tau$ signal region depleted.

6.7 Conclusions

After some basic corrections for cutoffs in the NEGLIB generation, incomplete material description, and NUBEAM re-weighting (chapter 5), good agreement is observed between the measured and expected vertex distributions, and the inclusive muon distributions. The observed absolute and relative event rates are in reasonable agreement with predictions.

The investigation of distributions involving hadrons and/or the hadronic jet shows that the Monte Carlo simulation of the hadronic part of the event is most likely incomplete, with possible contributions from all levels including event generation (e.g., nuclear effects), simulation (e.g., hit smearing) and reconstruction (e.g., tracking efficiency). At the present time, it is impossible to asses the "correct" contribution for each of these effects, although ongoing improvements at all three levels should shed some light on these issues soon. Here, a rough but largely physics motivated set of corrections is proposed, which phenomenologically yields an improved description of many kinematic variables, the most important of which is the missing-p_T.

There is little evidence that the tuning of the additional simulated effects introduces an explicit bias in potential $\nu_\mu \to \nu_\tau$ searches. If this or a similar set of additions is ultimately to be used in an oscillation search, however, it may be necessary to sacrifice the $\tau^- \to \mu^- \nu_\tau \bar{\nu}_\mu$ channel out of concern for such bias. The additions may be confidently applied, however, to a different event sample, most notably the starting sample of ν_e CC events used for the more sensitive search based on the channel $\tau^- \to \mathrm{e}^- \nu_\tau \bar{\nu}_e$. In addition, the corrections should prove useful to the study of systematic effects on efficiency and background calculations for the ongoing $\nu_\mu \to \nu_\tau$ analyses. These studies should be a useful complement to similar studies using real data in which an identified muon is replaced by a neutrino, an electron, or a τ. Eventually, all the considered effects (and more) should be understood and implemented within the standard simulation and reconstruction chain.

Chapter 7

Search for the Oscillation

$\nu_\mu \rightarrow \nu_\tau$

Since its earliest conception, the NOMAD experiment has been designed to set a limit on the (ν_μ, ν_τ) mixing parameters with at least an order of magnitude improvement over the current best limit. In the case of large Δm^2, this corresponds to a mixing angle of $\sin^2 2\theta \leq 3.0 \times 10^{-4}$, at the 90% confidence level. This result is expected from the combined oscillation searches using most of the τ decay modes with branching ratios on the order of 10%. In particular, it was calculated that a search based on the decay mode $\tau^- \rightarrow \mu^- \nu_\tau \bar{\nu}_\mu$ would alone yield a limit (large Δm^2) of $\sin^2 2\theta \leq 1.7 \times 10^{-3}$ [39].

This chapter describes an oscillation search based on the $\tau^- \rightarrow \mu^- \nu_\tau \bar{\nu}_\mu$ decay channel. At present, whether this analysis will be able to attain the anticipated sensitivities, or eventually contribute to the combined result, is not clear. This is primarily due to the difficulties in understanding the high ν_μ CC background for this search.

This analysis can be regarded as an extension of the ν_μ analysis (chapter 6), to study the same systematic effects on the data and Monte Carlo distributions in the context of an oscillation search. The search is carried out using Monte Carlo sets

with and without the additions developed in section 6.6, from which the systematic error on the $\tau^- \to \mu^- \nu_\tau \bar{\nu}_\mu$ selection efficiency is estimated. A preliminary limit for the neutrino mixing parameters is calculated in chapter 8.

7.1 Data and Monte Carlo Samples

7.1.1 Initial Statistics

The starting sample for this analysis is the same as for the ν_μ analysis in chapter 6 (tables 5.1 and 4.1). In addition, a ν_τ Monte Carlo sample is used, originally containing 6000 NEGLIB ν_τ CC events, in which the final-state τ decays via $\tau^- \to \mu^- \nu_\tau \bar{\nu}_\mu$. After the density cut and PROD4 losses, 5717 ν_τ events remain in NTUPLE6.

For the purpose of calculating the efficiency of the $\tau^- \to \mu^- \nu_\tau \bar{\nu}_\mu$ event search (section 7.2), a starting sample of Monte Carlo events within a loose fiducial volume and minimal pre-selection cuts is selected. This sample is chosen to be the number of Monte Carlo events equivalent to the number of data events on tape (i.e., the number corrected for trigger efficiency, but before the filter cuts) with primary vertex in the same fiducial volume defined for the ν_μ study, namely: $|x| < 130$ cm, $-125 \leq |y| \leq 135$ cm, $0 \leq |z| \leq 405$ cm (section 6.1) with additional cuts in z to account for the incomplete target (section 5.3.3). The statistics are summarized in table 7.1.

MC Events in Official Fiducial Volume			
	MC CC	*MC NC*	*MC* $\tau^- \to \mu^- \nu_\tau \bar{\nu}_\mu$
# events	184484	50234	1820

Table 7.1: Statistics of MC event sample in the fiducial volume used for $\tau^- \to \mu^- \nu_\tau \bar{\nu}_\mu$ event selection efficiency calculations, after re-weighting as described in section 7.1.2

7.1.2 Monte Carlo Weights

In addition to the re-weighting applied to Monte Carlo events in the ν_μ study (sections 5.3 and 5.4), re-weighting is used in the NEGLIB ν_τ event samples to insure that the entire set of these events is internally consistent. An arbitrary global weight factor, equal to about 10% of the expected number of CC events, is assigned to each ν_τ event. From this point, adjustments are made for two effects:

- *Tau branching ratio:* For each simulated ν_τ event, the weighting routine identifies the product particles from the τ decay. The weight is then assigned according to the expression:

$$W_i = \frac{W_g, \ _i}{N_i}, \tag{7.1}$$

  where W_g is the global weight, and W_i, , $_i$, and N_i are the event weight, branching ratio, and number of simulated events in the sample for the τ decay channel i in question. (This weight is only relevant if MC samples from different τ decay channels are combined, which is not the case for this analysis.)

- *Tau mass effect:* In order to account for the mass threshold suppression of τ production, the weight for each τ event is scaled by a factor:

$$\left(1 - \frac{m_\tau^2}{2x_{bj}m_n E_\nu}\right)^2, \tag{7.2}$$

  where m_τ is the τ mass, x_{bj} is the Bjorken scaling parameter, m_n is the nucleon mass, and E_ν is the energy of the incident neutrino. (As of this writing, it is not exactly clear how to correct for the only partial treatment of the τ mass in the NEGLIB production. The additional weight in expression 7.2 represents a current best guess as to the correction needed, similar to the treatment used in other preliminary NOMAD analyses. Since this additional weighting can substantially change the final $\tau^- \to \mu^- \nu_\tau \bar{\nu}_\mu$ event selection efficiency, the final results are quoted both with and without this weighting. Unless explicitly stated otherwise, the mass re-weighting has been applied.)

7.1.3 Vertex Association and Fiducial Volume

As in the ν_μ analysis, all events considered for the $\nu_\mu \to \nu_\tau$ search are required to have at least two tracks associated to the primary vertex, according to the vertex algorithm described in section 6.2. Similarly, fiducial cuts in the target are chosen so as to exclude edge regions in which increased levels of missing-p_T correspond to regions of multiplicity degradation and charge imbalance, and can presumably be ascribed to reconstruction inefficiencies (section 6.5). The resulting volume is defined by: $|x| < 115$ cm, $|y| < 105$ cm, 5 cm $< z < 370$ cm. The effects of the multiplicity and fiducial cuts are summarized in table 7.2.

Multiplicity and Fiducial Cuts				
	data	*MC CC*	*MC NC*	*MC* $\tau^- \to \mu^- \nu_\tau \bar{\nu}_\mu$
# events	165442	131525	33932	1261
efficiency (%)	-	71	68	69

Table 7.2: Statistics of event sample after multiplicity and tight fiducial cuts

7.1.4 Muon Reconstruction Criteria

Loose Muon Reconstruction Cuts

All events in the samples considered must pass the "loose" requirements related to the reconstruction of the final–state muon, as described in section 6.3.1. The effect of these cuts is summarized in table 7.3. In the table, the Monte Carlo samples are divided according to interaction type (CC and NC). This allows the direct comparison of the efficiency of the cut in the Monte Carlo Samples to the efficiency in the data sample (μ^- and μ^+ respectively) for which they are expected to constitute the principal contribution. In addition, separate statistics are shown for the Monte Carlo sets both with and without the additions described in section 6.6. This arrangement is intended only as a guideline; the CC Monte Carlo sample contains a 2-3% $\bar{\nu}_\mu$ contribution, and the NC sample also contains both μ^+ and μ^-

final states, in about equal proportion. The appropriate linear combinations of the samples should be made for a full comparison of data and Monte Carlo statistics. Due to the relatively small sizes of the μ^+ and NC samples, the full comparison is closely approximated by the μ^- data and CC Monte Carlo statistics. Note that the loose cuts eliminate most of the NC background events.

Loose Muon Reconstruction Cuts								
	data	*MC CC*		*data*	*MC NC*		*MC* $\tau^- \to \mu^-\nu_\tau\bar{\nu}_\mu$	
	μ^-	*no add.*	*add.*	μ^+	*no add.*	*add.*	*no add.*	*add.*
# events	95212	106460	99071	3628	780	735	927	878
efficiency (%)	60	81	-	-	2.3	-	74	-

Table 7.3: Statistics of event sample after loose quality and muon identification requirements. Data efficiency is for combined μ^- and μ^+ samples. Monte Carlo additions ("*add.*" columns), listed in section 6.6, are applied after these cuts.

Tight Muon Reconstruction Cuts

Up to this point in the analysis, all of the cuts used are exactly the same as those used in the ν_μ CC study (chapter 6). For the purpose of the $\nu_\mu \to \nu_\tau$ search, additional muon reconstruction cuts are applied, in order to insure that the event candidate selection proceeds on a set of well–reconstructed events originating from neutrino interactions. These are the first requirements specific to the $\tau^- \to \mu^-\nu_\tau\bar{\nu}_\mu$ event search, and include:

1. *Muon Identification Consistency:* To reduce background from incorrectly solved matching ambiguities, the muon identification algorithm in the matching engine and that from a previously–used version of the phase–2 reconstruction must agree on which track is the muon in each event. Dimuon candidates are excluded.

2. *Matching–χ^2:* The average χ^2 of the match between the candidate track for the muon in the drift chambers and the track in the muon chambers (in both stations, if relevant) must be less than 3.

3. *Muon momentum:* $|\vec{p}_\mu| > 3.0$ GeV. The momentum cut is tightened with respect to the $|\vec{p}_\mu| > 2.5$ GeV requirement in order to reduce background from hadron decay and punch-through. A small additional loss is introduced in the Monte Carlo if the muon track is removed by the additional Monte Carlo corrections (tracking efficiency correction), where applicable.

The effect of these cuts, along with the event quality cuts (section 7.1.6), is summarized in table 7.4.

7.1.5 Basic Event Kinematics

As discussed in chapter 6, the resulting data sample is well described by the Monte Carlo samples with the additional simulated effects. At this point, the kinematic parameters used to further distinguish between various types of events are calculated. The calculation of the parameters most crucial to the selection of ν_τ-event candidates, and/or to the definition of further cuts, is described below.

Hadronic Jet

The total hadronic vector $(\vec{p}_{jet}, E_{jet})$ is composed from all tracks associated to the primary vertex (section 7.1.3) and isolated neutral clusters in the electromagnetic calorimeter. Hanging tracks and overlapping calorimeter clusters are not included since, if misidentified, they tend to introduce missing-p_T in the direction of the final–state lepton through double–counting, and therefore more background to the $\nu_\mu \to \nu_\tau$ searches via the leptonic channels.

Pairs of oppositely–charged tracks originating from the decay of neutral primary tracks, commonly called "V0s," are not included in the definition of the hadronic

momentum. This avoids large discrepancies observed between data and Monte Carlo V0 reconstruction efficiencies.

In order to better estimate E_{jet}, each charged vertex–associated track is assigned the mass of the pion, with the exception of one positively–charged track (if any) which is assigned the proton mass. The isolated neutral clusters are assumed to originate from photons. This definition is chosen to be consistent with the method yielding a reasonable estimate of W^2 as calculated from the hadronic system alone (section 7.2.1).

Related Quantities

With the hadronic vector as defined above, the following quantities are calculated:

1. *Missing-p_T (p_T^{miss}):* p_T^{miss} is composed from (and opposite to) the first two components of the muon and hadronic jet 3–momenta in the beam frame, and therefore contains only primary vertex–associated charged tracks, and isolated neutral clusters in the electromagnetic calorimeter.

2. *Missing-p_T Error (σ_{P_T}):* The error on p_T^{miss} is calculated with the expression:

$$\sigma_{P_T} = \frac{1}{p_T^{miss}} \sqrt{p_x^2 \sigma_{p_x}^2 + p_y^2 \sigma_{p_y}^2}, \tag{7.3}$$

   where p_x and p_y are composed from the muon and hadronic jet momenta. The errors on the component momenta are estimated by multiplying the total momentum errors (extracted from the reconstruction) by the ratio of the component to the total momentum, and adding them in quadrature.

3. *Hadronic Energy Transfer (ν):* With the total jet energy as calculated above, ν is formed simply by subtracting the mass of the struck nucleon: $\nu = E_{jet} - m_N$.

4. *Visible Energy (E_{vis}):* The visible, or total reconstructed energy of the incident neutrino, is taken simply by forming the sum $E_\mu + \nu$.

7.1.6 Event Quality Cuts

The sensitivity of the $\tau^- \to \mu^- \nu_\tau \bar{\nu}_\mu$ event selection to problems in the reconstruction motivates the series of quality cuts described below. The effect of each cut is illustrated with the corresponding distributions, which are organized in a manner similar to that of the tables: ν_μ CC distributions are displayed below μ^- data distributions, and ν_μ NC below μ^+. In addition, distributions comparing the entire data and Monte Carlo (without $\tau^- \to \mu^- \nu_\tau \bar{\nu}_\mu$) sets are provided for each cut. All plots display the Monte Carlo sets with additions, and any statistics displayed on the plots pertain to the Monte Carlo distributions. The event quality cuts include:

1. *Event Topology:* At least one primary hadron track must survive the Monte Carlo corrections, if applicable, in order to ensure calculability of the kinematic variables used in subsequent cuts.

2. *Multiplicity Limit:* The number of vertex associated tracks (according to the criteria described in section 7.1.3) per event is limited to 8 (figure 7.1). This eliminates events in which the reconstruction is overwhelmed by the activity in the drift chambers (figure 7.2), and attenuates the differences between data and Monte Carlo in response to the hit density cut.

3. *Vertex Association Ratio:* More than half of the drift chamber tracks must be vertex–associated (figure 7.3). This requirement eliminates events in which additional p_T due to charged activity is missed due to poor reconstruction in the region of the vertex, and events with significant secondary interactions. The event in figure 7.4, for example, has only two vertex–associated tracks; the additional stub at the vertex is not associated (fails y–distance cut).

4. *Charge Balance:* $\sum_i q_i = 0$ or 1, where i runs over all vertex-associated tracks in the event (figure 7.5). While consistent with basic charge conservation, this cut is designed to eliminate events with track reconstruction problems. Examples include the event in figure 7.6, which has a charge balance of 2.

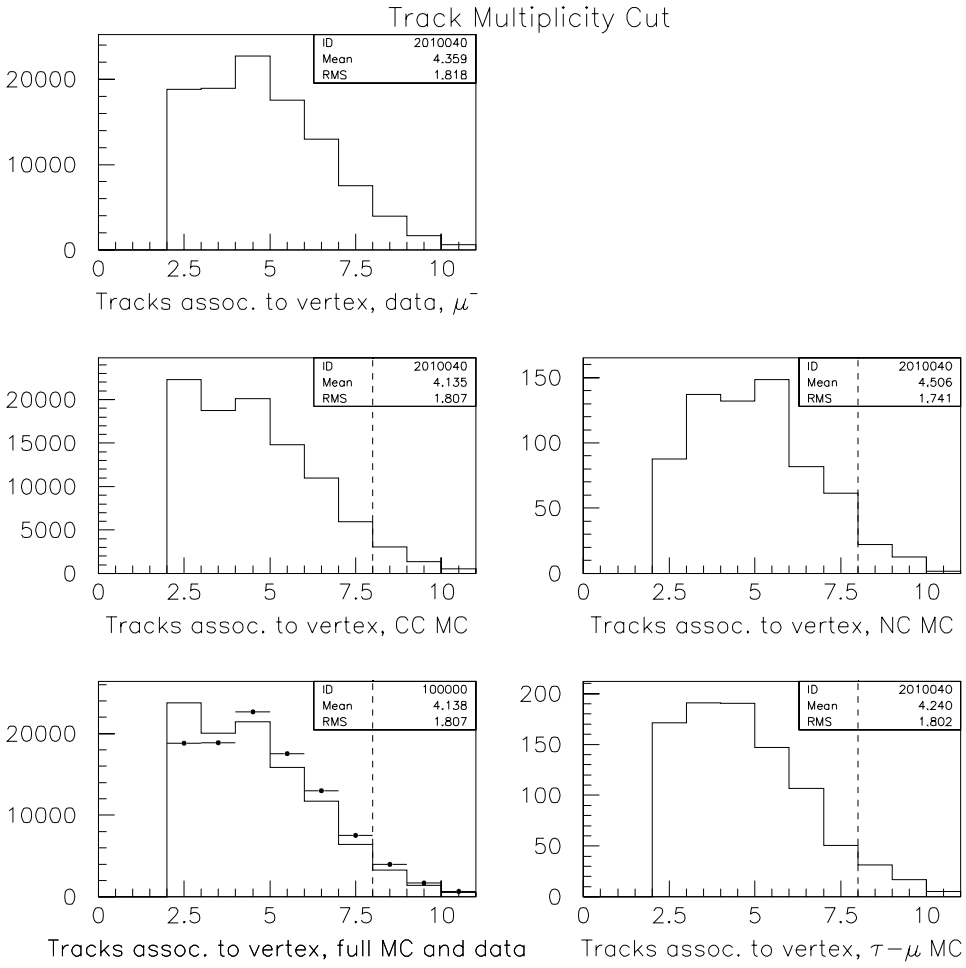

Figure 7.1: Multiplicity distributions and cut. μ^+ data are normally displayed in the upper right (a histogramming error occurred in this instance). For the lower–left plot (comparison of "full MC and data"), μ^- and μ^+ data (dots) have been added; CC and NC Monte Carlo samples (histogram) have been added and renormalized to the area under the data curve.

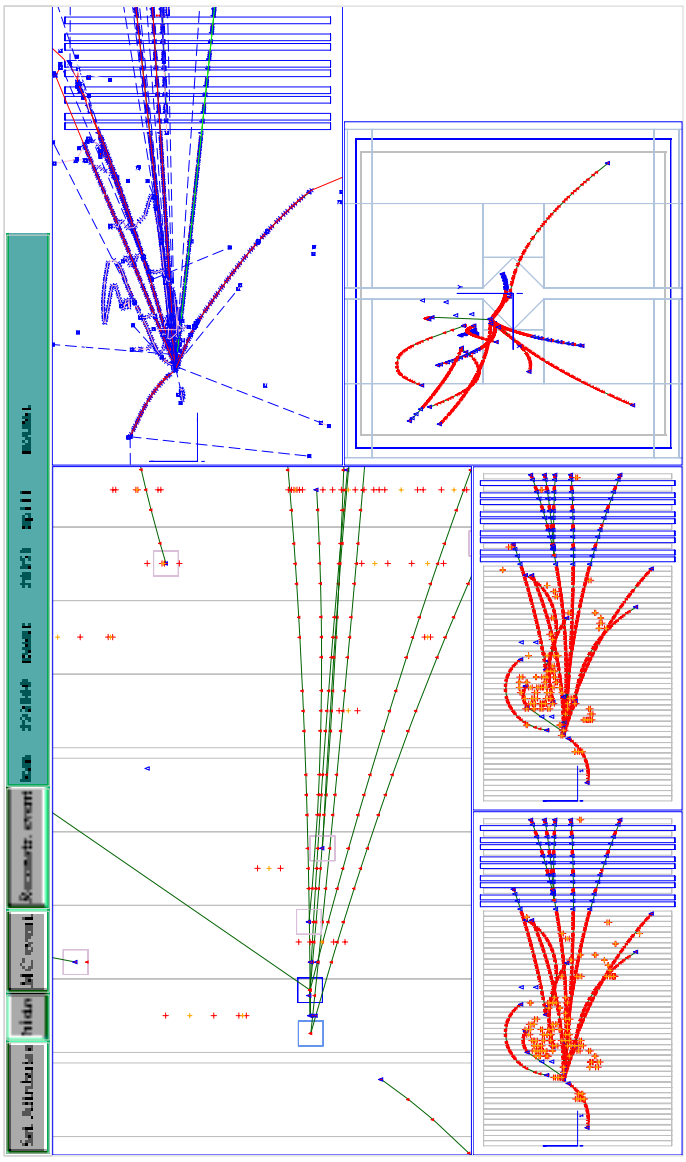

Figure 7.2: Event 28150, run 222000; rejected by multiplicity limit. Clockwise from the bottom left, the views displayed are: yz (side), xz (top), xy (front), and two additional side views showing hits from individual drift chamber wire planes. The region of the primary vertex is enlarged in the main yz panel.

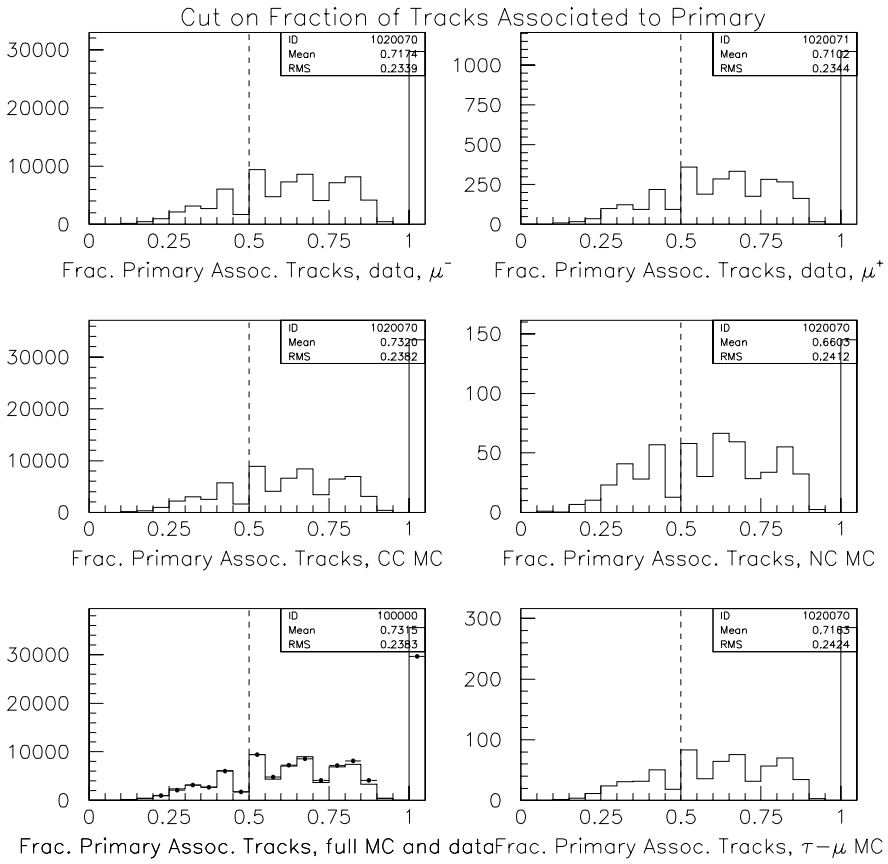

Figure 7.3: Vertex–association ratio distributions and cut

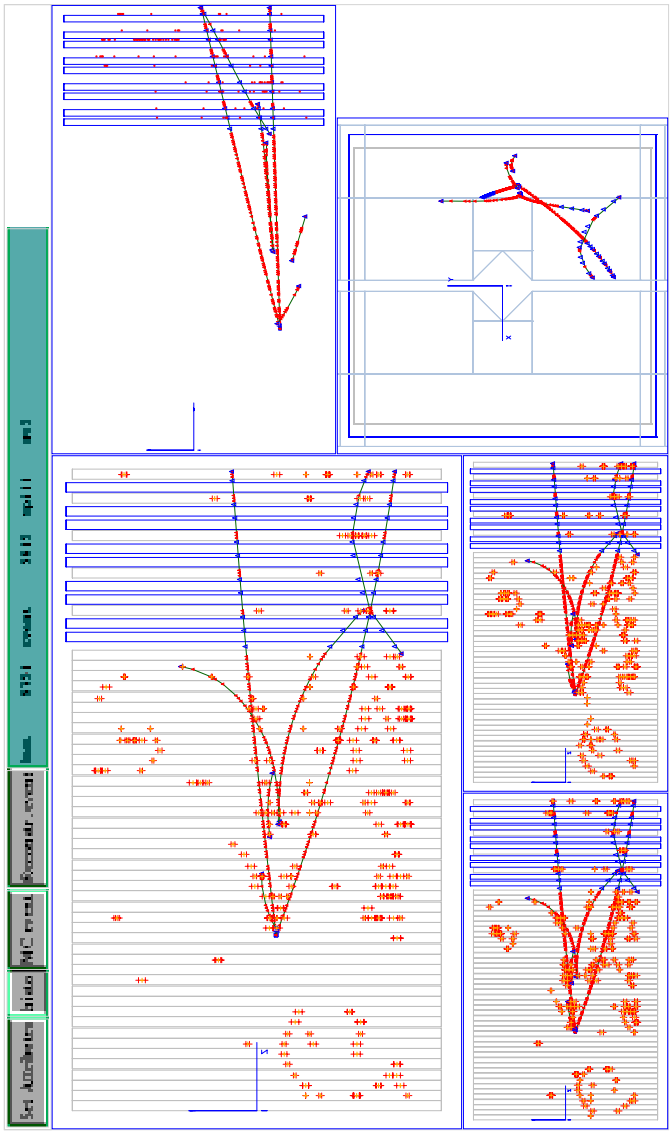

Figure 7.4: Event 5615, run 9751; rejected by vertex–association ratio cut

This event has a large angle (negative?) track at the primary vertex which is not reconstructed. The event in figure 7.7 (charge balance = 3) has 4 positive tracks, including a large-p_T stub at the primary which is also mis-reconstructed.

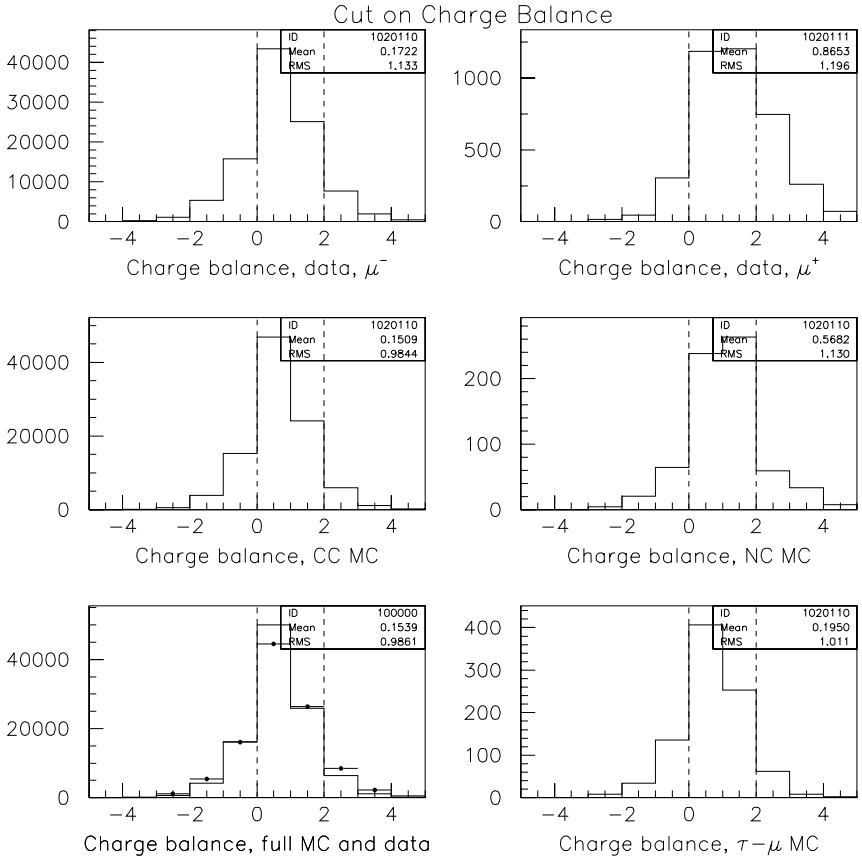

Figure 7.5: Charge balance distributions and cut

5. *Missing-p_T Error:* $\sigma_{p_T} < 0.2$ GeV (figure 7.8). This cut assures that the missing-p_T, involved in the definition of the most crucial selection criteria, is well measured.

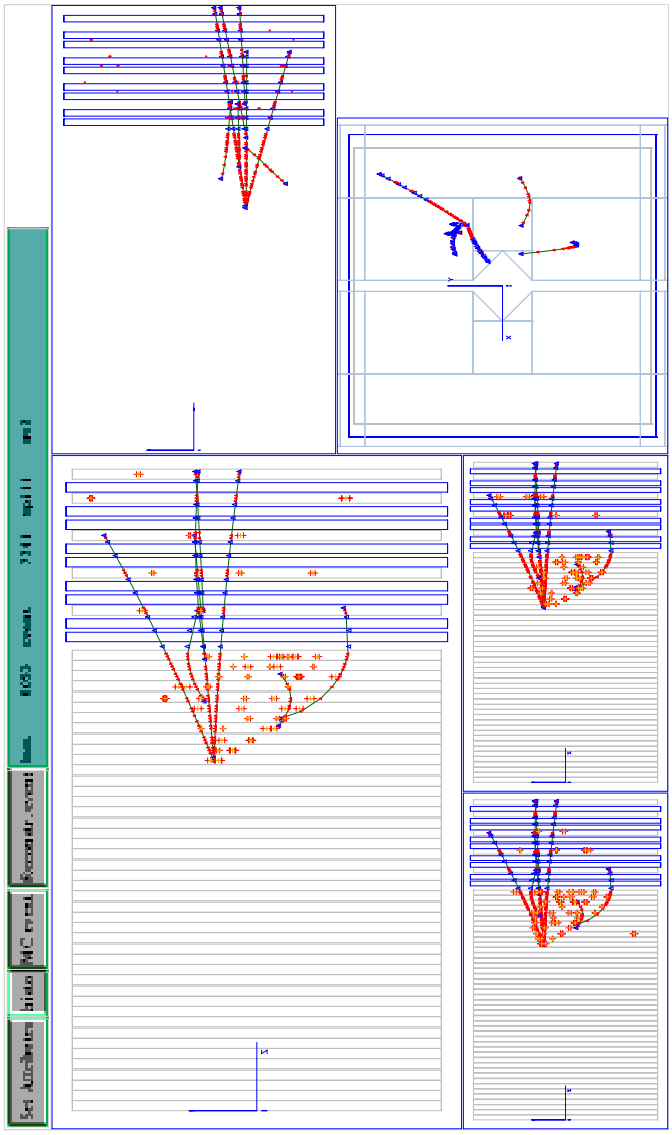

Figure 7.6: Event 7741, run 8053; rejected by charge balance cut

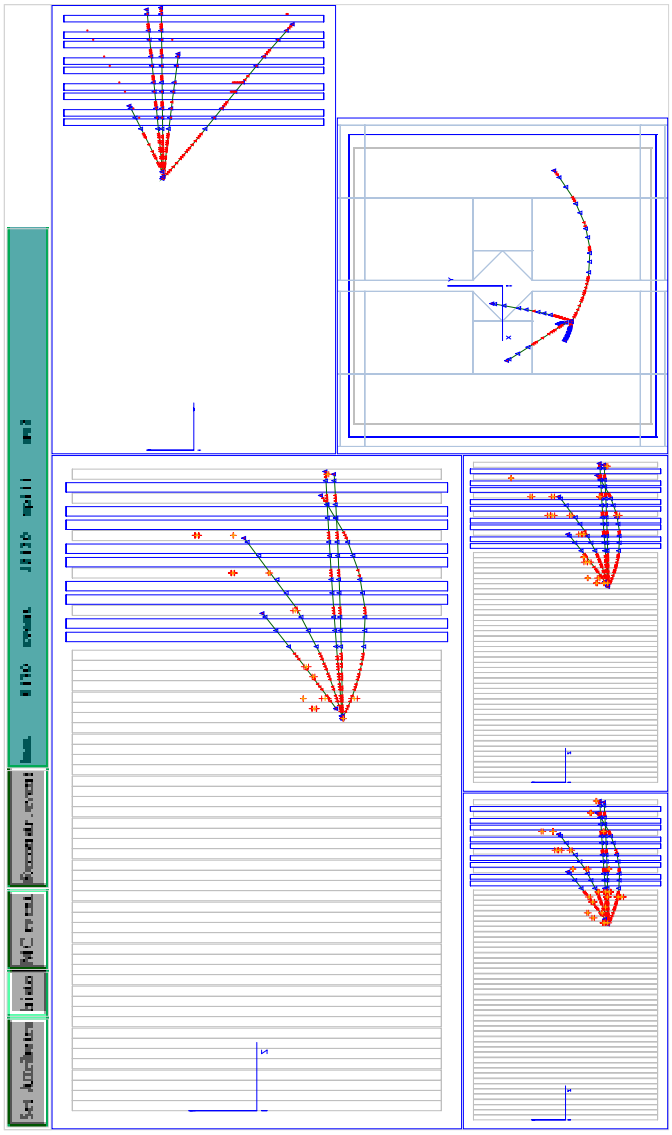

Figure 7.7: Event 12170, run 8170; rejected by charge balance cut

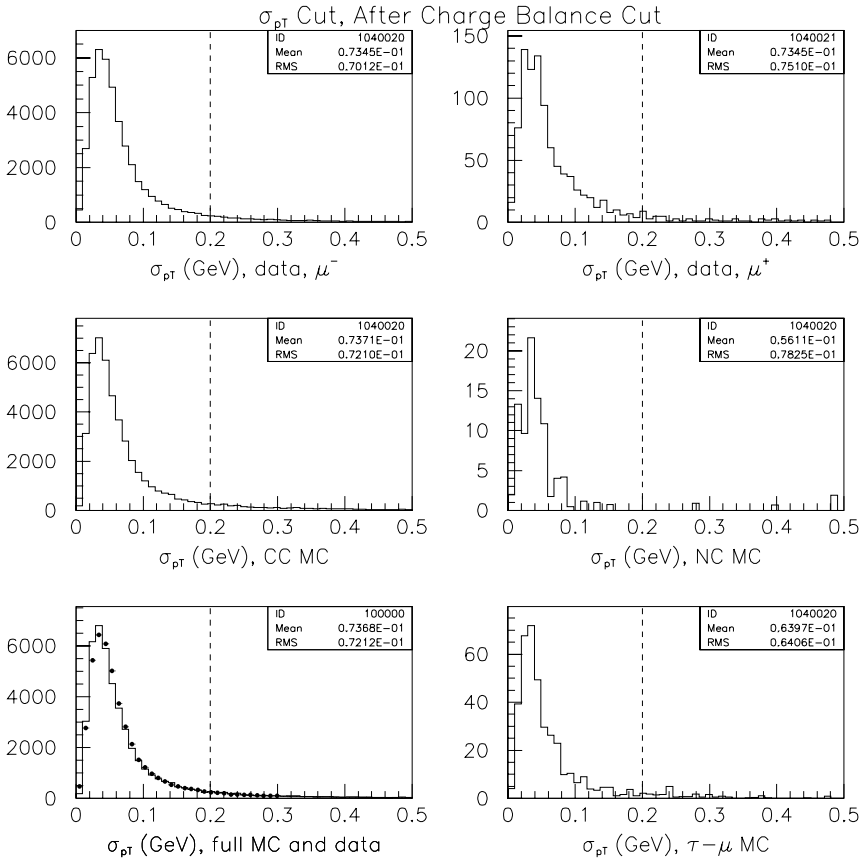

Figure 7.8: Missing-p_T error distributions and cut

6. *Maximum Missing-p_T:* $p_T^{miss} < 3.5$ GeV (figure 7.9). No physical process is known which would produce true p_T^{miss} of order 4 GeV or more in CC events (a Fermi momentum tail of this size can be excluded from the data). Scanning of such events typically reveals severe reconstruction problems in both data and Monte Carlo.

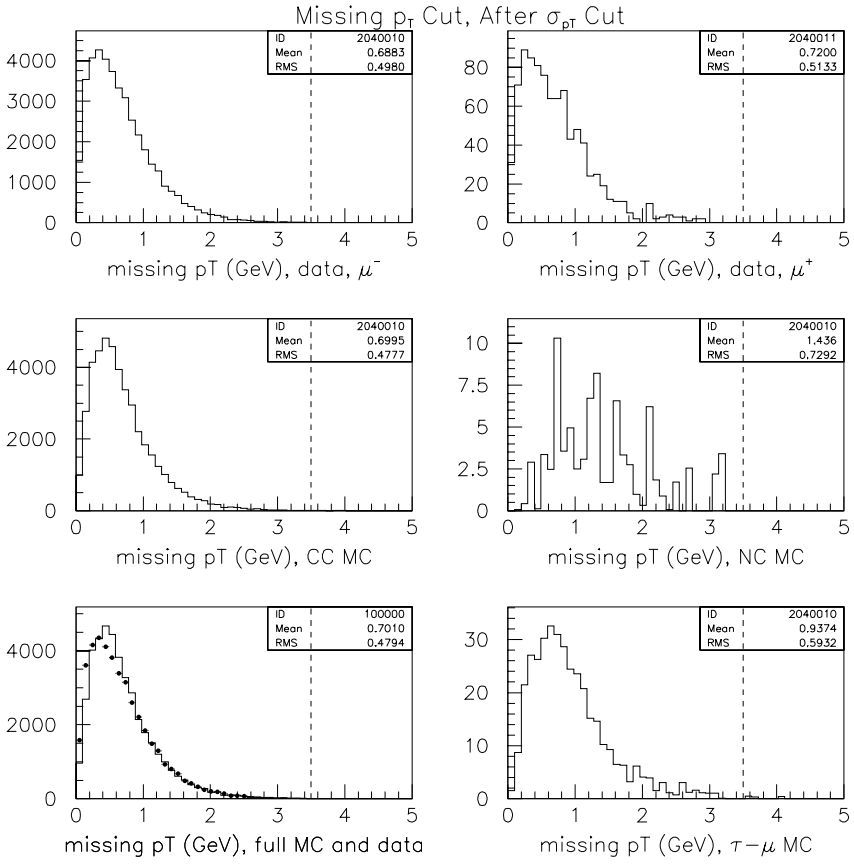

Figure 7.9: Missing-p_T distributions and cut

7. *Energy Consistency:* The total energy recorded in the electromagnetic calorimeter must be less than the total hadronic energy (measured from charged tracks

and isolated neutral calorimeter clusters). This cut helps to eliminate events in which high energy neutral clusters are not recognized due to overlapping charged tracks. For example, in the event in figure 7.10, one photon from a neutral pion decay converts, with the resulting electron overlapping the other decay photon in the calorimeter. None of the 12 GeV of energy deposited is therefore accounted for in the p_T balance. This cut is needed to compensate the deliberate choice of not including overlaps into the missing p_T algorithm (section 7.1.5).

The effect of these cuts is summarized in table 7.4.

Tight Muon and Event Quality Cuts								
	data	*MC CC*		*data*	*MC NC*		*MC* $\tau^- \to \mu^- \nu_\tau \bar{\nu}_\mu$	
	μ^-	*no add.*	*add.*	μ^+	*no add.*	*add.*	*no add.*	*add.*
# events	29300	38779	31232	615	77	64	320	267
efficiency (%)	31	36	32	17	10	9.8	35	30

Table 7.4: Effect of tight quality cuts. Note that the statistics in the Monte Carlo set with additions (sum of μ^- and μ^+) differ from the data by less than 5%. The statistics in the set without additions differ by more than 20%.

7.2 $\nu_\mu \to \nu_\tau$ Oscillation Search

The decay channel through which NOMAD will most likely attain the highest sensitivity in the search for τ–appearance events is $\tau^- \to e^- \nu_\tau \bar{\nu}_e$. The 1% admixture of ν_e in the predominantly ν_μ beam yields a corresponding 100-fold decrease in the CC background for that channel. However, the search strategies used for both of the leptonic decay modes are quite similar, so that the higher statistics in the $\tau^- \to \mu^- \nu_\tau \bar{\nu}_\mu$ channel offers an excellent opportunity to establish how well the behavior of the data and Monte Carlo samples under the τ–event selection cuts is understood. Similar cuts can then be confidently applied to a $\tau^- \to e^- \nu_\tau \bar{\nu}_e$ anal-

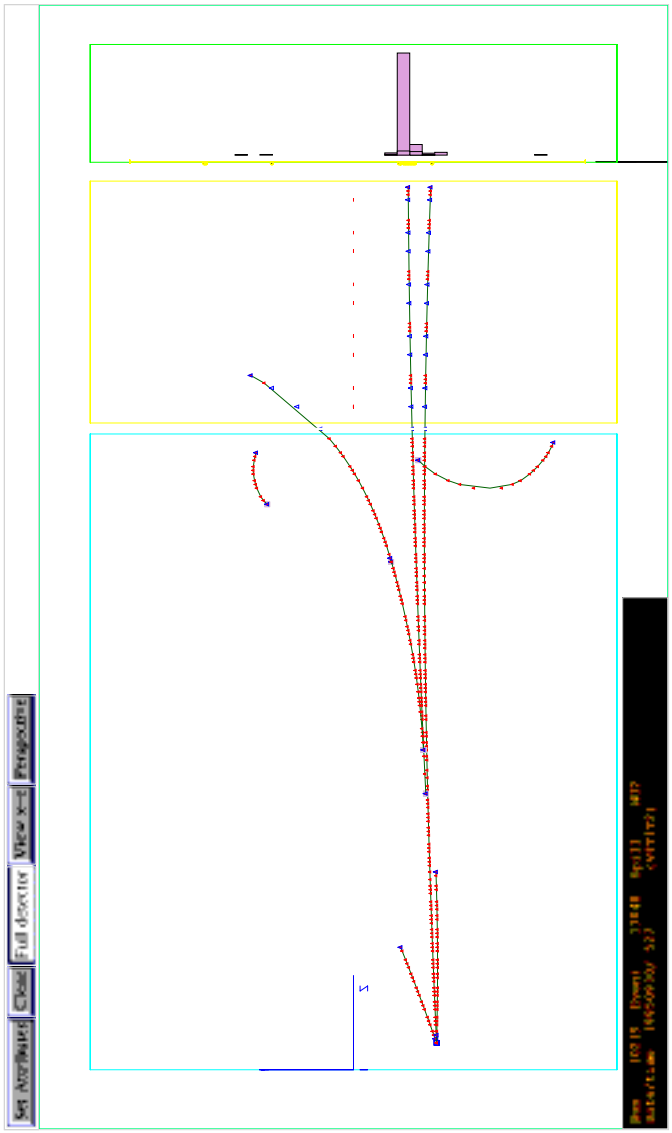

Figure 7.10: Event 13048, run 10219; rejected by the energy consistency cut

ysis. In addition, if the background behavior can be controlled, the $\tau^- \to \mu^- \nu_\tau \bar{\nu}_\mu$ channel might yield a small contribution to a combined limit on the neutrino mixing parameters.

With these goals in mind, a $\tau^- \to \mu^- \nu_\tau \bar{\nu}_\mu$ candidate event search is made, using the Monte Carlo sets both with and without additions. The organization of the tables and distributions used to illustrate the cuts in previous sections is retained.

7.2.1 $\tau^- \to \mu^- \nu_\tau \bar{\nu}_\mu$ Event Selection Cuts

p_T-ratio cut

The principal variable used to distinguish $\tau^- \to \mu^- \nu_\tau \bar{\nu}_\mu$ events from ν_μ CC background is the p_T-ratio. It is defined by:

$$R_{p_T} = \frac{p_T^\mu}{min(p_T^{miss}, p_T^{had})}. \tag{7.4}$$

The cut based on this variable is essentially the same as the traditional cut in the $\phi_{\mu h} - \phi_{mh}$ plane (see section 1.6.1 for an explanation of this cut). As shown in figure 7.11, values of the p_T-ratio represent contours in the $\phi_{\mu h} - \phi_{mh}$ plane. The contour most closely approximating the $\phi_{\mu h} - \phi_{mh}$ cut as suggested in the NOMAD proposals for the $\tau^- \to \mu^- \nu_\tau \bar{\nu}_\mu$ analysis corresponds to a p_T-ratio of about 0.4. Unlike the $\phi_{\mu h} - \phi_{mh}$ cut, the contour encloses the corners of the plane, a possible source of background.

The p_T-ratio distributions are shown in figure 7.12. A loose requirement, p_T-ratio < 1, (dashed line) is chosen to pre–select events in the signal region such that the behavior of subsequent cuts in this region is not obscured by the much larger contribution from the background. Figure 7.13 shows the same distributions without the Monte Carlo additions. The significant improvement in the agreement between data and Monte Carlo distributions with additions (especially within the signal region) is offered as further motivation for the detailed study of nuclear and reconstruction effects. The improved agreement is also shown in the effect of the

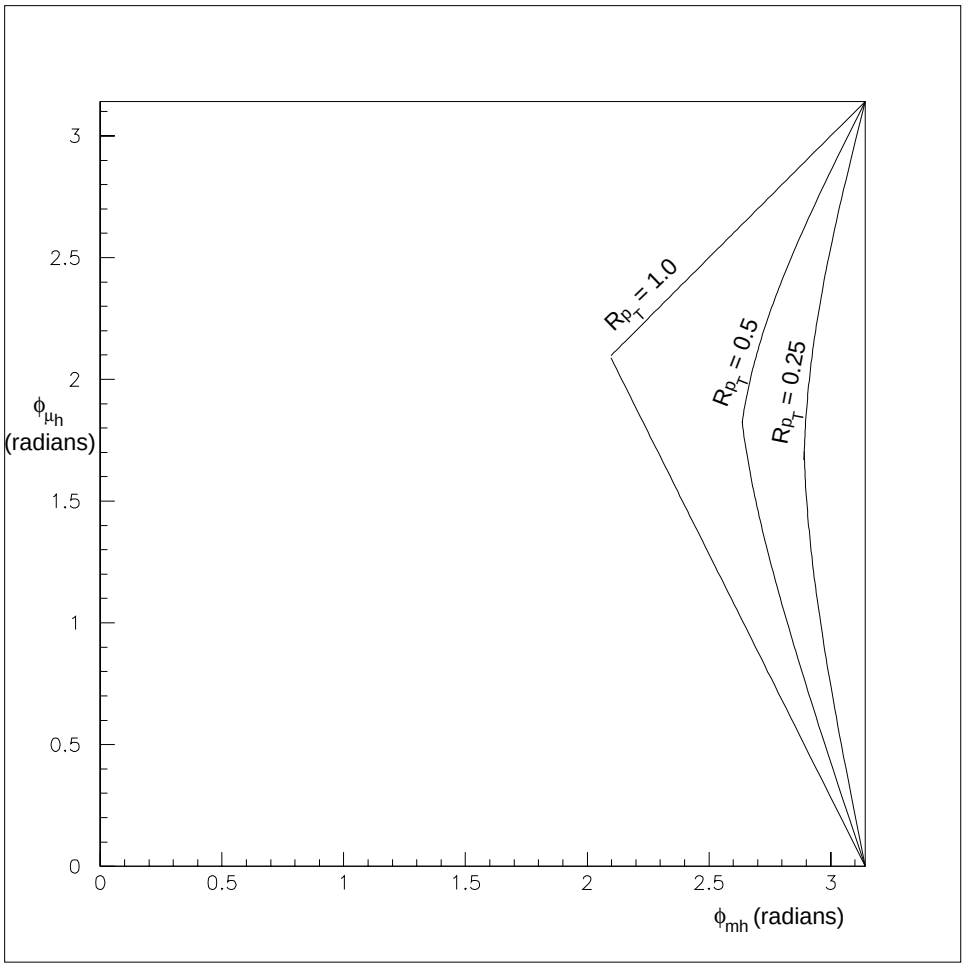

Figure 7.11: Contours in the $\phi_{\mu h} - \phi_{mh}$ plane for three different values of the p_T-ratio ($\mathrm{R_{pT}}$). The two values chosen for this analysis are $\mathrm{R_{pT}} < 1.0$ and $\mathrm{R_{pT}} < 0.5$. The cut originally proposed corresponds to about $\mathrm{R_{pT}} < 0.4$, with further exclusion in the corners.

cut, summarized in table 7.5. For all subsequent plots, only the MC with additions is shown.

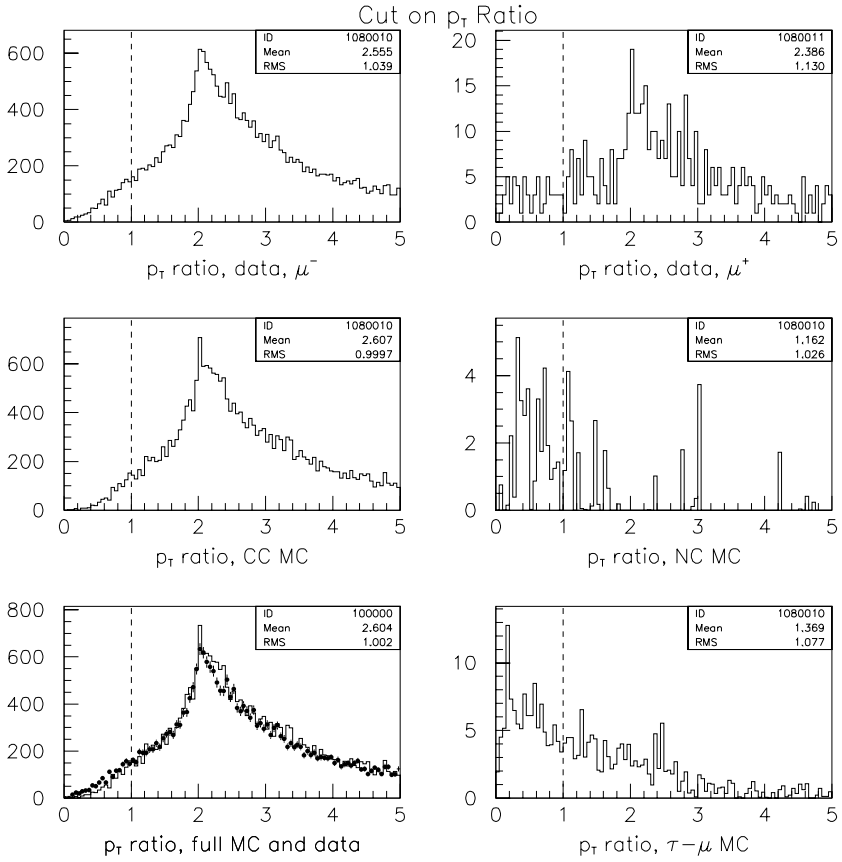

Figure 7.12: p_T-ratio distributions for data and MC sets, with cut at $R_{p_T} > 1.0$ (dashed line).

$q_{T\mu}$ cut

In this analysis, $q_{T\mu}$ is defined as the magnitude of the momentum of the final–state muon transverse to the total reconstructed momentum vector. The total momen-

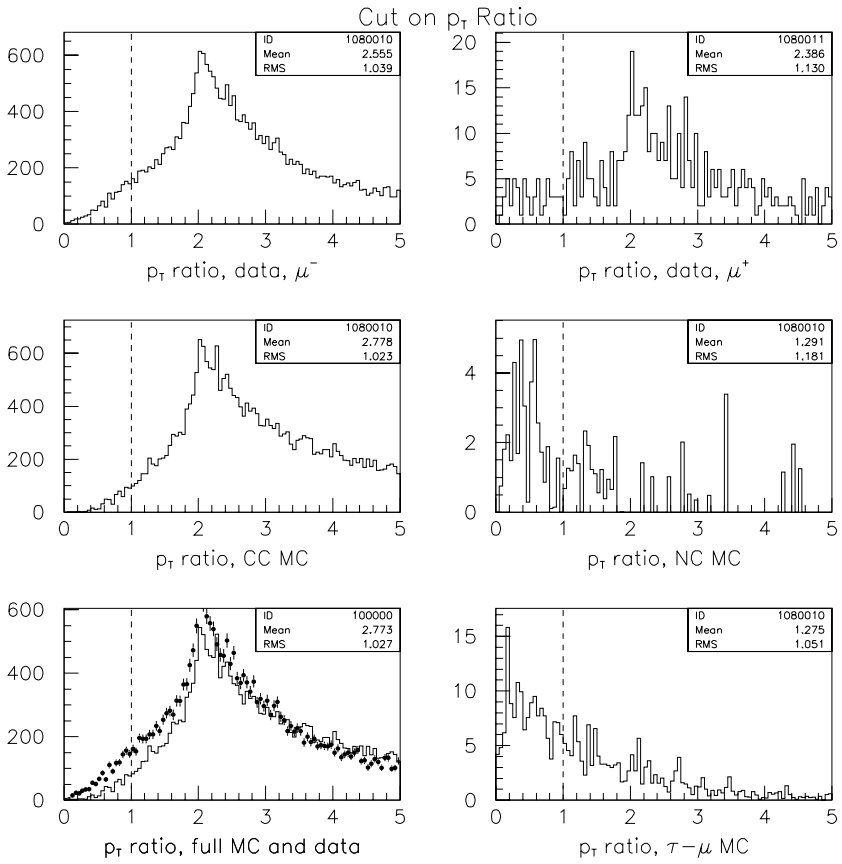

Figure 7.13: p_T-ratio cut, without smearing or nuclear effects applied to the Monte Carlo distributions. Significant discrepancies remain in the signal region.

p_T–ratio cut								
	data	*MC CC*		*data*	*MC NC*		*MC* $\tau^- \to \mu^- \nu_\tau \bar{\nu}_\mu$	
	μ^-	*no add.*	*add.*	μ^+	*no add.*	*add.*	*no add.*	*add.*
# events	1320	656	977	58	41	37	154	115
efficiency (%)	5.0	1.7	3.1	9.4	53	58	48	43

Table 7.5: Effect of p_T-ratio cut

tum is composed from the muon momentum and the hadronic jet as defined in section 7.1.5. A requirement of $q_{T\mu} > 0.5$ GeV removes a significant portion of the remaining NC background events (figure 7.14). The effect of this cut is summarized in table 7.6.

$\mathbf{q_{T\mu}}$ **cut**								
	data	*MC CC*		*data*	*MC NC*		*MC* $\tau^- \to \mu^- \nu_\tau \bar{\nu}_\mu$	
	μ^-	*no add.*	*add.*	μ^+	*no add.*	*add.*	*no add.*	*add.*
# events	974	517	750	22	10	10	126	88
efficiency (%)	74	79	77	38	24	27	82	77

Table 7.6: Effect of $q_{T\mu}$ cut

Q^2 Consistency Cut

The Q^2 consistency cut is motivated by the observation that the ν_μ CC background events surviving the p_T-ratio cut have low average Q^2 relative to the original events. This is to be expected since the p_T–ratio cut selects events with low $p_{T\mu}$, which, for the case of ν_μ CC background events, is related to Q^2 by the relationship:

$$Q^2 \simeq \frac{E_\nu}{E_\mu} \frac{p_{T\mu}^2}{\cos^2\left(\frac{\theta}{2}\right)}, \tag{7.5}$$

where E_ν and E_μ are the incident neutrino and final state muon energies, and θ is the muon polar angle (Note: for a typical event selected by the p_T-ratio cut, E_ν and E_μ are on the order of 10 GeV each, and $\theta \simeq 0$, so that usually a factor of unity

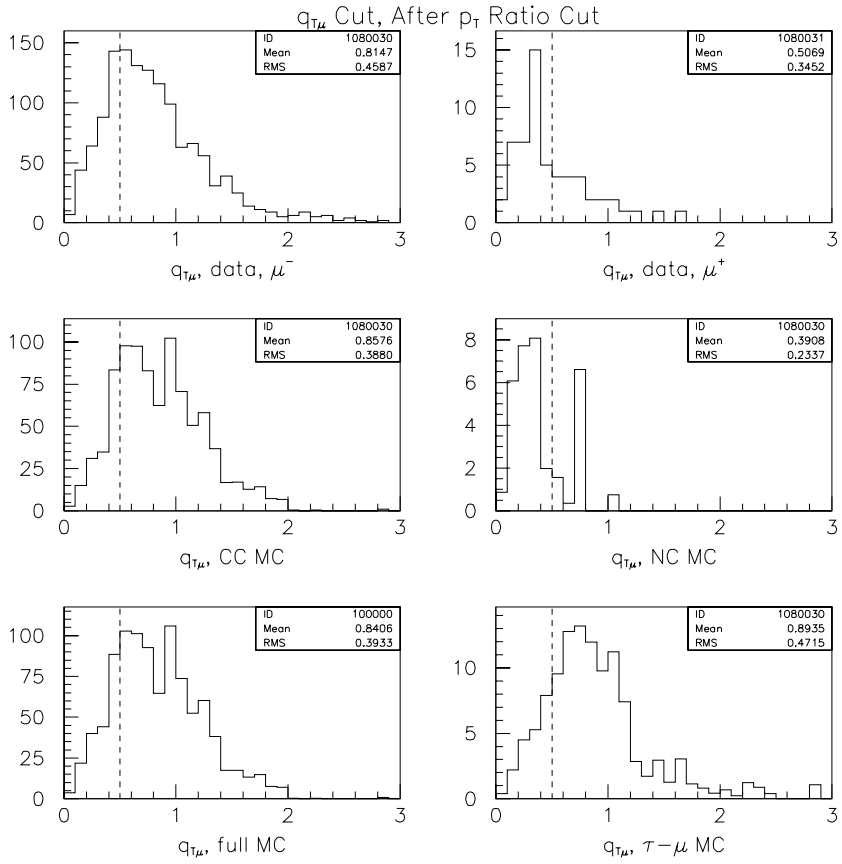

Figure 7.14: $q_{T\mu}$ distributions and cut

multiplies $p_{T\mu}^2$ in the equation). No such relationship holds for $\tau^- \to \mu^- \nu_\tau \bar{\nu}_\mu$ events. Q^2 is determined conventionally for each event via the final–state muon, with the expression:

$$Q_{lep}^2 = -m_\mu^2 + 2E_\mu E_{vis}\left(1 - \frac{|p_\mu|}{E_\mu}\cos\theta\right), \tag{7.6}$$

where θ is the muon polar angle in the beam system and E_{vis} is defined in section 7.1.5. Due to the presence of the two additional final–state neutrinos in $\tau^- \to \mu^- \nu_\tau \bar{\nu}_\mu$ events, this expression will lead to a consistent underestimate of the true value of Q^2 for the signal. It should therefore be possible to isolate a portion of the surviving background events with some measure of Q^2 other than that obtained with the final–state muon.

For each event, Q^2 is also measured from the hadronic jet using the expression:

$$Q_{jet}^2 = 2E_{jet}m_N - m_N^2 - W_{jet}^2, \tag{7.7}$$

where m_N is the nucleon mass. W_{jet}^2 is the invariant jet mass, as measured from jet parameters alone. It is the most difficult parameter to estimate in equation 7.7, as the masses of the jet particles enter directly. For this purpose, each jet track is assigned the pion mass, with the exception of one positive track (if any) per event meeting certain kinematic criteria, which is assigned the proton mass. For this analysis, the criteria are simply that the momentum fall within 1 GeV and 4 GeV, and the polar angle within 0.2 radians and 0.6 radians, as suggested by a simple study of ν_μ CC NEGLIB events. This approximation leads to an underestimate of W_{jet}^2 and an overestimate of Q_{jet}^2 (figure 7.15), desirable for the design of a conservative cut for low–Q_{jet}^2 events.

Finally, a powerful cut is obtained using the ratio:

$$\frac{Q_{jet}^2 - Q_{lep}^2}{Q_{jet}^2 + Q_{lep}^2} \tag{7.8}$$

or Q^2 consistency. This ratio exploits the fact that Q_{lep}^2 consistently underestimates the actual Q^2 in signal events, as shown in figure 7.15, while Q_{jet}^2 holds for both τ and background events. Q^2 consistency distributions for data and Monte

Carlo sets before the p_T-ratio cut are shown in figure 7.16. The distribution for the $\tau^- \to \mu^- \nu_\tau \bar{\nu}_\mu$ events is much harder, in accordance with the consistently low values of Q^2_{lep}. The discrepancy between data and Monte Carlo at high Q^2 consistency is not fully understood. Preliminary investigations seem to indicate that the excess in the data could be due to coherent pion production events (not simulated in NEGLIB), with an admixture of low–multiplicity events in which Q^2_{jet} is underestimated due to missing neutrals.

The distributions after the p_T-ratio and $q_{T\mu}$ cuts (figure 7.17) are all considerably harder, demonstrating the tendency of the p_T-ratio cut to select events with low Q^2_{lep} in all samples. A requirement of Q^2 consistency > 0.75 is imposed. Higher tails below the cut remain to distinguish ν_μ CC events from $\tau^- \to \mu^- \nu_\tau \bar{\nu}_\mu$ events. The effect of the cut is summarized in table 7.7. The efficiency for removing events in the data and the CC Monte Carlo set with additions is nearly identical.

Q^2 Consistency Cut								
	data	*MC CC*		*data*	*MC NC*		*MC* $\tau^- \to \mu^- \nu_\tau \bar{\nu}_\mu$	
	μ^-	*no add.*	*add.*	μ^+	*no add.*	*add.*	*no add.*	*add.*
# events	447	323	354	10	8.7	8.8	84	62
efficiency (%)	46	62	47	45	87	88	67	70

Table 7.7: Effect of Q^2 consistency cut

Jet collimation cut

In order to remove background from low–Q^2, high–W events, for which the missing-p_T direction is often not well defined, all events are subject to a requirement based on the fraction of hadronic momentum falling within the hemisphere defined by the hadronic jet. Once the jet is defined, the relative direction of each hadronic track is checked and the momenta of tracks falling within the jet hemisphere are added to a

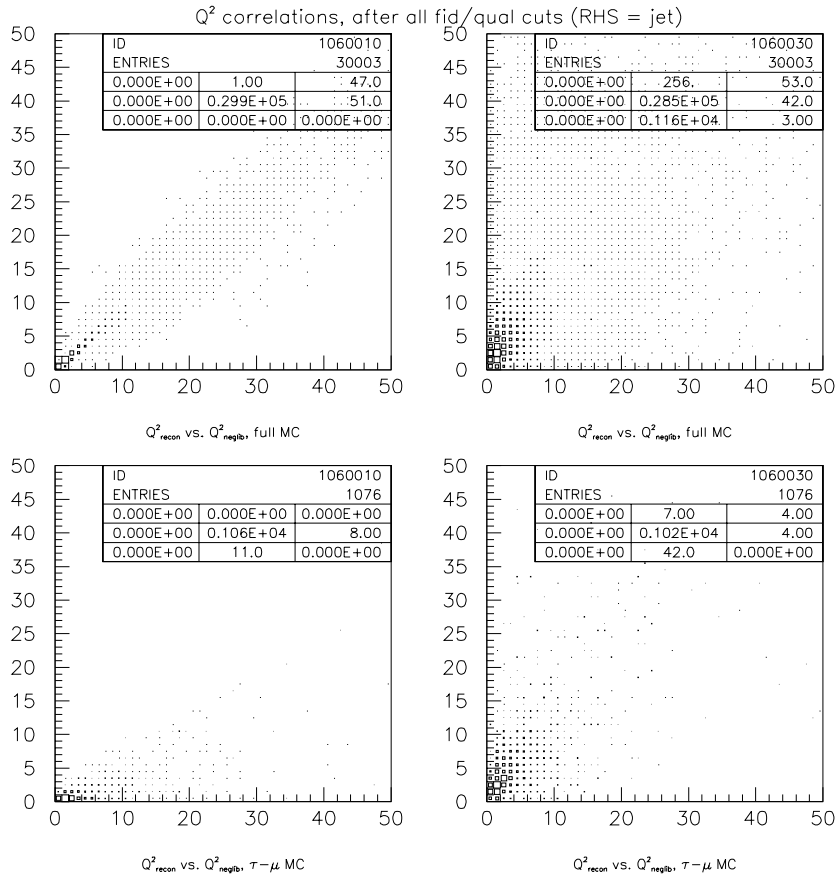

Figure 7.15: Q^2 (reconstructed) vs. Q^2 (NEGLIB). The two upper plots display statistics from the combined CC and NC Monte Carlo samples. The two lower plots display $\tau^- \to \mu^- \nu_\tau \bar{\nu}_\mu$ events. In the two plots on the left, Q^2 is calculated from the final state muon; in the plots on the right, from the hadronic jet. Note that Q^2_{jet} is consistently over-estimated in reconstructed CC and NC events, and that Q^2_{lep} is under-estimated in signal events.

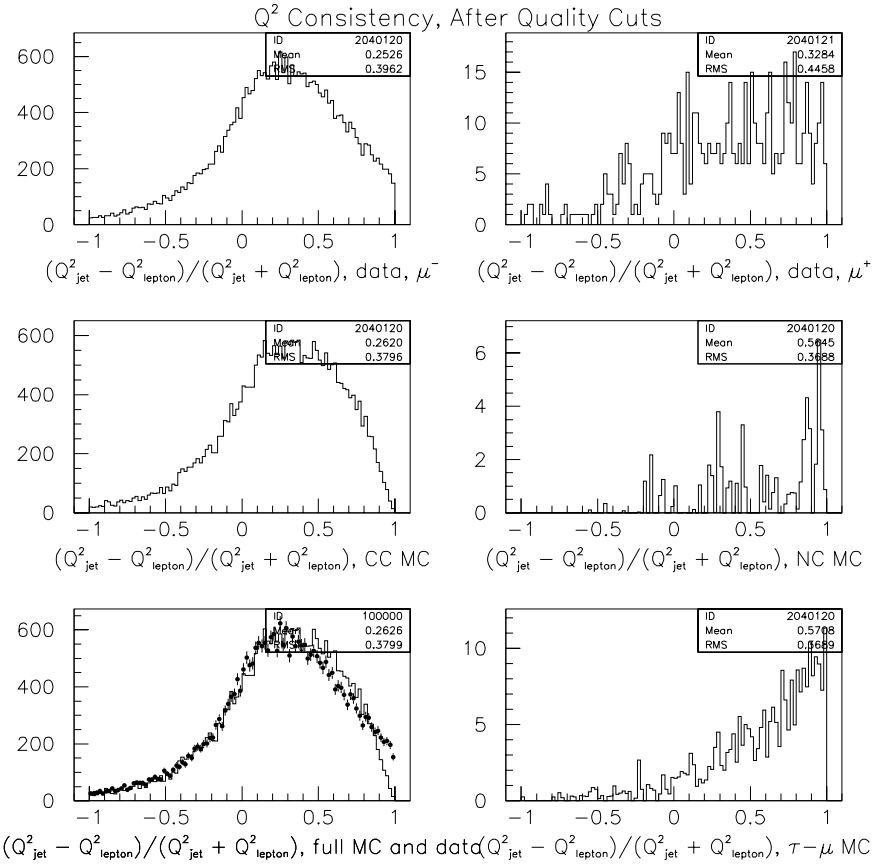

Figure 7.16: Q^2 consistency distributions before $\tau^- \to \mu^- \nu_\tau \bar{\nu}_\mu$ selection cuts.

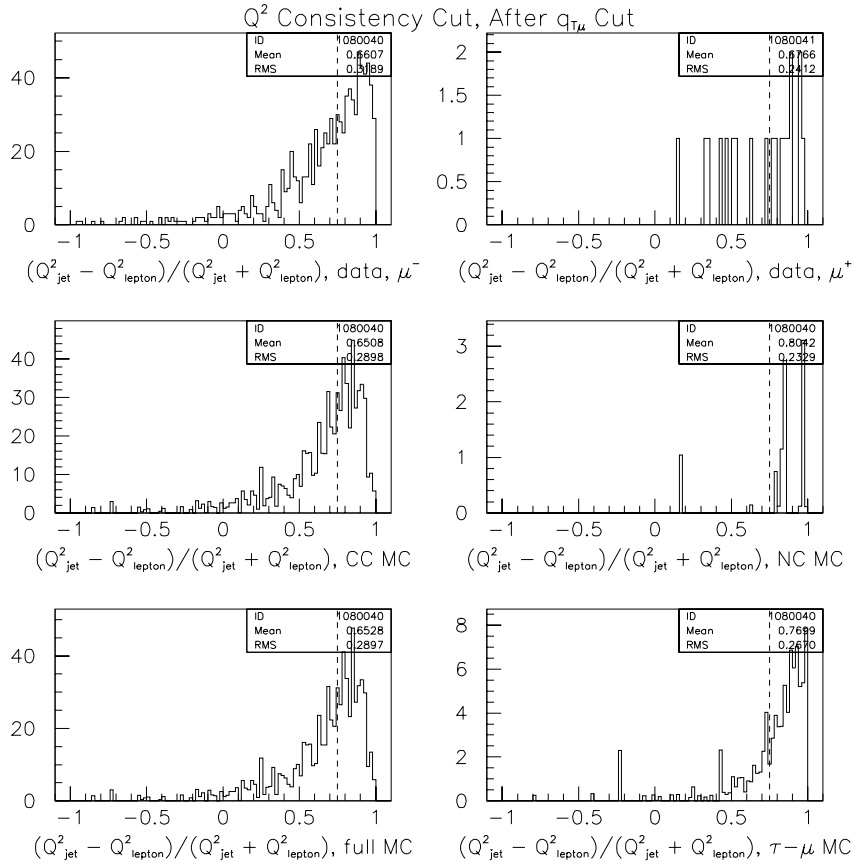

Figure 7.17: Q^2 consistency distributions and cut, after the $q_{T\mu}$ cut. Tails below 0.75 are less pronounced in the $\tau^- \to \mu^- \nu_\tau \bar{\nu}_\mu$ event sample.

running total. The requirement is defined by:

$$\frac{\sum_i |\vec{p}_i|}{|\vec{p}_{jet}|} > 0.8, \tag{7.9}$$

where i runs over all hadron tracks in the jet hemisphere. The distributions are shown in figure 7.18, and the effect of the cut in table 7.8.

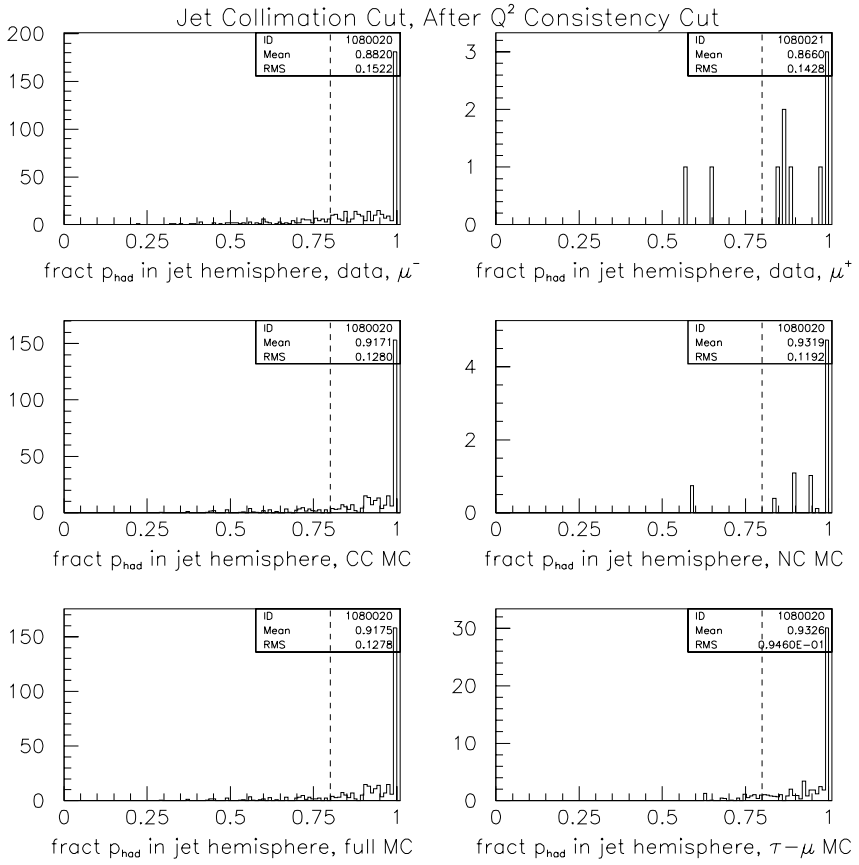

Figure 7.18: Jet collimation distributions and cut

Jet Collimation Cut								
	data	*MC CC*		*data*	*MC NC*		*MC* $\tau^- \to \mu^- \nu_\tau \bar{\nu}_\mu$	
	μ^-	*no add.*	*add.*	μ^+	*no add.*	*add.*	*no add.*	*add.*
# events	343	268	305	8	6.7	8.0	77	54
efficiency (%)	77	83	86	80	84	91	92	87

Table 7.8: Effect of jet collimation cut

Missing-p_T cut

In contrast to what was conjectured in the proposal, a cut on the missing-p_T angular correlations (p_T-ratio) alone turns out not to be sufficient to reduce the background to an acceptable level. Instead, an additional cut on the magnitude of the missing p_T is found to be helpful.

Remaining events are required to have missing-p_T greater than 1.6 GeV. While detrimental to the $\tau^- \to \mu^- \nu_\tau \bar{\nu}_\mu$ event selection efficiency, this cut removes most of the surviving CC and NC background events (figure 7.19 and table 7.9).

The events in the high-p_T tail of $\tau^- \to \mu^- \nu_\tau \bar{\nu}_\mu$ distribution are scanned individually to check for reconstruction problems. A typical $\tau^- \to \mu^- \nu_\tau \bar{\nu}_\mu$ Monte Carlo event is shown in figure 7.20. The events appear well–reconstructed, with the large missing–p_T resulting from the two final–state neutrinos from the τ–decay, which are clearly isolated in the transverse plane from most of the charged activity.

Final Missing-p_T Cut								
	data	*MC CC*		*data*	*MC NC*		*MC* $\tau^- \to \mu^- \nu_\tau \bar{\nu}_\mu$	
	μ^-	*no add.*	*add.*	μ^+	*no add.*	*add.*	*no add.*	*add.*
# events	5	1.1	0.5	0	0.3	0.3	25	17
efficiency (%)	1.5	0.4	0.2	0.0	4.5	3.7	32	31

Table 7.9: Effect of missing-p_T cut

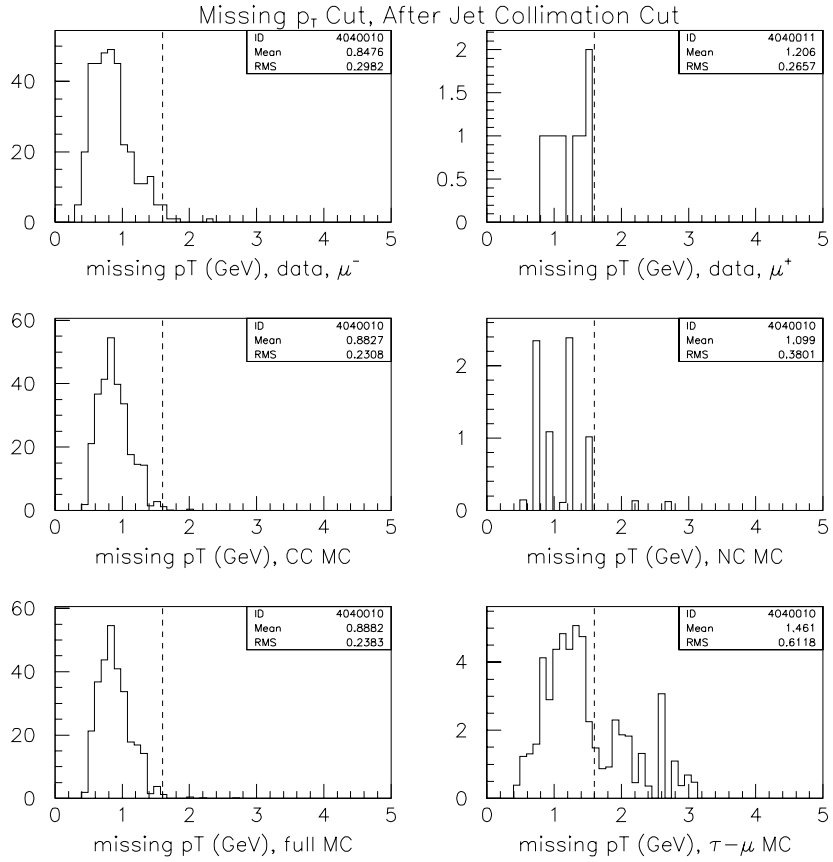

Figure 7.19: Missing-p_T distributions of remaining events, and cut

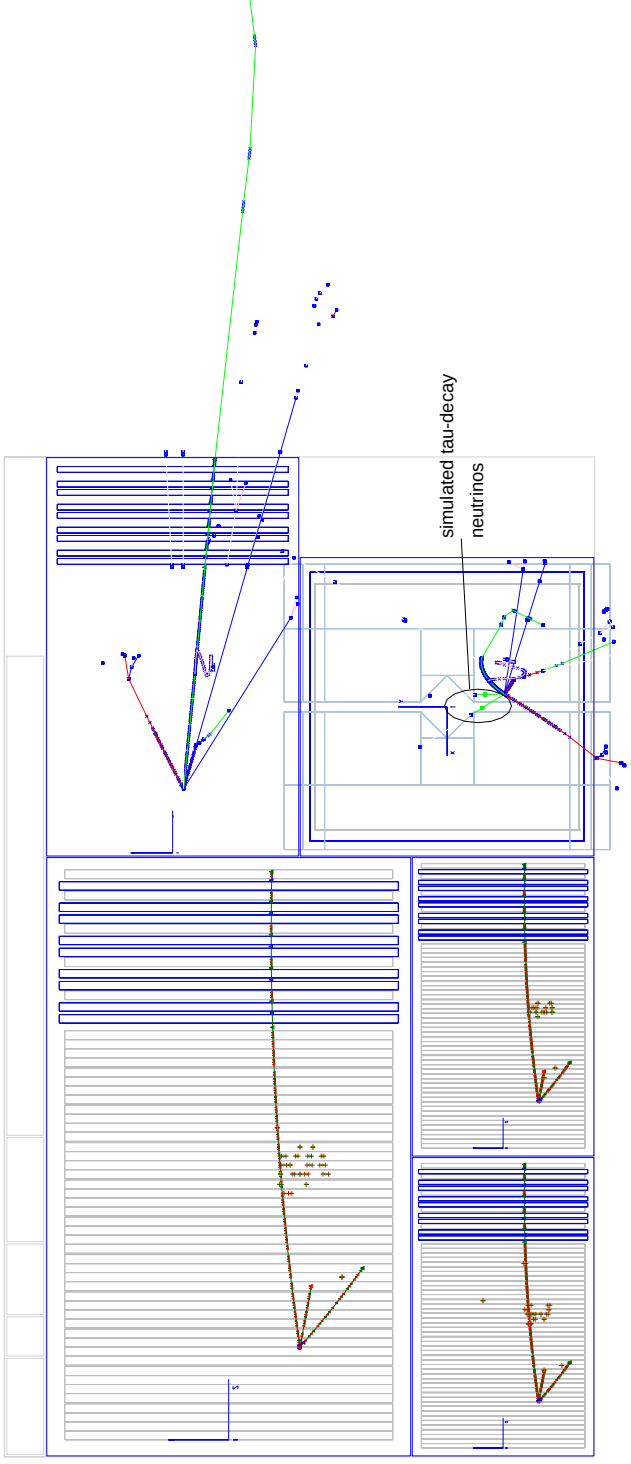

Figure 7.20: Example of $\tau^- \to \mu^- \nu_\tau \bar{\nu}_\mu$ event surviving missing-p_T cut (event 2118, run 252006). Note the direction of the two neutrinos in the transverse plane. The value of the true neutrino p_T is 1.6 GeV.

Transverse $\mathbf{m_\tau}$, $\mathbf{y_{Bjorken}}$, and Tight p_T-ratio cuts

The remaining three requirements in the $\tau^- \to \mu^- \nu_\tau \bar{\nu}_\mu$ event selection are defined by:

1. *Transverse τ mass:* 0.2 GeV $< m_\tau <$ 2.0 GeV
2. $y_{Bjorken} > 0.25$, calculated from the expression $y_{bj} = \nu / E_{vis}$, with ν and E_{vis} as defined in section 7.1.5.
3. p_T-ratio < 0.5

At this stage of the analysis, the remaining Monte Carlo event statistics are so poor that it is impossible to deduce reasonable cut values from the Monte Carlo alone.

Despite the bias this introduces, the combination is adjusted empirically to simultaneously eliminate both all background from the remaining CC and NC samples, and all remaining data candidates, sacrificing as few $\tau^- \to \mu^- \nu_\tau \bar{\nu}_\mu$ events as possible. The effect of these cuts is summarized in table 7.10.

The p_T-ratio cut removes one final event each in the CC background (p_T-ratio = 0.59) and data (p_T-ratio = 0.73) samples. The y_{bj} cut, while qualitatively motivated by the y_{bj} distribution at earlier stages of the analysis which is harder for $\tau^- \to \mu^- \nu_\tau \bar{\nu}_\mu$ candidates than for the CC background (figure 7.21), is quantitatively somewhat biased by the one final data event it removes ($y_{bj} = 0.09$, see table 7.12). Another event, at $y_{bj} = 0.14$, also fails the m_τ cut. Finally, the m_τ cut is mainly motivated by the Monte Carlo, since it has no effect at all on the data if applied as the last cut (table 7.12). The lower cut removes events in the upper right hand corner of the $\phi_{\mu h} - \phi_{mh}$ plot (fig. 7.11), where the missing p_T and the muon are parallel (possibly due to mismeasured muon momentum). The upper cut reflects the physical constraint imposed by the τ mass.

Each of these cuts has about 94% $\tau^- \to \mu^- \nu_\tau \bar{\nu}_\mu$ selection efficiency, so the potential bias introduced by this procedure is hoped to be small compared to the

statistical and systematic errors (25% each) used for the final result. Clearly, more Monte Carlo statistics is needed in future analyses to avoid this problem.

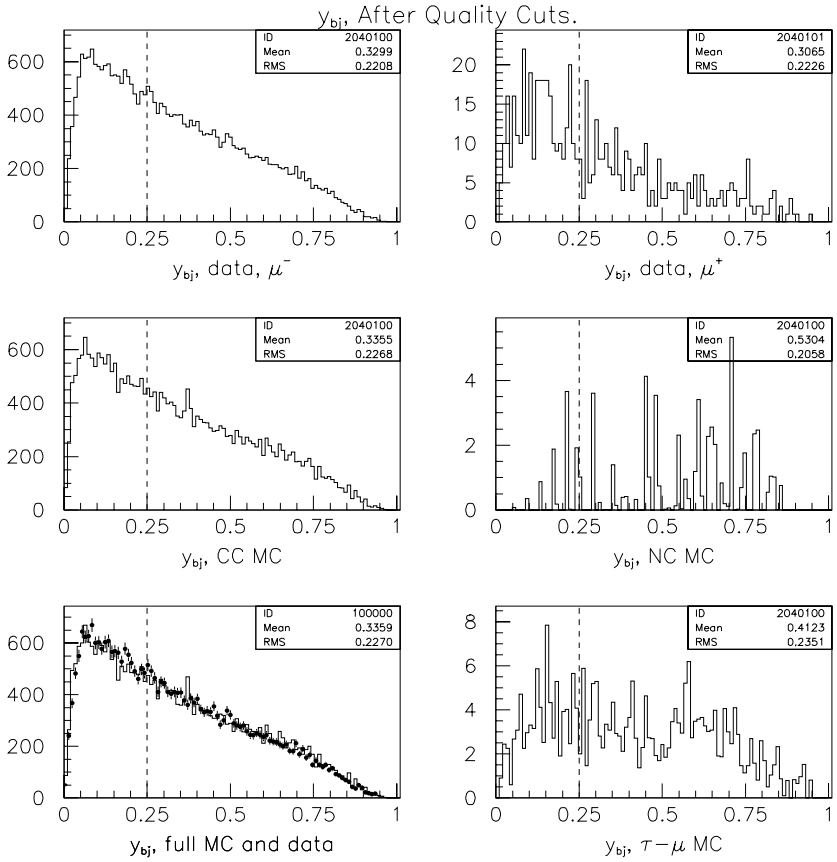

Figure 7.21: y_{bj} distributions of event samples after quality cuts, with dashed lines indicating position of selection cut at a later stage.

7.2.2 Signal Selection Efficiency

The results of the $\tau^- \to \mu^- \nu_\tau \bar{\nu}_\mu$ selection cuts on the entire data and Monte Carlo sets are summarized in table 7.11. Initial Monte Carlo samples are those events

Final Event Selection									
cut		*data* μ^-	*MC CC*		*data* μ^+	*MC NC*		*MC* $\tau^- \to \mu^-\nu_\tau\bar{\nu}_\mu$	
			no add.	*add.*		*no add.*	*add.*	*no add.*	*add.*
$M_{T\tau}$	*# events*	2	0.9	0.4	0	0.1	0.0	22	16
	efficiency (%)	40	82	80	-	33	0.0	88	94
y_{bj}	*# events*	1	0.9	0.4	0	0.1	0.0	21	15
	efficiency (%)	50	100	100	-	100	-	95	94
p_T ratio	*# events*	0	0.5	0.0	0	0.1	0.0	19	14
	efficiency (%)	0.0	56	0.0	-	100	-	90	93

Table 7.10: Effect of final selection cuts

falling in the fiducial volume defined in section 7.1.1. The statistical uncertainty of the efficiencies, calculated from the sum of the weights of the remaining $\tau^- \to \mu^-\nu_\tau\bar{\nu}_\mu$ events in quadrature, is approximately 0.2% for Monte Carlo sets both with and without additions.

Event Selection Summary								
	data μ^-	*MC CC*		*data* μ^+	*MC NC*		*MC* $\tau^- \to \mu^-\nu_\tau\bar{\nu}_\mu$	
		no add.	*add.*		*no add.*	*add.*	*no add.*	*add.*
Initial events	95212	184484	184484	3628	50234	50234	1820	1820
Final events	0	0.5	0.0	0	0.1	0.0	19	14
efficiency (%)							1.0	0.8

Table 7.11: Event selection summary

Using the selection cuts from the last section, no $\tau^- \to \mu^-\nu_\tau\bar{\nu}_\mu$ candidates in the data are observed. In the Monte Carlo sets with additions, no background events are expected, and the selection efficiency is $[0.8 \pm 0.2]$%. In the Monte Carlo set without additions, 0.6 background events are expected, and the efficiency is $[1.0 \pm 0.2]$%. The Monte Carlo additions result in an efficiency loss on the order of 25%.

Due to the uncertainty, as of this writing, over the correct way to account for the τ mass effect, the $\tau^- \to \mu^-\nu_\tau\bar{\nu}_\mu$ selection is repeated on the Monte Carlo set with corrections, but without including the mass correction in the event weights

(section 7.1.2). The resulting efficiency is observed to decrease by about 25%.

7.3 Additional Consistency Checks

From the statistics in the last section, the behavior of the data under the $\tau^- \to \mu^- \nu_\tau \bar{\nu}_\mu$ selection cuts appears to be more consistent with that of the Monte Carlo set with additions. An additional check as to the consistency of the two Monte Carlo sets is obtained by removing individual $\tau^- \to \mu^- \nu_\tau \bar{\nu}_\mu$ selection cuts, and comparing the number of additional surviving events with that obtained in the data. For each selection cut released, the number of additional survivors in each set is listed in table 7.12. In the cases where two cuts are made in the analysis on the same variable (p_T-ratio, missing-p_T), both cuts are removed to obtain the survivors in the table.

Released Cut Statistics			
released cut	*additional surviving events*		
	data	*Monte Carlo*	
		no add.	*add.*
p_T ratio	1	0.4	0.4
$q_T(\mu)$	7	3.0	3.8
Q^2 consistency	5	0.0	2.4
jet collimation	1	0.0	3.0
missing-p_T	26	8.0	15.3
m_τ	0	0.1	0.3
$y_{Bjorken}$	1	0.0	0.0

Table 7.12: Additional surviving events in data, CC and NC samples after the release of $\tau^- \to \mu^- \nu_\tau \bar{\nu}_\mu$ selection cuts.

For the cases in which the release of a cut results in a statistically relevant number of survivors, such as the missing-p_T and Q^2 consistency cuts, the data once again appear to be more consistent with the Monte Carlo sets with additions.

7.4 Estimation of Systematic Errors

Figure 7.22 shows the evolution of the signal and background efficiencies as a function of the applied cuts (enumerated in table 7.13). Again, the Monte Carlo curve with additions follows the data much more closely than the one without. This is particularly clear in figure 7.23.

Enumerated Cuts	
1	tight fiducial
2	loose μ ID
3	vertex association
4	track multiplicity, charge balance
5	tight μ ID
6	$\sigma(p_T)$
7	energy consistency, max. missing-p_T
8	loose p_T-ratio
9	$q_{T\mu}$
10	Q^2 consistency
11	jet collimation
12	missing-p_T
13	m_τ, $y_{Bjorken}$
14	tight p_T-ratio

Table 7.13: Definition of cut numbers as used in figures 7.22 and 7.23

An estimate of the systematic error on the τ efficiency is obtained in two ways:

1. from the difference in efficiency with and without additions (table 7.11)
2. from the maximum variation of the background efficiency (in the Monte Carlo with additions) with respect to the data efficiency (fig. 7.23).

In both cases, a systematic error of about 25% is obtained.

This result for the error can also be expressed in terms of the variation of individual cuts. The same variation in efficiency can be obtained, for example, by making any one of the following cut variations:

1. p_T-ratio in the range 0.4–0.6

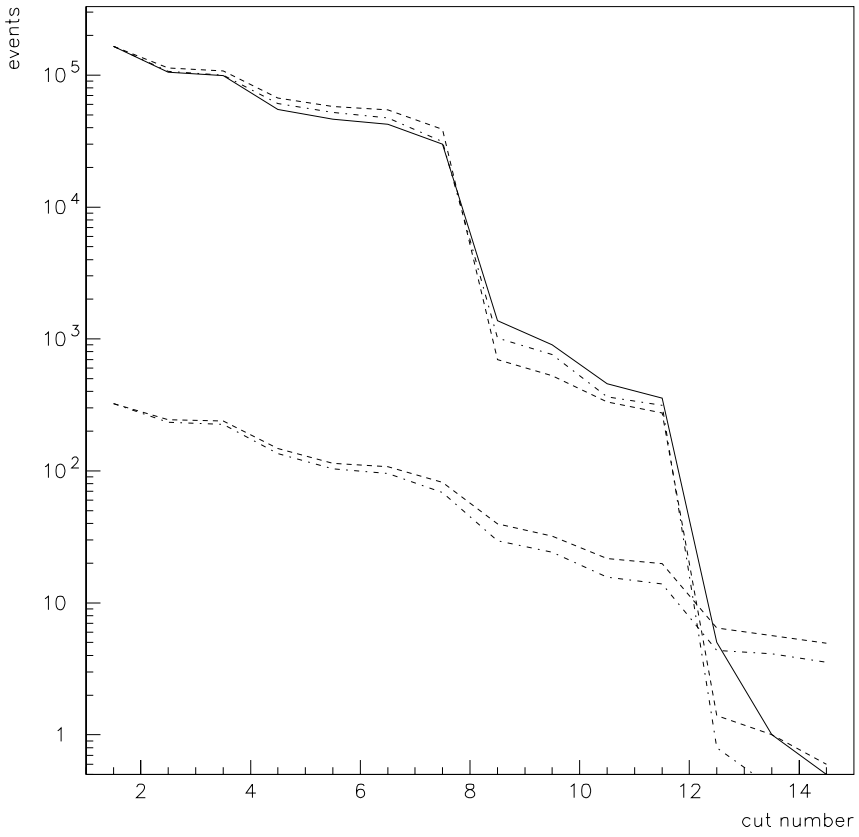

Figure 7.22: Surviving events as a function of cut number (table 7.13) for data (continuous line), MC without additions (upper dashed line), MC with additions (upper dash-dotted line), $\tau^- \to \mu^- \nu_\tau \bar{\nu}_\mu$ without additions (lower dashed line), and $\tau^- \to \mu^- \nu_\tau \bar{\nu}_\mu$ with additions (lower dash-dotted line).

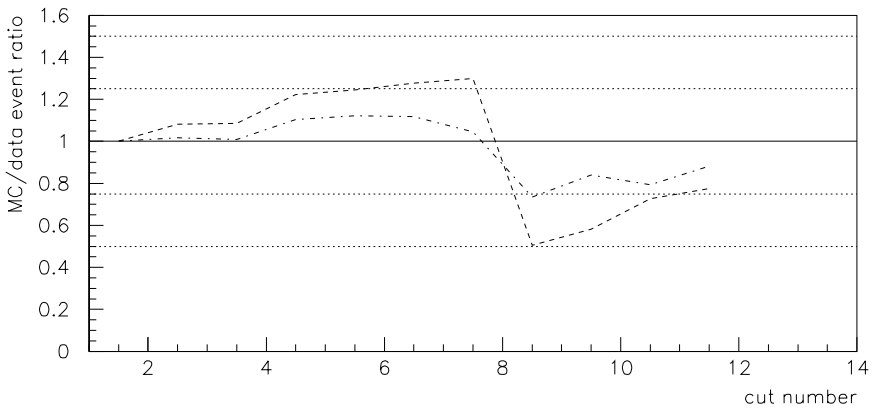

Figure 7.23: Ratio MC/data of surviving events as a function of cut number (table 7.13) for the Monte Carlo without additions (dashed line) and with additions (dash-dotted line).

2. missing-p_T in the range 1.4–1.9 GeV

3. $q_{T\mu}$ in the range 0.4–0.6 GeV

4. Q^2 consistency in the range 0.60–0.85.

The 25% change in efficiency if the τ mass correction is removed is a 1–sigma effect in these terms.

In analogous $\tau^- \to e^- \nu_\tau \bar{\nu}_e$ analyses in NOMAD, the efficiency reduction for the Monte Carlo with additions has been found to be consistent with that obtained using data sets in which final–state muons from measured ν_μ CC events are replaced with simulated τ–decays (often referred to as "data simulators"). Although similar studies remain to be done for this analysis, this is an important further cross-check. Therefore, to calculate a limit on $\nu_\mu \to \nu_\tau$ oscillations (chapter 8) the more conservative efficiency from the Monte Carlo with additions,

$$\epsilon = 0.8 \pm 0.2_{stat} \pm 0.2_{sys}\%$$

is used.

Chapter 8

Conclusions

8.1 Preliminary Limit Calculation

At this stage of the analysis, it may not be reasonable to assume that the $\nu_\mu \to \nu_\tau$ oscillation search via the $\tau^- \to \mu^- \nu_\tau \bar{\nu}_\mu$ channel will be unbiased and sensitive to the point where the limits on the neutrino mixing parameters obtainable from it may be of interest. To get some idea as to how sensitive the analysis is at the moment, this section is included to provide a sample calculation of those limits.

The first step is to calculate a confidence limit N_τ for the $\tau^- \to \mu^- \nu_\tau \bar{\nu}_\mu$ signal. Following reference 40, define n_0 to be the observed number of events. In this analysis, n_0 is the number of events left in the data sample after all selection cuts. Let μ_S be the unknown Poisson parameter for the signal and μ_B the known parameter for the sum of all the background. In this case, μ_S is the mean number of events in the final sample due to $\tau^- \to \mu^- \nu_\tau \bar{\nu}_\mu$ events, and μ_B is the total number of background events predicted by the Monte Carlo. The *minimum* probability that $\mu_S \leq N_\tau$ is then given by the equation:

$$P_{min}(\mu_s \leq N_\tau) = 1 - \frac{e^{-(\mu_B + N_\tau)} \sum_{n=0}^{n_0} \frac{(\mu_B + N_\tau)^n}{n!}}{e^{-\mu_B} \sum_{n=0}^{n_0} \frac{\mu_B^n}{n!}}. \tag{8.1}$$

Choosing $P_{min} = 0.9$ and using the results $\mu_B = 0.0$, $n_0 = 0$ from the $\tau^- \to \mu^- \nu_\tau \bar{\nu}_\mu$ event selection search (using the Monte Carlo set with additions) the equation yields

$N_\tau = 2.3$ for the 90% confidence limit on the $\tau^- \to \mu^- \nu_\tau \bar{\nu}_\mu$ event signal. To account for the 35% total error (section 7.4), this number is scaled to 2.6 [41].

The next step is to calculate the oscillation probability corresponding to the 90% confidence limit. The number of events expected in the data due to $\tau^- \to \mu^- \nu_\tau \bar{\nu}_\mu$ events is given by:

$$N_\tau = \int N_{CC},\ _\mu\epsilon \left(\frac{\sigma_\tau}{\sigma_\mu}\right) P(\nu_\mu \to \nu_\tau) dE \tag{8.2}$$

where N_{CC} is the total number of ν_μ CC events produced in the detector, , $_\mu$ is the branching ratio for the decay $\tau^- \to \mu^- \nu_\tau \bar{\nu}_\mu$ ϵ is the $\tau^- \to \mu^- \nu_\tau \bar{\nu}_\mu$ event selection efficiency, $\left(\frac{\sigma_\tau}{\sigma_\mu}\right)$ is the ratio of $\nu_\tau \to$ τ to $\nu_\mu \to$ μ production cross sections, and $P(\nu_\mu \to \nu_\tau)$ is the $\nu_\mu \to$ ν_τ oscillation probability.

Replacing the efficiency and cross section ratio with their energy–averaged values, and solving for the oscillation probability,

$$P(\nu_\mu \to \nu_\tau) = \frac{N_\tau}{N_{CC},\ _\mu\epsilon \left(\frac{\sigma_\tau}{\sigma_\mu}\right)}. \tag{8.3}$$

Using $N = 2.6$ as calculated above, this expression generates the 90% confidence limit on the $\nu_\mu \to \nu_\tau$ oscillation probability. From table 6.2, $N_{CC} = 194000$. From reference 40, , $_\mu = .178$. The energy–averaged $\tau^- \to \mu^- \nu_\tau \bar{\nu}_\mu$ event selection efficiency is the result from chapter 7: $\epsilon = 0.8$. The production cross section ratio is calculated to be 0.48. These values yield a probability limit of:

$$P(\nu_\mu \to \nu_\tau) < 2 \times 10^{-2}\ (90\%\ \text{CL}) \tag{8.4}$$

Conversely, if all muon neutrinos in the beam would oscillate into tau neutrinos, the number of expected τ candidates would be $N_\tau = N_{CC}\left(\frac{\sigma_\tau}{\sigma_\mu}\right),\ _\mu\epsilon = 133$.

Assuming the two–component model of neutrino oscillations (section 1.3), the result for the probability can be illustrated in terms of limits on the neutrino oscillation parameters. Due to the energy dependence of $P(\nu_\mu \to \nu_\tau)$ in this model, producing a full limit curve in the $(\sin^2\theta, \Delta m^2)$ parameter space would necessitate

inserting the expression for the oscillation probability:

$$P(\nu_\mu \to \nu_\tau) = \sin^2 2\theta \sin^2 \left(\frac{1.27 \Delta m^2 L}{E} \right) \tag{8.5}$$

into equation 8.2. A value for $\sin^2 \theta$ could then be generated for any Δm^2 by repeating the $\tau^- \to \mu^- \nu_\tau \bar{\nu}_\mu$ event selection on the $\tau^- \to \mu^- \nu_\tau \bar{\nu}_\mu$ Monte Carlo sample, weighting the resulting efficiency ϵ with the energy-dependent term in the above expression. Due to the poor sensitivity of this analysis at the present stage, however, the exact shape of the exclusion curve is not very illuminating.

A value for the mixing angle in the limit of large Δm^2 can be obtained from equation 8.3. In this limit, the oscillations take place over periodic lengths (equation 1.22) very short compared to the length scale of the experiment. The term $\sin^2 \left(\frac{1.27 \Delta m^2 L}{E} \right)$ in the expression for $P(\nu_\mu \to \nu_\tau)$ can then simply be replaced with the distance–averaged value of 1/2. From equation 8.3, the limit on the mixing angle becomes:

$$\sin^2 \theta = 2P(\nu_\mu \to \nu_\tau) < 4 \times 10^{-2} (90\% \text{ CL}) \tag{8.6}$$

For NOMAD, $L \simeq 1$ km and $E \simeq 10$ GeV, so that the limit $L_{osc} \ll L$ is attained by $\Delta m^2 > 1 \times 10^3$ eV^2. This limit is illustrated in figure 8.1.

8.2 Epilogue

A $\nu_\mu \to \nu_\tau$ oscillation search via the decay $\tau^- \to \mu^- \nu_\tau \bar{\nu}_\mu$ has been carried out on all of the 1995 data and Monte Carlo samples. The limit obtained for the (ν_μ, ν_τ) mixing angle at large Δm^2 is approximately $\sin^2 2\theta \leq 4 \times 10^{-2}$. This limit is roughly an order of magnitude less sensitive than the current best limit [42].

The oscillation search has been conducted using Monte Carlo sets to which nuclear and reconstruction effects have been added, and using sets without the additions. A 25% reduction in the $\tau^- \to \mu^- \nu_\tau \bar{\nu}_\mu$ event selection efficiency is observed on the set with the additions. However, the Monte Carlo set with additions behaves

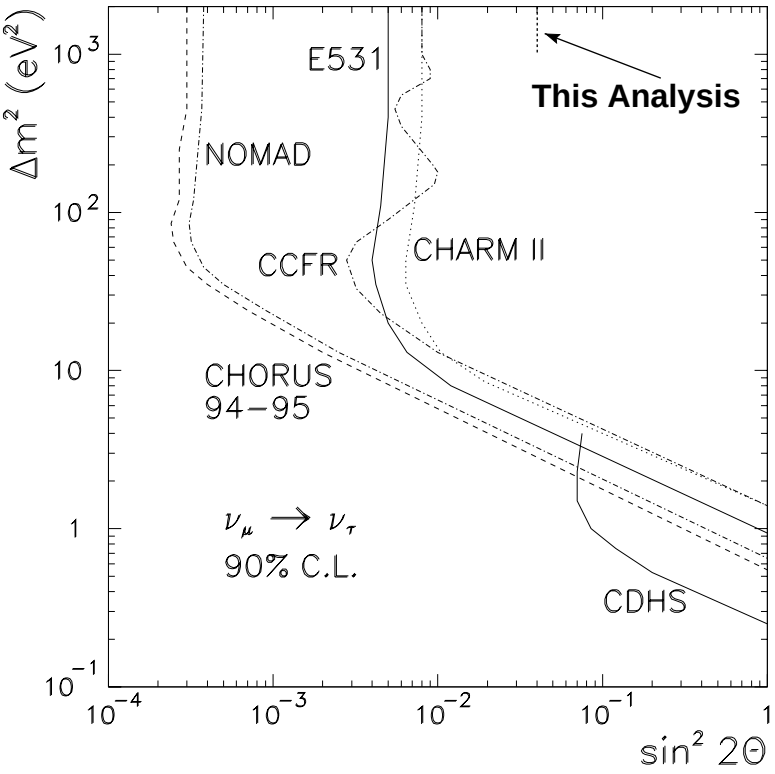

Figure 8.1: Large Δm^2 limit for $\sin^2\theta$ from this analysis, compared with limits from other experiments. The areas above and to the right of each curve are excluded at the 90% confidence level.

more similar to the data under most of the $\tau^- \to \mu^- \nu_\tau \bar{\nu}_\mu$ event selection cuts (including the cut in the $\phi_{\mu h} - \phi_{mh}$ plane), and demonstrates a more similar response upon the release of the most significant cuts. This observation is offered as an additional motivation for the serious consideration of the detailed simulation of nuclear effects in the Monte Carlo at the event–generation level.

Bibliography

[1] Cahn, Robert N. and Gerson Goldhaber, *The Experimental Foundations of Particle Physics* (New York, Cambridge University Press, 1991).

[2] Kim, C.W. and A. Pevsner, *Neutrinos in Physics and Astrophysics* (Chur, Harwood Academic Publishing, 1993).

[3] Reines, F. and C.L. Cowan, Jr. "Free Antineutrino Absorbtion Cross Section. I. Measurement of the Free Antineutrino Absorbtion Cross Section by Protons," *Physical Review* **113** 273 (1959).

[4] Frauenfelder. H., et. al., "Parity and the Polarization of Electrons from Co^{60}," *Physical Review* **106** 386 (1957).

[5] Goldhaber, M., L. Grodzins, and A.W. Sunyar, "Helicity of Neutrinos," *Physical Review* **109** 1015 (1958).

[6] Danby, G., et. al., "Observation of High–Energy Neutrino Reactions and the Existence of Two Kinds of Neutrinos," *Physical Review Letters* **9** 36 (1962).

[7] Davis, R., D. Harmer, and K. Hoffman, "Search for Neutrinos from the Sun," *Physical Review Letters* **20** 1205 (1968).

[8] DiLella, L., "Neutrino Oscillations" in *The 1995 CERN School of Particle Physics*

[9] 1 SNU (Solar Neutrino Unit) is defined as 1 capture per second per 10^{36} target atoms.

[10] Perkins, D., *Introduction to High Energy Physics*, 3rd ed. (Addison–Wesley Publishing Co., Inc., 1987) p. 242.

[11] Pontecorvo, B., *Zh. Expt. Theor. Fiz.* **33** 549 (1957) [JETP **6** 429 (1958)]; Pontecorvo, B., *Zh. Expt. Theor. Fiz.* **53** 1717 (1969) [JETP **26** 989 (1967)].

[12] Maki, Z., M. Nakagawa, S. Sakata, *Prog. Theor. Phys* **28** 870 (1962).

[13] Halzen, F. and A. Martin *Quarks and Leptons: An Introductory Course in Modern Particle Physics* (New York, John Wiley and Sons, Inc., 1984).

[14] Langacker, P. *Neutrino Mass* (Lectures presented at TASI-90, Boulder, CO, June 1990).

[15] The discussion in this section follows Boehm, F. and P. Vogel, *Physics of Massive Neutrinos*, 2nd ed. (Cambridge University Press, 1992), pp. 217–222.

[16] NOMAD Collaboration, "The NOMAD Experiment at the CERN SPS: A Status Report," *EPS HEP '95, 1995 International Europhysics Conference on High Energy Physics* Brussels, Belgium, 27 July–2 August 1995, p. 3.

[17] Altegoer, J., et. al., "The NOMAD Experiment at the CERN SPS," *Nuclear Instruments and Methods* (to be submitted).

[18] Acquistapace, G., et. al., CERN Internal Note, CERN-ECP 95-14, July 1995.

[19] Weisse, T., *Comparison of Muonic and Electronic Final States in the NOMAD Experiment at the CERN Wide-Band Neutrino Beam*, Ph.D. Thesis, Univ. of Dortmund, January 21, 1997 (Unpublished).

[20] Application Software Group, Computing and Networks Division, *GEANT: Detector Description and Simulation Tool*, CERN Programming Library Long Writeup W5013 (Geneva, Switzerland, 1993).

[21] Fasso A., et. al., "FLUKA92," in *Proc. of the Workshop on Simulating Accelerator Radiation Environments*, Santa Fe, NM, 1993.

[22] Gonzales-Garcia, M. C., and J.J. Gomez-Cadenas, *Prompt ν_τ Fluxes in Present and Future Tau Neutrino Experiments*, CERN Internal Note, CERN-PPE/96-114, August 14, 1996.

[23] Autiero, D., et. al., "The Electromagnetic Calorimeter of the NOMAD Experiment," *Nuclear Instruments and Methods* **A373** 358-373 (1996).

[24] Perrin, Y., et. al., *CASCADE: A Toolkit for the Construction of Distributed, Real–time Data Acquisition Systems*, CERN Internal Note, CERN ECP 93-13, October 1993.

[25] Astier, P., et. al., *Nomad Reconstruction Software Drift Chamber Package* Version 7 Release 1 (NOMAD Software Note, 23 September 1996). *This is the most complete reference, and contains descriptions of changes to version 5r9.*

[26] Bird, I. G., *Vertex Finding and Fitting Package* (NOMAD Internal Memo 96-019, 2 August 1996).

[27] Cattaneo, P. W., et. al., *The Reconstruction Algorithm and Bank Structure for the E.M. Calorimeter* (NOMAD Software Note, 12 November 1996).

[28] Bird, I. G., *RECON: NOMAD Reconstruction Program* (NOMAD Internal Memo 37, 24 September 1993).

[29] Application Software Group, Computing and Networks Division, *HBOOK–Statistical Analysis and Histogramming, Reference Manual*, Version 4.24, CERN Programming Library Long Writeup Y250 (Geneva, Switzerland, 1995).

[30] Meyer, J. P., and A. Rubbia, *NOMAD Event Generator Off-Line Manual (Draft)* (NOMAD Software Note, 20 December 1994).

[31] Ingleman, G., "LEPTO version 6.1—The Lund Monte Carlo for Deep Inelastic Lepton–Nucleon Scattering," *Physics at HERA* (proceedings), Hamburg, October 1991, v. 3., p. 1366.

[32] Sjostrand, Torbjorn, *Pythia 5.6 and Jetset 7.3, Physics and Manual*, CERN Programming Library Long Writeup W5035/W5044 (Geneva, Switzerland, May, 1992).

[33] Jadach, S., J. H. Kuhn, and Z. Was, *Computer Physics Communications* **64** 275 (1991), **66** 276 (1991), and **70** 69 (1992).

[34] Altegoer, J., et. al., *NOMAD GEANT Offline Manual* Version 5.11, (NOMAD Software Note, 3 July 1996). *The documentation for version 5.11 is identical to that of version 5.10, release 16, which has been used for the production of the MC samples.*

[35] Bodek, A., and J. L. Ritchie, *Physical Review D* **23** 1070 (1981).

[36] Guojo, H., and J. M. Irvine, *Journal of Physics G: Nuclear and Particle Physics* **15** 147 (1988).

[37] Burkot, W., et al., *Z. Phys.* **C 70** 47 (1993).

[38] Hanssgen, K., and J. Ranft, "The Monte Carlo Code NUCRIN," *Computer Physics Communications* **39** 53 (1986).

[39] NOMAD Collaboration, "Addendum to Proposal P261, Search for $\nu_\mu \to \nu_\tau$ Oscillation," CERN–SPSLC/91-53 SPSLC/P261 Add. 2, 25 October 1991.

[40] Particle Data Group, "Review of Particle Physics," *Physical Review D, Particles and Fields* **54** 166 (1996).

[41] R. Cousins and V. Highland, "Incorporating Systematic Uncertainties into an Upper Limit," *Nuclear Instruments and Methods in Physics Research* **A340** 331–335 (1992).

[42] N. Ushida et. al., *Physical Review Letters* **57** 2897 (1986).

Vita

The author was born in 1967 in Denver, Colorado, where he attended East High School. He graduated from Amherst College in Massachusetts in 1989 with a bachelor's degree in physics. His undergraduate thesis project was an experiment in high-temperature superconductivity, with Professor Joel Gordon. He spent the summer of 1988 working for Professor Gerald Gabrielse at Harvard University, helping to construct experiments for the trapping of single antiprotons. After college, he worked several months for Dr. George Lawrence at the University of Colorado's Laboratory for Atmospheric and Space Physics, helping to develop satellite instrumentation. He entered Johns Hopkins University in 1990, and worked for Professor Peter Fisher on the development of silicon and infrared detectors for the SSC. After receiving a master's degree in physics in 1993, he began full time work on his dissertation research on the NOMAD experiment at CERN, under the supervision of Professor Barry Blumenfeld.